ABSTRACT

Title of Document: EFFECTS OF MEMBRANE-BINDING PEPTIDES ON THE PHYSICAL PROPERTIES OF LIPID BILAYERS

Beatriz Eugenia Burrola Gabilondo
Doctor of Philosophy, 2010

Directed By: Professor Wolfgang Losert
Department of Physics

The physics of lipid bilayers has been studied for varying lipid and protein constituents. The effects of molecules that transiently associate with the bilayer is a new area of research. In this work, we focus on two proteins involved in vesicle trafficking inside cells, Arf1 and ArfGAP1. Research has suggested that these proteins may act as curvature generators or stabilizers. We generalize this hypothesis to suggest that the addition of these proteins to unilamellar vesicles would alter the physical characteristics of the lipid bilayers to favor deformations that lead to vesicle formation. Results from measurements of global properties such as membrane surface tension and bending rigidity are inconclusive due to the large variability intrinsic to vesicle samples. We find that the addition of peptide alters the thermally-driven fluctuations of the vesicles and biases the membrane shape during local deformations. Fluorescent probe experiments indicate that the association of myristoylated Arf1 peptide increases the packing of lipid molecules in the membrane. This work points to a potential novel role for these proteins as suppressors of negative curvature and calls for refinement of traditional techniques used to measure the physical properties of vesicles.

EFFECTS OF MEMBRANE-BINDING PEPTIDES ON THE PHYSICAL PROPERTIES OF LIPID BILAYERS

By

Beatriz Eugenia Burrola Gabilondo

Dissertation submitted to the Faculty of the Graduate School of the
University of Maryland, College Park, in partial fulfillment
of the requirements for the degree of
Doctor of Philosophy
2010

Advisory Committee:
Professor Wolfgang Losert, Chair
Professor Arpita Upadhyaya
Professor Arthur La Porta
Professor Srinivasa R. Raghavan
Professor Dionisios Margetis, Dean's Representative
Dr. Paul A. Randazzo, NIH Advisor

A mi familia,

a mi país

y

a Rolando.

Acknowledgements

First of all, I would like to thank my advisors Dr. Wolfgang Losert and Dr. Paul Randazzo for their support and guidance through this project. They were very patient with me and each other when things were not going as they had hoped. They also showed interest in my future and professional development, giving me advice when they felt I needed it.

I would like to thank my thesis committee: Dr. Dionisios Margetis, Dr. Arpita Upadhyaya, Dr. Arthur La Porta, and Dr. Srini Raghavan for agreeing to read my thesis and for all their valuable feedback.

I would like to thank my funding sources, especially the Consejo Nacional de Ciencia y Tecnología, the National Council of Science and Technology from Mexico, for their financial support through the formation of scientists fellowship.

The students in the *Losert lab* have been great in creating an inviting work atmosphere. I want to thank all of them for their support and advice and yes, the occasional chocolate and beer: Rodica Bauer, Meghan Driscoll, Mark Herrera, Colin McCann, Eleanor Ory, Dr. Andrew Pomerance, Cory Poole, and Steven Slotterback. The people from the *Randazzo lab* were also great. Dr. Fanny Campa, Dr. Pei-Wen Chen, Dr. Luan Ha, Dr. Hiroki Inoue, Dr. Xiaoyin Jian, and Dr. Hye-Young Yoon were always friendly and answered all my stupid biology and biochemistry questions.

I would like to thank Dr. Erin Rericha for all her help and valuable discussions about my projects and for being my mentor. I would like to also thank

Dr. Riubai Luo for her help and patience in teaching a physicist with no biochemistry background how to do basic biochemistry techniques. Her help was invaluable for the completion of this project.

I would like to thank the students that worked with me on this project: Jon Balajthy, Stevephen Hung, and Alex Steinkamp. Special thanks go to the summer undergrads of 2010, Peter Kordell, Anthony Coburger and Eric Kim, for putting up with my bad mood during the time I was writing this thesis.

During my time as a graduate student, I relied on the support of others to help me through different stages. I want to thank my study group for the qualifiers: Dr. Colleen Ellis, Dr. Renee Michelle Goertzen and Rebecca Knell-Olson; the IONS-NA Divas: Brooke Hester, Jem Galang, Katayoon Saadin, and Debjani Roy, for taking the risk of organizing a conference while being a graduate student with me; the Women in Physics group, especially Dr. Betsy Beise for being a great mentor and supporter; and my thesis writing buddies, Shaela Jones and Ellie Twedt.

I think two persons deserve a special mention: Nancy Cruz from NCI and Jane Hessing from UMD. Without them, both the Laboratory of Cellular and Molecular Biology at NCI and the Physics Department at UMD would probably fall apart. They go above and beyond their job description to make sure the bureaucratic wheels keep turning. Thank you for making sure I was able to focus on research.

I would like to thank my family, especially my parents and my siblings

(Jana, Fay y Mickey). They have always been supportive of my studies, even if they don't really know what a PhD is or why any reasonable person will stay in school an extra 6 years past college to get one. *Gracias por todo su apoyo y comprensión. Los quiero.*

Finally, I want to thank my wonderful husband. He has been there for me, making sure I don't carry the burden of the household by myself, even as we both work long hours and go to the lab on the weekends. *No soy la mujer que todo lo puede, pero contigo no tengo que serlo. Gracias.*

Table of Contents

List of Tables

List of Figures

Chapter 1: Motivation

Membranes, together with associated proteins, regulate specialized chemical processes inside the cell; membranes surround cells, allowing cells to regulate their internal chemistry and their interactions with the surrounding environment. Additionally, in eukaryotes, cells with a nucleus, internal cellular processes are divided into specialized compartments called organelles, which are separated from the rest of the cell by membranes. Membranes provide a contact surface for a wide range of proteins which carry out vital cell functions while membrane-bound. The transport of material between the different compartments inside the cell, which is crucial for the cell's survival, is regulated by proteins that attach to the periphery of membranes. We are interested in the effects that peripheral proteins implicated in material transport have on the physical properties of membranes.

Eukaryotes are divided into membrane-delimited organelles, each having specialized roles. Examples include the Endoplasmic Reticulum (ER), where amino acids are assembled into proteins; the Golgi, where proteins are modified with additional attachments such as carbohydrates and fatty acid tails; and the nucleus which holds the DNA and proteins needed to maintain DNA structure and function (Alberts *et al*, 2002).

Proper functioning of the cell requires the coordinated transport of material among organelles. Disruption or malfunction of material trafficking in human cells has been linked to congenital disorders, including deficient immune response

and neurological abnormalities (Gissen and Maher, 2007). The process of material transport (membrane trafficking) is accomplished through the action of vesicles; small sections of membrane pinch off from the host organelle and are transported to the target organelle, where they fuse to the target membrane, delivering their contents. Membrane-associated proteins are known to be involved in several steps of this transport process (Aniento *et al*, 2003).

It is assumed that during vesicle trafficking the membrane in the host organelle is deformed, going from nearly flat to highly curved (Alberts *et al*, 2002). Transport vesicles are of the order of 50-100 nanometers in size (Nossal, 2001) and the organelles from which they originate are 2-5 μm long (Phillips *et al*, 2008). Though the proteins involved in several vesicle trafficking complexes have been identified, it remains unclear how the membrane is deformed and from where the energy of deformation is contributed.

1.1 Composition of membranes

Membrane composition of organelles is unique for each compartment, though all biological membranes share common traits. In the fluid mosaic model, introduced by Singer and Nicolson (Singer and Nicolson, 1972), biological membranes are viewed as an oriented, two-dimensional, viscous solution of protein and lipid molecules in instantaneous thermodynamic equilibrium. According to this model, the membrane is a mosaic structure of proteins in low concentration dispersed in a two-dimensional sea of lipids. Over the past 38

years, however, our view of biological membranes has changed to that of a two-dimensional membrane with variable patchiness, variable thickness and high protein concentration (Engelman, 2005). The properties of the membrane will depend on the physical and chemical properties of the individual constituents, lipids and proteins, as well as on the interactions between them. Next, we introduce these basic physical and chemical properties.

1.1.1 Lipid molecules

Some but not all lipid molecules have an amphipathic nature. A hydrophilic end easily incorporates in the hydrogen-bond network with water while a hydrophobic tail that does not. In an aqueous environment, such as that inside the cell, lipid molecules will self-assemble into bilayer structures (figure 1.1). The lipids form two sheets, with the hydrophilic head-groups aligned towards the water molecules, and the hydrophobic tails aligned toward each other forming a hydrophobic core.

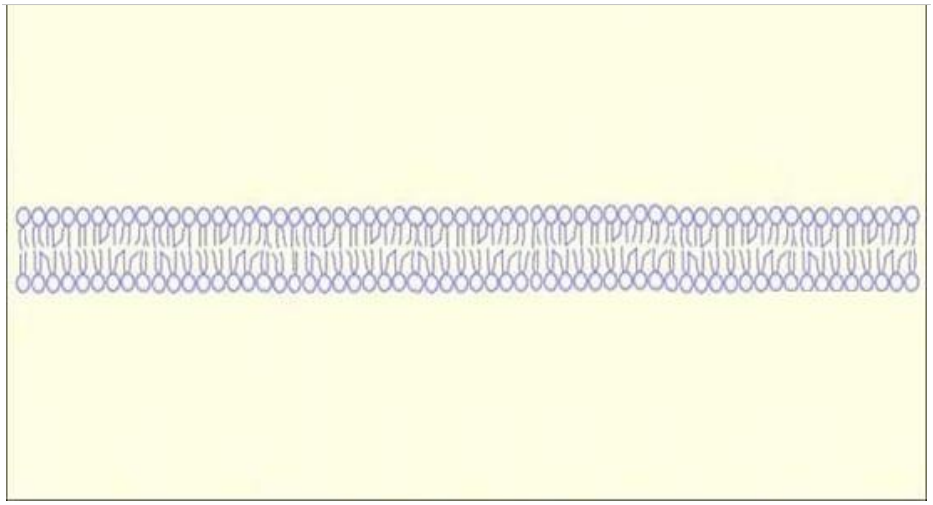

Figure 1.1: Cartoon of a lipid bilayer in an aqueous environment with the head groups aligned toward the water, while the tail groups aligned towards the middle hydrophobic core. Image modified from: www.erin.utoronto.ca/~w3bio315/lecture2.htm

Lipid bilayers display interesting physical properties. They are easily deformable but not easily stretchable and can bend into a wide range of patterns from spheres to planar sheets. Bilayers do not behave as simple elastic sheets, since the lipid molecules are free to diffuse along the surface. Hence, the viscous component of the bilayers is important.

Lipid bilayers have bending rigidity and surface tension, that is, there is an energetic cost for bending and stretching the bilayer. A common way to measure bending rigidity is by micropipette aspiration. In this technique, a giant unilamellar vesicle is partially sucked into a micropipette, setting a uniform tension on the vesicle. The pressure applied is known to the experimenter, and simple geometrical considerations and measurements give a measure of the tension on

the surface. Measuring this tension as a function of surface area yields the bending rigidity of the membrane, since the bending rigidity is the proportionality constant between the two.

Lipid bilayers exhibit phase separation. In mixtures of different lipid composition, the lipid molecules segregate into domains based on the order or packing of the molecules. For phase separation to occur, at least three lipid species must be present: one high melting temperature lipid with saturated fatty acid tail groups, one low melting temperature lipid usually, though not necessarily, with unsaturated fatty acid tail groups, and cholesterol (Veatch and Keller, 2003). Domains in these so-called ternary mixtures can be present in one of several phases: liquid ordered (Lo) phase where lipid molecules are found in short range order, liquid disordered (Ld) phase where lipid molecules present no order, and gel-like phase with long range order between the molecules.

The phase that lipids display depends on the temperature, with lipids usually exhibiting liquid disordered phase for high temperatures and liquid ordered or gel-like phase for lower temperatures.The melting temperature is defined by the phase transition between these states. In samples composed of ternary mixtures, lipids will be mixed homogeneously for temperatures above the highest melting temperature of the lipid components, and exhibit phase separation for temperatures below that (Veatch and Keller, 2003).

In giant vesicles with Ld and Lo phases, a line tension in the area joining the domains is observed, with Ld domains bending towards Lo domains. Hence,

Ld domains have a smaller bending rigidity than Lo domains. Increasing the temperature of these samples causes similar domains to fuse forming larger domains and can even induce vesicle fission (Baumgart *et al*, 2003).

The two-loosely-connected-layers structure of lipid membranes gives rise to interesting properties. The physics of two-dimensional sheets has been studied in the past assuming the membrane is infinitesimally thin. This assumption is not true for lipid bilayers. In addition, the monolayers are not completely independent. Each monolayer can have a different area, giving rise to non-local bending elasticity, reflecting the energetic cost of keeping the monolayers together through deformations that deviate from the preferred lower energy state for each one in isolation (Miao *et al*, 1994). The finite thickness of each monolayer and the weak interactions between them give rise to an inter-monolayer friction, which plays an important role in the behavior of lipid membranes (Evans and Yeung, 1994).

1.1.2 Membrane proteins

The physical properties, shapes, and dynamics of lipid bilayers are further complicated by the presence of proteins bound to the membrane. As much as one third of the genes in a typical genome encode membrane proteins (Phillips et al, 2009). Indeed, the ratio by weight of proteins to lipids in a biological membrane ranges from about 1.5 to 4 (Singer and Nicolson, 1972), suggesting that cell membranes are primarily composed of proteins.

The conformation that a protein adopts is sensitive to the surrounding

environment. For instance, when in an aqueous solution, the non-polar residues are sequestered in the core of the protein, while the ionic residues are in contact with water. However, when a protein is in a hydrophobic environment, the conformation may change. Binding of additional elements can also alter the protein shape. This flexibility of conformation allows proteins to change shape when interacting with amphipathic lipid bilayers.

Membrane proteins are divided into two populations based on their biochemistry: peripherally associated proteins and integral proteins. Peripheral proteins are easily dissociated from the membrane, and are relatively soluble when found in an aqueous neutral buffer. On the other hand, integral proteins require more drastic means to dissociate from membranes, such as treatment with detergents, and remain associated with lipids, even after isolation.

Integral proteins, which are the majority of membrane-associated proteins, are amphipathic globular structures that partially embed and partially protrude from membranes. Integral proteins can be attached to carbohydrates to form glycoproteins or interact strongly with specific lipids, forming lipoproteins. The structure adopted by a particular protein within the membrane will depend on the amino acid sequence, the covalent bonds within the protein itself, as well as the protein's interactions with the surrounding environment. Integral transmembrane proteins can cross from one side of the bilayer to the other once or several times. Integral proteins can also associate with peripheral proteins, or with other integral proteins, forming complexes.

It has long been assumed that only integral proteins contribute to the structural integrity and the physical properties of the membrane (Singer and Nicolson, 1972). However, other work has shown that peripheral proteins affect the properties of the membrane also (Lee *et al*, 2000), and mutations or malfunction of peripheral proteins can significantly alter the proper functioning of the cell (Gissen and Maher, 2007). An example of the importance of the activity of peripheral proteins in cellular function is vesicle trafficking.

There are several vesicle trafficking processes inside the cell that rely on coated vesicles; figure 1.2 shows three of them. The COPI vesicle trafficking complex is responsible for transport of material in the retrograde direction, from the Golgi to the ER. The COPII complex transports material in the anterograde direction, from the ER to the Golgi. Finally, clathrin-coated vesicles transport material from the plasma membrane in endocytosis and from endosomes to the trans Golgi. During the formation of a transport vesicle, the membrane is assumed to be deformed. Although many of the proteins that are associated with transport vesicles have been identified, the precise cause of this membrane deformation remains unknown.

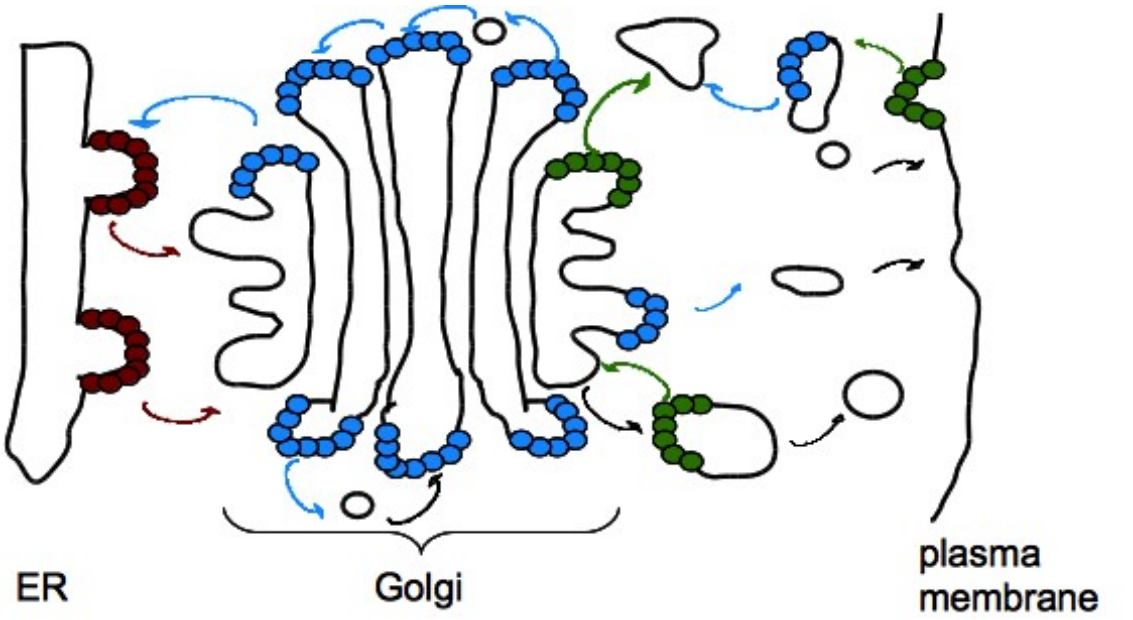

Figure 1.2 Different coat proteins select cargo and coat vesicles in different transport pathways. Red represents COPII, blue represents COPI, and green represents clatrhin coats. Figure adapted from Molecular Biology of the Cell [4, Fig 13-5 p. 176]

1.2 COPI vesicle trafficking

A well studied vesicle transport complex is the coat protein 1 (COPI) complex, whose function is to transport material in the retrograde direction within the Golgi and from the Golgi to the ER (Aniento *et al*, 2003). Figure 1.3 shows a schematic of the steps thought to be involved in COPI vesicle formation (Nie *et al*, 2003). An important component of COPI vesicle formation is the protein Arf1.

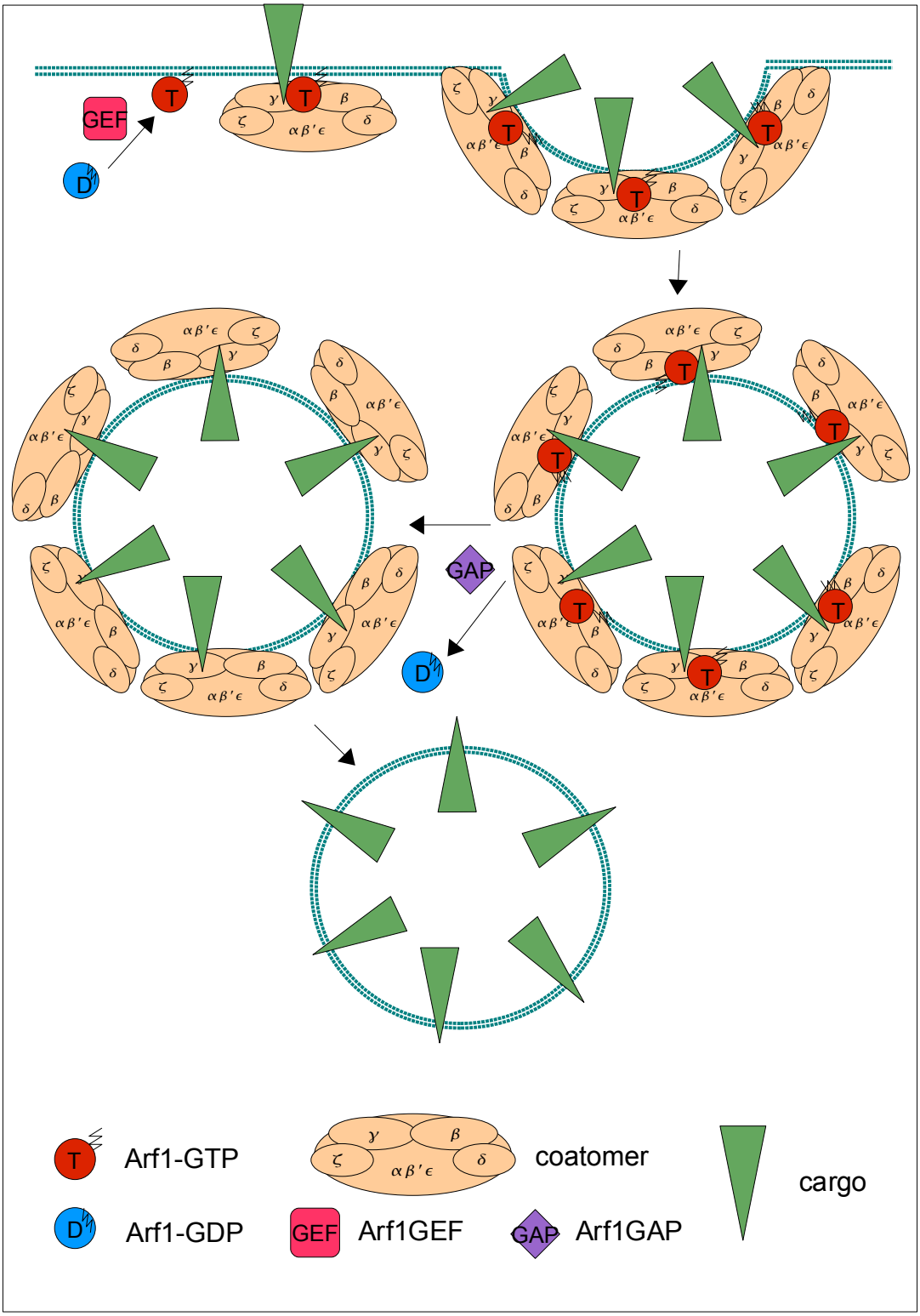

Figure 1.3: Model of COPI vesicle formation in the Golgi. During the process the membrane is deformed from low curvature to high curvature.

Like other proteins of the Ras superfamily, Arf1 acts as a (guanosine tri-phosphate)GTP-dependent switch: it associates to membranes more strongly when bound to GTP, and hydrolysis of GTP on Arf1 results in dissociation of Arf1 from the membrane (Kahn *et al*, 1992). Arf1 associates to membranes through its N-terminus and myristic acid attached to the N-terminus, which is exposed by a conformational change occurring upon binding to GTP. In the GDP-bound form of Arf1 the myristoylated N-terminus is folded into the core of the protein (Amor et al, 1994). The transition from GDP- to GTP-bound form of Arf1 is regulated by nucleotide exchange factors (GEF), while hydrolysis of GTP is caused by the action of GTPase-activating proteins (GAP), such as ArfGAP1.

Before the formation of a vesicle, GTP-bound Arf1 associates to the membrane. Once on the membrane, GTP-bound Arf1 associates with coatomer proteins, which in turn associate with cargo proteins (figure 1.4).

A proposed role of Arf1 in the COPI complex is to induce curvature, since Arf1 has been reported to bend membranes (Beck *et al*, 2008; Lundmark *et al*, 2008; Krauss *et al*, 2008). When GTP-bound Arf1 is incubated with lipid bilayers, tubular structures appear, both from planar sheets (Beck *et al*, 2008) and from liposomes (Lundmark *et al*, 2008; Krauss *et al*, 2008). Such structures are not observed when the lipid bilayers are incubated with GDP-bound Arf1. The authors of these studies concluded that GTP-bound Arf1 induces the formation of these structures. Arf1 is also thought to regulate the coat of COPI vesicles (Donaldson *et al*, 1992) and adaptor proteins (Boehm *et al*, 2001). Another

proposed mechanism for Arf1 is that it associates with coatomer and ArfGAP1 in tripartite subunits, which can then polymerize and deform the membrane (Bigay *et al*, 2003).

Several of the Arf1-coatomer-cargo complexes polymerize at the site where the membrane is subsequently deformed. The membrane bulges out forming a bud at the location of the polymerized COPI complex, and the coated vesicle pinches off. GTP bound to Arf1 is hydrolyzed by the action of a GAP, such as ArfGAP1, causing Arf1 to undergo a conformational change resulting in the myristoylated tail to be folded into the core of the protein and Arf1 dissociating from the membrane. It is unclear if this process happens before the vesicle pinches off from the Golgi or after the vesicle is fully formed (Nie *et al*, 2006).

In figure 1.3, ArfGAP1 is not shown associated to the membrane nor to other proteins in the complex, though there is evidence that it associates directly to the membrane (Bigay *et al*, 2005) and that its function is regulated by coatomer and cargo proteins as well (Luo and Randazzo, 2008). ArfGAP1 has two ALPS (ArfGAP1 lipid packing sensor) motifs that show no defined structure in solution, but fold into an alpha-helix when associated to lipid membranes (Bigay *et al*, 2005). ArfGAP1 has also been reported to function as a curvature sensor (Drin *et al*, 2007; Mesmin *et al*, 2007). Consistent with its role to mediate the release of Arf1 from a vesicle, the ALPS domains of ArfGAP1 have been shown to bind more efficiently to vesicles of smaller radii, suggesting a higher affinity of ArfGAP1 for high curvature surfaces (Drin *et al*, 2007; Mesmin *et al*, 2007).

Dissociation of Arf1 from the membrane precedes dissociation of the coatomer. Finally, after the coat proteins dissociate from the membrane, the naked vesicle is transported to the ER or other parts of the Golgi (Nie and Randazzo, 2006).

1.3 A possible conserved mechanism for bending the membrane

There are no images of COPI-coated vesicles. However, recent studies on the structure of domains of coatomer protein indicate possible similarities between the association of tripartite subunits which can polymerize to form a coat and the association of clatrhin tiskelia (Lee and Goldberg, 2010), suggesting a possible similarity in function for coated vesicles. Figure 1.4 shows the proposed shape of basket subunits for each of these vesicle complexes based on currently available data.

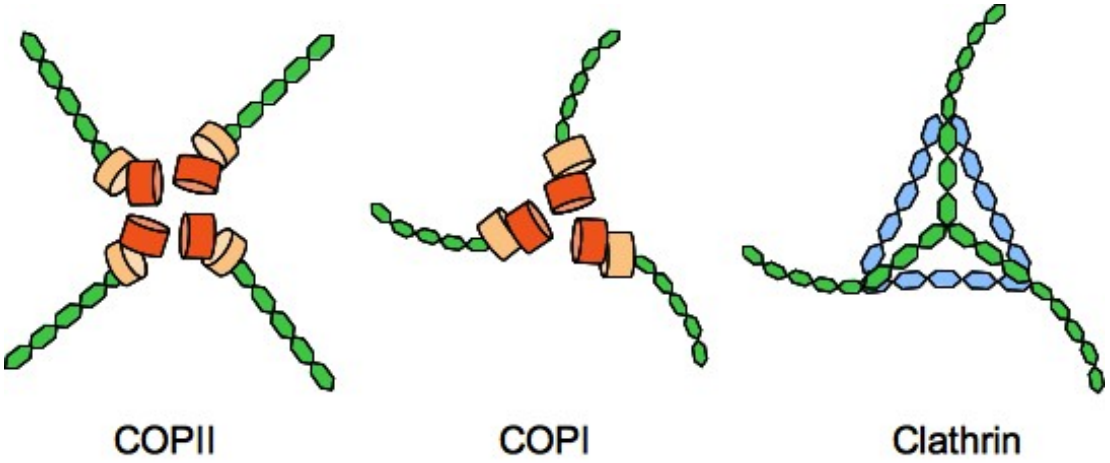

Figure 1.4: Suggested relationship among COPI, COPII and clatrhin basket subunits. COPI is thought to present characteristics of both COPII and Clatrhin coats. Figure adapted from Lee and Goldberg, 2010.

It has been suggested that polymerization of clathrin basket subunits, called triskelia, could drive membrane bending and initiate vesicle formation (Jin and Nossal, 1993). However, calculations and experiments done on clathrin-coated vesicles show that the polymerization of the coat alone is not enough to form a vesicle. The free energy change that occurs when a given number of subunits combine to form a coat or basket (Nossal, 2001) can be expressed as a function of three parameters representing the bending rigidity of the subunits, the preferred curvature of the subunit assembly (preferred number of subunits in basket if subunits do not deform), and the association of different triskelia. Assuming the size distribution of baskets in equilibrium is represented by a Boltzmann distribution, these three parameters can be estimated based on the distribution width at half maximum and the basket size with the maximum counts.

Baskets formed from clathrin alone have a wider size distribution than

those formed in the presence of assembly proteins (Zaremba and Keen, 1983). This suggests, based on the model by Nossal, that inclusion of assembly proteins increases the rigidity, as well as the effective curvature, of subunits forming the basket (Nossal, 2001). This is in line with the idea that assembly proteins and other adaptors can act as braces that stabilize the assembled subunits.

These results also suggest that remodeling and growth of structures made from individual clathrin subunits can be thermally driven, as the free energy change associated with addition of subunits to a basket already formed is of the order of $k_B T$ (where k_B is Bolztmann's constant and T is the absolute temperature), while the overall energy cost of forming a complete basket is much higher than $k_B T$, leading to baskets that are stable (Nossal, 2001).

The bending moduli found for clathrin baskets are comparable to reported values of membrane bending moduli (Nossal, 2001). Hence, clathrin baskets cannot by themselves induce membrane bending. Another protein might bend the membrane into a patch with high enough curvature to aid in the assembly of clathrin-coated vesicles. The protein Epsin1 seems to be a good candidate (Nossal and Zimmemberg, 2002).

As in the case of Arf1, liposomes incubated with Epsin1 show tubular structures when observed under electron microscope (Ford, 2002). Again, as Arf1, Epsin1 is not a contractile protein, nor an ATPase, which means it can only passively alter the membrane and create tubes. It could create such structures by bending the membrane through increasing the bilayer spontaneous curvature

by increasing the area of the monolayer into which it inserts, or by increasing the spontaneous curvature of the monolayer, without changing the area (for further details in the theory see chapters 2 and 3).

Though studies on the energetics of COPI baskets have not been conducted, the similarities in shape and dimension between COPI coat and clathrin, as well as the similar effect of Arf1 and Epsin1 on membranes *in vitro*, indicate a possible conserved mechanism for vesicle formation. Hence, the model emerging from the study of clathrin-coated vesicles and the role of Epsin1 as a curvature generator could be relevant in the understanding of COPI vesicles, and the role of Arf1 and/or ArfGAP1.

In this work, we set out to test the hypothesis that Arf1 or ArfGAP1 induce and stabilize local membrane curvature. This curvature-stabilizing action would then lead to the polymerization of the other COPI proteins and the formation of a vesicle.

1.4 This work – model system and hypothesis

Arf1 has an amphipathic helix at the amine end of the protein, its N-terminus. This peptide shows little alpha-helix structure in solution, but a strong alpha-helix structure when associated with phospholipid membranes (Kahn *et al*, 1992). Arf1 has a myristoyl moiety, a 14-carbon saturated chain, attached to a glycine at the N-terminus. This fatty acid chain is necessary for the efficient association of Arf1 to membranes – non-myristoylated Arf1 does not bind strongly

to liposomes (Kahn *et al*, 1992). As noted above, the myristoylated N-terminus of Arf1 is exposed upon association of GTP with the protein. Hence, it is believed that this section of Arf1, the myristoylated N-terminus, is important for the protein's function.

ArfGAP1 has two ALPS domains which preferentially bind to liposomes of smaller radii, or higher curvature. Proteins other than ArfGAP1 have been reported to have ALPS-like motifs. These proteins' ALPS domains share homology to the ALPS domains of ArfGAP1 and show a preference for vesicles of smaller size (Drin *et al*, 2007).

The peptides chosen for this study are: the myristoylated N-terminus of Arf1 and the ALPS domain of the yeast protein Kes1p as a proxy for the ALPS domain of ArfGAP1. The ALPS domain of Kes1p was modified by addition of two lysines at the N-terminus and one lysine at the C-terminus, since the ALPS domain of ArfGAP1 and Kes1p precipitate from aqueous solutions. Both the myristoylated and non-myristoylated forms of the Arf1 N-terminus were used. Miristic acid, the 14-carbon fatty acid chain found attached to the N-terminus of Arf1 was chosen as a control. Figures 1.5 and 1.6 shows the amino acid sequence of the peptides used.

```
  2  GNIFANLFK GLFGKKEMRI LMVGLDAAGK TTILYKLKLG EIVTTIPTIG
 51 FNVETNEYKN ISFTVWDVGG QDKIRPLWRH YFQNTQGLIF VVDSNRERVN
101 EAREELMRML AEDELRDAVL LVFANKQDLP NAMNAAEITD KLGLSLRHRN
151 WYIAQTCATS GDGLYEGLDW LSNQLRNQK
```

Figure 1.5: Amino acid sequence of Arf1. The N-terminus is shown in red and underlined.

```
  1 MSQYASSSSW TSFLKSIASF NGDLSSLSAP PFILSPISLT EFSQYWAEHP
 51 ELFLEPSFIN DDNYKEHCLI DPEVESPELA RMLAVTKWFI STLKSQYCSR
101 NESLGSEKKP LNPFLGELFV GKWENKEHPE FGETVLLSEQ VSHHPPVTAF
151 SIFNDKNKVK LQGYNQIKAS FTKSLMLTVK QFGHTMLDIK DESYLVTPPP
201 LHIEGILVAS PFVELEGKSY IQSSTGLLCV IEFSGRGYFS GKKNSFKARI
251 YKDSKDSKDK EKALYTISGQ WSGSSKIIKA NKKEESRLFY DAARIPAEHL
301 NVKPLEEQHP LESRKAWYDV AGAIKLGDFN LIAKTKTELE ETQRELRKEE
351 EAKGISWQRR WFKDFDYSVT PEEGALVPEK DDTFLKLASA LNLSTKNAPS
401 GTLVGDKEDR KEDLSSIHWR FQRELWDEEK EIVL
```

Figure 1.6: Amino acid sequence of the yeast protein Kes1p. The ALPS domain is highlighted in green. We used a peptide based on this sequence, with two added lysines on the N-terminus and one on the C-terminus.

The myristoylated N-terminus of Arf1 could induce curvature the following ways:

1) Insertion of the myristoylated N-terminus of Arf1 on one side of bilayer could decrease bending rigidity, making the membrane easier to bend.
2) Insertion of the myristoylated N-terminus of Arf1 on one side of bilayer could decrease the force required to form and maintain a tether.
3) Insertion of the myristoylated N-terminus of Arf1 on one side of bilayer could change non-local properties of the bilayer, like increasing inter-monolayer friction or the area difference between the monolayers. Increased area of the outer monolayer could then induce buckling of the bilayer.
4) Insertion of the myristoylated N-terminus of Arf1 on one side of bilayer could decrease lipid packing, making lipid bilayers more fluid-like. This would be consistent with the membrane being easier to bend.

5) Insertion of the myristoylated N-terminus of Arf1 on one side of bilayer could increase lipid lateral mobility, making lipids more fluid-like. This would be consistent with the membrane being easier to bend.

1.5 Thesis Outline

We set out to test the hypothesis that Arf1 induces membrane curvature by making the membrane easier to bend through the insertion of its myristoylated N-terminus. This work presents results and discussion of experiments conducted to test this hypothesis.

Stabilizing curvature could lead the membrane to bend more easily or reduce bending rigidity. In order to test if the Arf1 peptide has an effect on the large-scale, global properties of the bilayer, I conducted experiments to measure the bending rigidity and surface tension of the bilayer. **Chapter 2** presents results of flicker spectroscopy experiments, in which the Fourier modes of membrane fluctuations, observed in Giant Unilamellar Vesicles (GUV) made of 1,2-dioleoyl-*sn*-glycero-3-phosphocholine (DOPC) using bright field microscopy, are related to the surface tension and bending rigidity of the vesicle. Adding myristoylated N-terminus of Arf1 appears to change the functional shape of the fluctuation spectra, though large variations in the model system used lead to inconclusive results.

Stabilizing the local curvature of the membrane would make it easier for an external agent to deform the membrane on length-scales similar to the

preferred curvature. We set out to test the hypothesis that the myristoylated Arf1 peptide will make it easier to deform a bilayer into a thin tube. **Chapter 3** presents results from experiments for pulling and retraction of thin tubes, called tethers, extruded from a GUV by holding a silica bead adhered to the vesicle in an optical trap while moving the GUV away, and later releasing the bead to let it retract. The force on the bead as the bilayer is deformed can be measured. The retraction speed of the bead in the constant speed regime is directly proportional to the critical force required to maintain a stable cylindrical tether, which is in turn directly proportional to the bending rigidity of the membrane. Any large changes in membrane shape can also be observed. The large variations of the measurements of pulling force and retraction speed between and within batches of GUV makes the results of adding myrisoylated N-terminus of Arf1 to the outside of the GUV inconclusive. However, the addition of peptide makes the appearance of a bulge in the GUV during retraction more likely.

Global membrane properties were not considerably changed by addition of myristoylated N-terminus of Arf1, though there are some indications that the peptide does affect the membrane. In order to test the hypothesis that Arf1 stabilizes membrane curvature by affecting the lipid molecules locally, we conducted fluorescence spectroscopy studies as a way to asses any changes in lipid order and membrane fluidity. **Chapter 4** presents results and discussion of fluorescence spectroscopy measurements on Large Unilamellar Vesicles (LUV) made of DOPC in the presence of varying concentrations of the peptides of

interest. Three fluorescent molecules that have different fluorescence spectra depending on the physical properties of the environment in which they are present were used to assess lipid packing in the bilayer (Diphenylhexatriene and Prodan) and lateral mobility along the plane of the bilayer (Bis-pyrene). The myristoylated N-terminus of Arf1 increases the packing of the lipid molecules, while non-myristoylated N-terminus of Arf1 and myristic acid do not. Lateral mobility of the lipid molecules was not affected.

Finally, Chapter 5 presents analysis and discussion of the combined results for all three experiments, as well as a discussion of open directions of research.

Chapter 2: Flicker spectroscopy

To test the peptide effect on the large-scale properties of lipid membranes, we conducted flicker spectroscopy experiments, where the fluctuations of Giant Unilamellar Vesicles (GUV) are related to large-scale physical properties of the membrane, such as surface tension and bending rigidity. This technique estimates the surface tension and bending rigidity of an almost-spherical membrane by measuring the variance of fluctuations from images taken of the widest part of the GUV. This chapter presents results of flicker spectroscopy measurements done on GUV with varying concentrations of peptide. We find that addition of peptide to GUV increases the variability of measured fluctuations. The variance spectra for GUV in the presence of peptide, for some cases, no longer fit to the model derived for GUV composed of lipid alone. This suggests that the assumptions on which the model is based, such as uniformity throughout the surface, no longer apply when peptide is added.

2.1 Introduction

Lipid bilayers can be characterized by the physical parameters expressing the energetic cost to bend the membrane, or bending rigidity, and the energetic cost to change the area of a patch of membrane, or surface tension. Bilayers formed of different lipid species will have, in general, different surface tensions and rigidities. Addition of dissimilar components, like cholesterol or peptides, into the bilayer could affect these global properties. In flicker spectroscopy, the

fluctuations of a lipid bilayer are used to estimate the surface tension and bending rigidity of the membrane. This section introduces the theoretical considerations relevant to flicker spectroscopy and a summary of bending rigidity values for lipid bilayers of different composition that have been reported in the literature.

2.1.1 Flicker spectroscopy

Flicker spectroscopy or contour analysis obtains a measure of the membrane surface tension and bending rigidity by measuring the fluctuations of the membrane. The deviation of the membrane from either a planar sheet (Helfrich, 1984) or a sphere (Milner and Safran, 1987) is decomposed into Fourier modes, and these deviations are then related to the physical parameters of the membrane's elastic energy. This section presents the theory of flicker spectroscopy, where Fourier modes of fluctuating vesicles imaged under bright field microscopy are used to estimate the bending rigidity and surface tension of the lipid membrane. This analysis is based on a model first proposed by Döberiener *et al* (2003), and should be extendable, in principle, to non-equilibrium membranes, such as lipid bilayers with active proteins (Pécréaux *et al*, 2004).

Lipid bilayers in water undergo thermal fluctuations. These small undulations, or deviations from the mean position of the membrane, $u(\vec{r})$, will change the free energy of the membrane. The energy change due to these undulations has two contributions, one from the difference between the area of

the stretched patch and its projected area to the (x,y)-plane, and one from the curvature elastic energy:

$$\Delta F = \int dA[\sigma|\nabla u(x,y)^2| + \kappa(\nabla^2 u(x,y))^2] \quad 2.1$$

The undulations can be decomposed into modes. In terms of complex waves, these modes can be written as follows, for a square patch of area *A* with periodic boundary conditions:

$$u(\vec{r}) = \frac{1}{\sqrt{(A)}} \sum u_q \exp(i\vec{q}\cdot\vec{r}) \quad 2.2$$

Here, $\vec{q}$ is the wave vector, $\vec{r}$ is the position vector along the patch of membrane, and u_q is the undulation amplitude for a given wave vector.

The expression for surface energy in Fourier coordinates is then (Safran, 1994):

$$\Delta F_s = \sigma \sum q^2 |u(\vec{q})|^2 \quad 2.3$$

Treating ΔF_s as a Hamiltonian of the fluctuating variable $u(\vec{q})$, the probability of finding $u(\vec{q})$ with a particular value is proportional to $\exp[-\Delta F_s / k_B T]$. The mean-square value of $u(\vec{q})$ due to surface energy contribution can be found through the Equipartition Theorem:

$$\langle |u(\vec{q})^2| \rangle_s = \frac{k_B T}{\sigma q^2} \quad 2.4$$

One can treat the contribution to the change in energy due to the bending on the membrane caused by the thermal undulations in a similar fashion (Safran, 1994). The expression for bending energy in Fourier coordinates is

$\Delta F_b = \kappa \sum q^4 |u(\vec{q})|^2$, and the mean-square fluctuation of the undulations is

$$\langle |u(\vec{q})^2| \rangle_b = \frac{k_B T}{\kappa q^4} \qquad 2.5$$

The full mean-square fluctuation spectrum for planar (infinite) membranes, considering tension and rigidity simultaneously, is (Helfrich, 1984):

$$\langle |u(q)|^2 \rangle = \frac{k_B T}{\sigma q^2 + \kappa q^4} \qquad 2.6$$

Images of giant vesicles under bright field microscopy allow one to only see the equator of the vesicle. Hence, a two-dimensional projection of a three-dimensional sphere must be used as a model for the fluctuating membrane. Figure 2.1 represents a contour found from an experiment. The vesicle is a 3D sphere, and the points along the surface will be (in cylindrical coordinates) a function of radius, angle, and height. The plane of the equator of the vesicle is defined in the analysis that follows as y=0. Pécréaux *et al* found that the predictions for a planar membrane deviate from those of a spherical membrane only for the first few modes. As a result, we adopt the approach used by other groups and ignore the contribution of the first five modes in the fluctuation spectrum analysis, as explained in section 2.2.4.

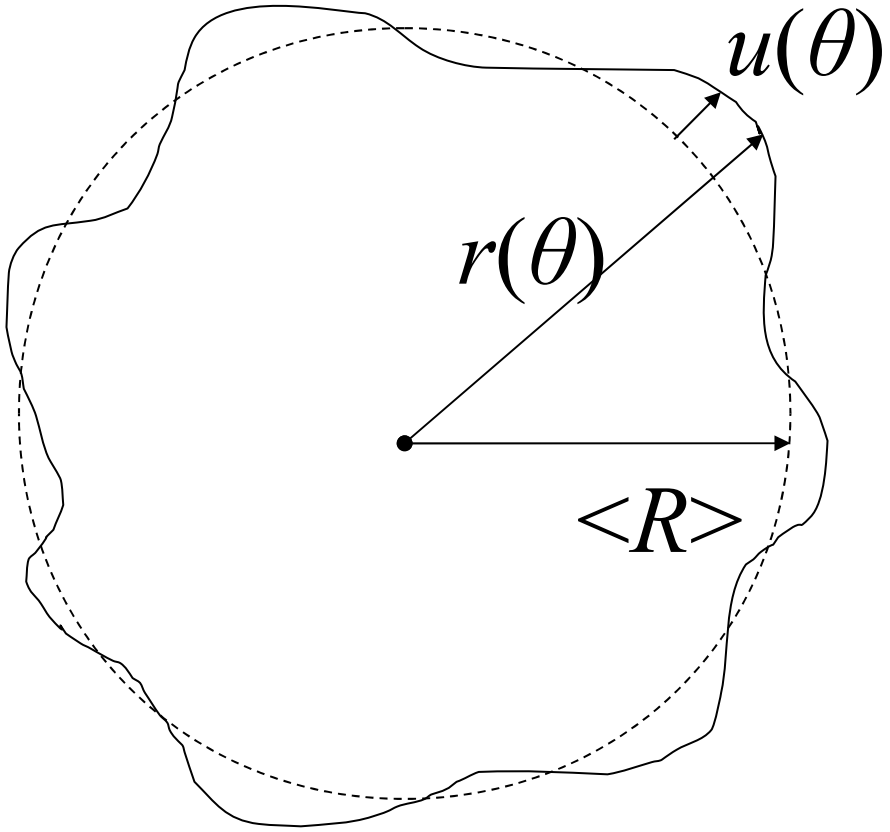

Figure 2.1: Fluctuating vesicle

The predicted observable fluctuations are then (Pécréaux *et al*):

$$\langle |u(q_x, y=0)|^2 \rangle = \frac{k_B T}{2\sigma} \left[\frac{1}{q_x} - \frac{1}{\sqrt{(\sigma/\kappa + (q_x)^2)}} \right] \qquad 2.7$$

The expression for the fluctuation spectrum must be modified to take into account the sampling bias introduced by the digital camera in an experiment. The corrected expression used to fit the data is:

$$\langle |u(q_x, y=0)|^2 \rangle = \frac{1}{\pi} \int \left(\frac{k_B T}{4\eta q} \tau_m \frac{\tau_m^2(q)}{\tau^2} \left[\frac{\tau}{\tau_m(q)} + \exp\left(\frac{-\tau}{\tau_m(q)} \right) - 1 \right] \right) dq_y \qquad 2.8$$

where τ_m is the fluctuation lifetime, and τ is the camera integration time (Pécréaux *et al*, 2004). Further limits on the application of this model due to

experimental constraints are discussed in section 2.2.4 below.

As seen in figure 2.1, each point along the contour of the vesicle can be written as $r(\theta)=R[1+u(\theta)]$. Expanding the deviations from the average radius, R , into Fourier modes, the coordinates of points along the contour can be written as:

$$r(\theta)=R[1+\frac{1}{2}\sum(c_m\exp(i\,m\theta))] \qquad 2.9$$

where the sum is taken over all possible Fourier modes. The Fourier coefficients can be expressed as:

$$c_n=\frac{2}{a}\int u(z)\exp(-i\frac{2\pi n}{a}z)\,dz \qquad 2.10$$

with $a=2\pi\langle R\rangle$. Here, as in the subsequent data analysis presented in section 2.3, averages are taken as time averages, though they are equivalent to averaging over all available states, assuming the ergodic hypothesis is valid for this analysis.

The measured fluctuation spectrum is then related to the variance of the Fourier coefficients, with a change in variable $q_x=n/\langle R\rangle$:

$$\langle|u(q_x)|^2\rangle=\frac{\pi\langle R\rangle^3}{2}(\langle|c_n|^2\rangle-\langle|c_n|\rangle^2) \qquad 2.11$$

By measuring the variance of each of the Fourier modes, one can calculate the fluctuation spectrum as a function of wave vector for a given vesicle and fit the data to the form proposed by Pécréaux *et al* to obtain an estimate for the bending rigidity and surface tension. Figure 2.2 shows an example of a fluctuation spectrum for a giant vesicle made of DOPC, as well as the spectrum's shape

change with increasing surface tension and increasing bending rigidity. The best fit parameters obtained are: σ = 3 x 10^{-7} N/m^2 and κ = 5 x 10^{-19} J. Increasing surface tension (σ) suppresses all the modes equally (higher σ, same κ), while increasing the bending rigidity (κ) suppresses the higher modes more than the lower modes (same σ, higher κ).

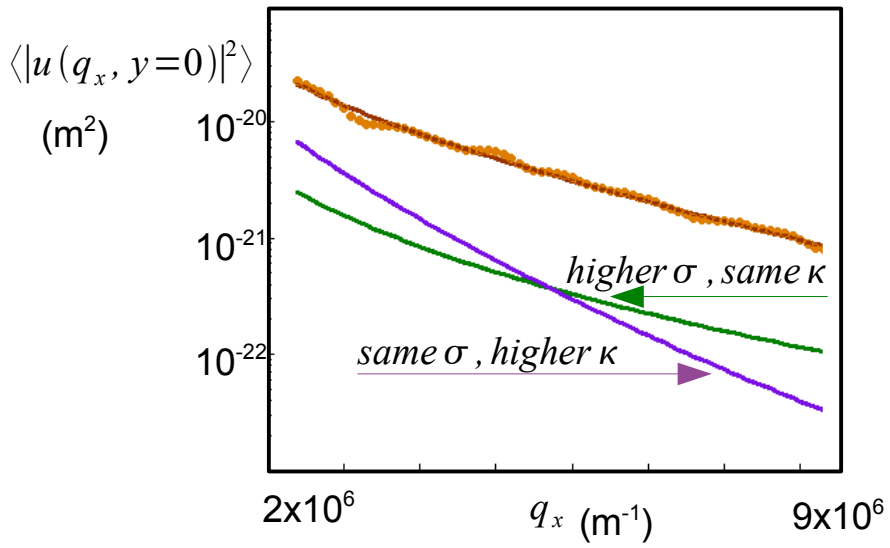

Figure 2.2: Variance spectrum for a vesicle: dots represent data, solid line represent best fit.

2.1.2 Previous measurements of bending rigidity of lipid bilayers

The bending rigidity of lipid bilayers has been measured using different experimental techniques as well as for different lipid composition. Below we present a table summarizing the measured values for bending rigidity found in the literature. Table 2.1 is an expansion of table 2 from Pécréaux *et al* (2004). Table 2.2 shows reports of bending moduli for bilayers formed of the lipid used in

our experiments, DOPC (di-oleoyl-phophatidyl-choline), as a function of temperature.

Lipid	Bending Modulus κ (10^{-20} J)	Technique	Reference
EPC	10 – 20	Correlation fluctuations	Schneider
EPC	4 – 5	Vesicle contour analysis	Faucon
EPC	11.5	Vesicle contour analysis	Duwe
EPC	8	Contour analysis	Mutz
EPC	2.5	Electric field	Kummrow
EPC	6.6	Vesicle contour analysis	Méléard
EPC	4.25 +- 0.87	Refined vesicle contour analysis	Pécréaux
SOPC	20	Tethers on vesicle	Bo
SOPC	9	Micropipette	Evans
SOPC	14.4	Vesicle contour analysis	Häckl
SOPC	12.7	Vesicle contour analysis	Méléard
SOPC	18.1	Vesicle contour analysis	Gerbeaud
SOPC	12.7	Vesicle contour analysis	Döbereiner
SOPC	12.6 +- 2.6	Refined vesicle contour analysis	Pécréaux
SOPC	15.5	Tethers on vesicle	Song1
SOPC:CHOL ratio 1:1	24.6	Micropipette	Evans
SOPC:CHOL ratio 1:1	29.6 +- 3.3	Refined vesicle contour analysis	Pécréaux
SOPC:POPS ratio 98:2	15.5	Tethers on vesicle	Song1
SOPC:POPS ratio 84:16	16.1	Tethers on vesicle	Song1
SOPC:POPS:CHOL ratio 39.2:0.8:60	36	Tethers on vesicle	Song

EPC: egg phosphatidyl-choline
SOPC: stearoyl-oleoyl-phosphatidyl-choline
CHOL: cholesterol
POPS: 1-palmitoyl-2-oleoyl-phosphatidyl-serine

Table 2.1 Bending rigidity of PC membranes reported in the literature.

Bengind rigidity (x 10^{-20}J)	Temperature (ºC)	Reference
7.15	45	Pan et al, 2008
7.65	30	Pan et al, 2008
8.5	18	Rawicz et al, 2000
8.4	15	Pan et al, 2008

Table 2.2 Bending rigidity of DOPC membranes as a function of temperature.

We used DOPC for our samples and experiments were conducted at room temperature (20-24 ºC). From table 2.2 we expect to measure a value for bending rigidity of 8 x10^{-20} J.

Note that the bending rigidity measurements reported vary considerably. This is true for membranes composed of lipids with different fatty acid chains, or with different relative concentrations of lipid species. However, values of bending rigidities reported for membranes of the same lipid composition vary by up to a factor of 10, depending on experimental technique. For egg PC the values are from 2.5 to 20 x10^{-20} J, while for SOPC they are from 9 to 20 x10^{-20} J. The values for DOPC are less variable, though they are determined only from two different measurements, and no confidence intervals or error bars were provided.

2.2 Experimental Methods

2.2.1 Making GUV

GUV were prepared following the electroformation technique described by Poole and Losert (2007). Briefly, 5-7 μL of lipids (99:1 %mol DOPC:N-Cap-Biotin-PE, Avanti Lipids) suspended in chloroform (20 mg/ml) were dried on two

pieces of (indium-tin-oxide)-covered glass (1 x 3 inches, Rm = 5 – 15 ohms, Delta Technologies), forming a thin coat. The glass pieces each have a copper wire attached with silver paste on the ITO-covered side. The slides were placed in a vacuum chamber for at least 20 minutes and up to a few hours to evaporate all traces of solvent. A Teflon ™ spacer 1 mm (0.043 inches) thick was placed on top of the lipid film on one glass piece, and secured with vacuum grease to prevent it from sliding. Figure 2.3 shows a schematic of this chamber.

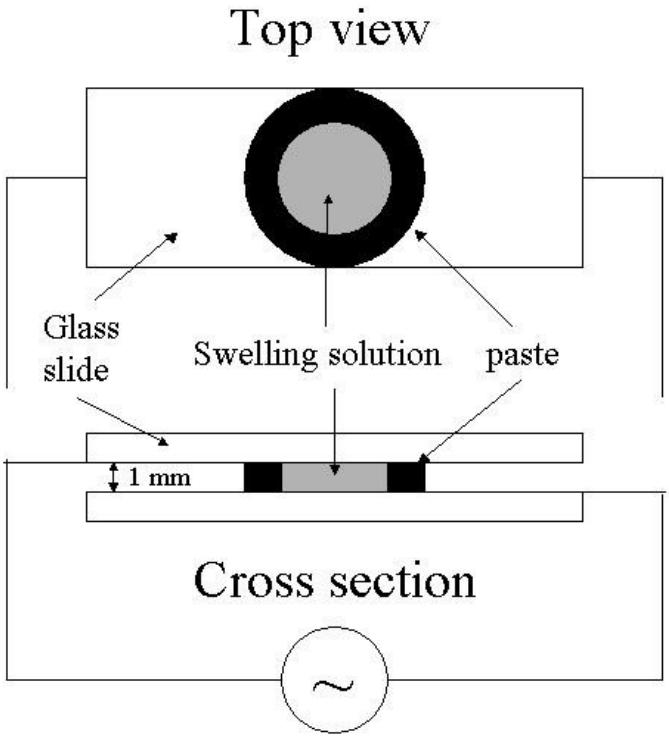

Figure 2.3: Schematic of electroformation chamber.

The chamber was filled with about 0.5 ml of 0.3 M sucrose solution (Fischer Scientific) and the other glass was placed on top to seal the chamber

with the lipid-film-side down. The arrangement was held in place using medium sized binder clips. The chamber was placed on top a hot plate (Cimarec, Barnstead) set a temperature of 75 ºC. The temperature inside the sucrose solution was measured with a temperature probe and was around 45 ºC, above the melting point of both DOPC and PE. This is done to ensure uniform mixing of the lipids during vesicle formation.

The output of a function generator (BK Precision 3011B) was connected to the chamber, passing a sinusoidal alternating current through the fluid inside the chamber. The signal was set with a frequency of 10Hz and the voltage rms value was increased from 0.5 V to 1.5 V in ten steps of 0.1 V over the course of one hour. Then the signal was left at 10 Hz and 1.5 V for 3 hours. Finally, the signal was changed to 4 Hz and 1.5 V, and left running for 1 hour. The sample was collected in a microcentrifuge tube using a Pasteur pipette and stored at 4 ºC. GUV prepared this way were used within 24 hours of finishing this process.

2.2.2 Sample preparation and setup

Viewing chambers were constructed as follows: using nail polish, a coverslip (No. 1, 22x22 mm, VWR) was attached to a microscope glass (1X3 inches, VWR) covering a 1-cm hole pre-drilled into the glass. The polish was allowed to dry, and the chamber was left open. A schematic of the viewing chamber is presented in figure 2.4.

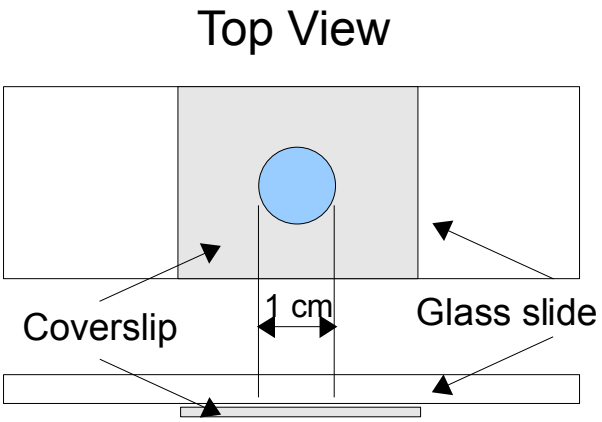

Figure 2.4: Schematic of viewing chamber

When preparing a sample for viewing, first 2 to 5 μL of GUV were placed on the cover slip in three droplets. Then, 100 μL of a solution containing glucose (0.34 M, EMD) and peptide (myristoylated N-terminus of Arf1, Anaspec) was added while the sample chamber was on the microscope. This minimizes the flows to which GUV are subjected, minimizing deformations and ruptures. The peptide was kept in a PBS (8 g/L NaCl, 0.2 g/L KCl, 1.44 g/L Na_2HPO_4, 0.24 g/L KH_2PO_4) solution and the final concentration of peptide inside the sample ranged from 0.2 μM to 2 μM .

Samples were viewed under a Nikon inverted microscope at 60x or 100x magnification with an 1.40 NA, oil immersion lens. Images were taken with a Photron Fastcam at 125 frames per second. Vesicles of radius between 10 and 60 μm that had no noticeable deformations, like tubes or bulges, and were not

visibly in contact with other vesicles were selected for imaging.

Images of the fluctuating vesicles were taken slightly out of focus. The lipid bilayer thickness is below optical resolution, and even though the difference in index of refraction between the sucrose solution inside the vesicle and the glucose solution outside the vesicle is enough to see the 'shadow' of the lipid bilayer, the resulting in-focus images are not sufficient for automated image processing. Taking the images with the vesicle slightly out of focus produces diffraction rings, and the lipid bilayer is assumed to behave the same way as the edge of these diffraction rings, where dark pixels meet light pixels, as in figure 2.5. The contour of the vesicle was found using a modified Snake Demo program for Matlab (interface by Dejan Tomazevic, Snake functions by Chenyang Xu and Jerry L. Prince) as explained in section 2.2.3.

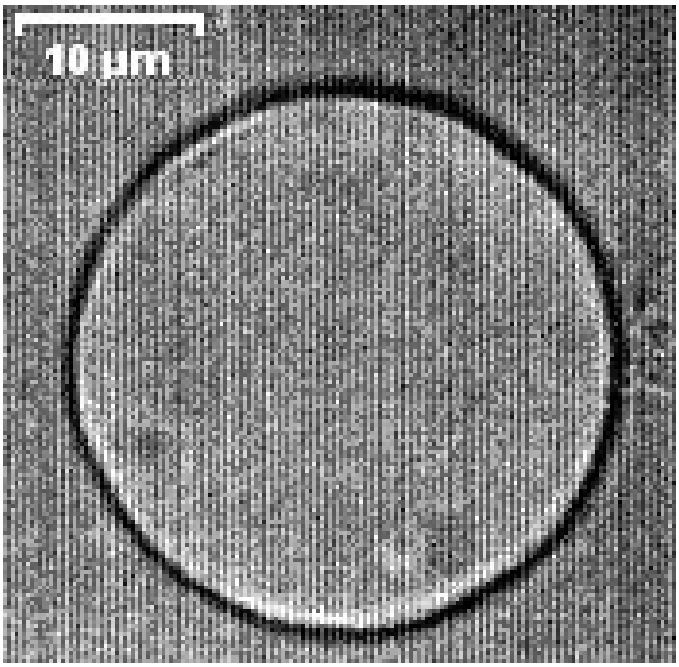

Figure 2.5: Image of GUV slightly out of focus. Diffraction rings are used for automated edge detection – see section 2.2.3 for details.

2.2.3 Image processing: Snake Algorithm

The contour of the fluctuating vesicle was obtained by extracting the edge of the slightly-out-of-focus vesicle using an active contour algorithm and separating the points along the contour by an equal distance along the contour. Several images (800 to 1000) for a single vesicle were used to calculate an average radius, measured from the center of the vesicle. This center was found by averaging the x- and y-positions of the points along the contour. Pécréaux *et al* calculated the center of the vesicle by weighing the points along the contour according to the angle between them. We found that this weighing was not necessary for our data, since the points along the contour are many (around 400) and equally spaced, so both methods give similar results. We used a modified version of the Snake Demo for Matlab. A brief description of snakes and the algorithm follows.

A snake is a spline, or an active curve on an image, that minimizes the energy landscape provided by the internal properties of the snake, such as rigidity and tension, and external constraints. The external energy constraints are derived from the image and are such that the energy is minimum at the features of interest, like boundaries or edges. The energy that the snake minimizes is of the form:

$$E = \int \left(\frac{1}{2}\left(\alpha |x'(s)|^2 + \beta |x''(s)|^2\right) + E_{ext}(x(s))\right) ds \qquad 2.12$$

where α and β control the snake's rigidity and tension, and x' and

x'' denote first- and second-order derivatives of x with respect to the contour variable *s*, respectively (Kass *et al*, 1988).

A snake that minimizes this energy must satisfy the Euler equation: $\alpha x''(s) - \beta x''''(s) - \partial_x E_{ext} = 0$. This equation can be seen as two terms representing an internal force that keeps the snake from stretching and bending balanced by a third term representing an external force pushing the snake towards the edge. The snake is made dynamic by treating x as a function of time, as well as a function of s. The partial derivative of x with respect to time is set equal to the force-balance in the previous equation. The equation can then be discretized and solved iteratively, until the snake stabilizes and the derivative of x with respect to time is zero (Xu and Prince, 1998).

In order to find the edge of an object, the external energy in the snake equation is typically equal to the norm of the intensity gradient in gray-scale images, or to the intensity itself in black and white images. Some processing of the original images might be required in order to get the desired features shown as darker pixels before applying the edge detection algorithm. In our images the feature of interest is the interface between the diffraction rings, where dark pixels and light pixels meet. The edge detection algorithm can be used iteratively in an image sequence, with the final snake of image n serving as the initial guess of image n+1. This works adequately as long as the object from which the edge is extracted does not move much from one image to the next.

The average radius of the vesicle was calculated by averaging the radii

obtained for all vesicle images. The modified Snake Demo program interpolates the positions of points along the snake along the x- and y-directions simultaneously, to ensure that the points along the contour are evenly spaced. This gives equal weight to the x- and y-positions of the points along the contour when calculating the center for a single image. For each frame, the center of the vesicle was then found by averaging the x- and y-positions of the equally-spaced points along the contour. The radius was then measured as the average Euclidean distance between this center position and the points along the contour. Figure 2.6 shows an image of a fluctuating vesicle, along with the snake found by our edge-detecting algorithm. The feature of interest in the edge-detection algorithm is the edge between the black and white diffraction rings.

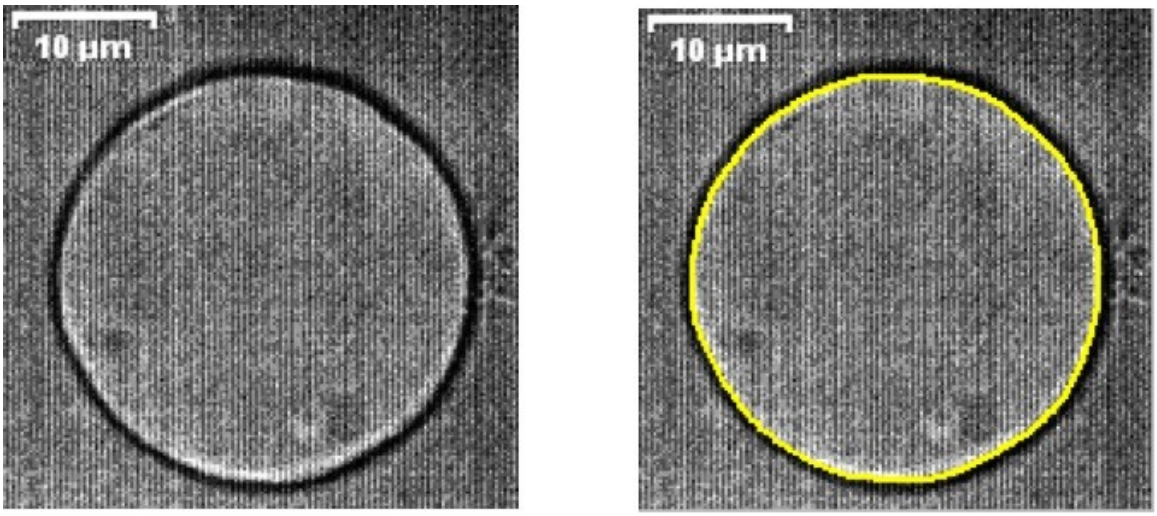

Figure 2.6: Picture of a GUV under bright field microscopy. Left: GUV. Right: GUV with snake superimposed in yellow.

2.2.4 Fitting procedure and noise cutoff

The correction due to integration time is included explicitly in our fitting routine. The function fitted was the same presented by Pécréaux *et al* and in

section 2.1.1 above. We used a program with a modified Newton method for fitting this equation to our data points, written by Hernan Zhou. The fitting program works well for our data. The program crashes when guesses for bending rigidity are negative. It also ignores negative values of surface tension and complex values of bending rigidity, leading to situations where the final 'best fit' parameters have no reasonable physical interpretation.

The fit should be limited to variances above noise level, mode numbers corresponding to wavelengths shorter than pixel size and optical resolution, and mode numbers higher than n=5 due to deviation of the model for flat membranes and the model for curved membranes.

To determine the noise cutoff, we followed the image processing steps and found the variance spectrum for images of a 5-micrometer silica bead that was stuck to the cover slip and thus not fluctuating. Since the bead was not fluctuating, any measured fluctuations can be reasonably considered to be due to image processing artifacts. Figure 2.7 shows the fluctuation spectrum and the picture of the bead used to obtain this spectrum. The highest value of the variance of the fluctuations of the bead is about $10^{-22}\,m^2$. Hence, variances below this value were considered noise and were subsequently ignored when fitting the variance spectra from the vesicle images.

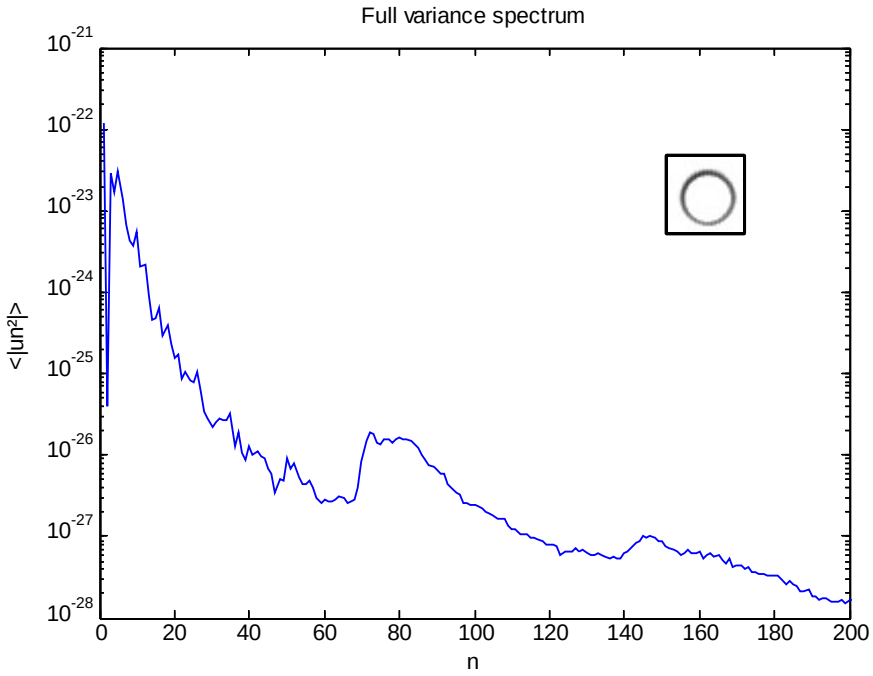

Figure 2.7: Fluctuation variance spectrum for non-fluctuating bead; variance for each mode number vs mode number, n. INSERT: Processed image of 5μ bead – dark ring represents where dark pixels meet bright pixels.

Wave vector values greater than 5 x 10^{6} m^{-1} were also ignored, since fluctuations smaller than a pixel size (0.2 x 10^{-6} m) are not expected to be detected. This is probably a conservative measure given that our contour detection routine can detect the position of the contour with sub-pixel resolution.

2.3 Results

2.3.1 Variance spectra of GUV

We measured the variance spectra of several GUV from the same batch. For some cases, as for the 030610 batch, most of the variance spectra fall

closely together, suggesting that the GUV sampled have similar physical properties. Figure 2.8 shows an example of variance spectra for several GUV in the absence of peptide from the same batch.

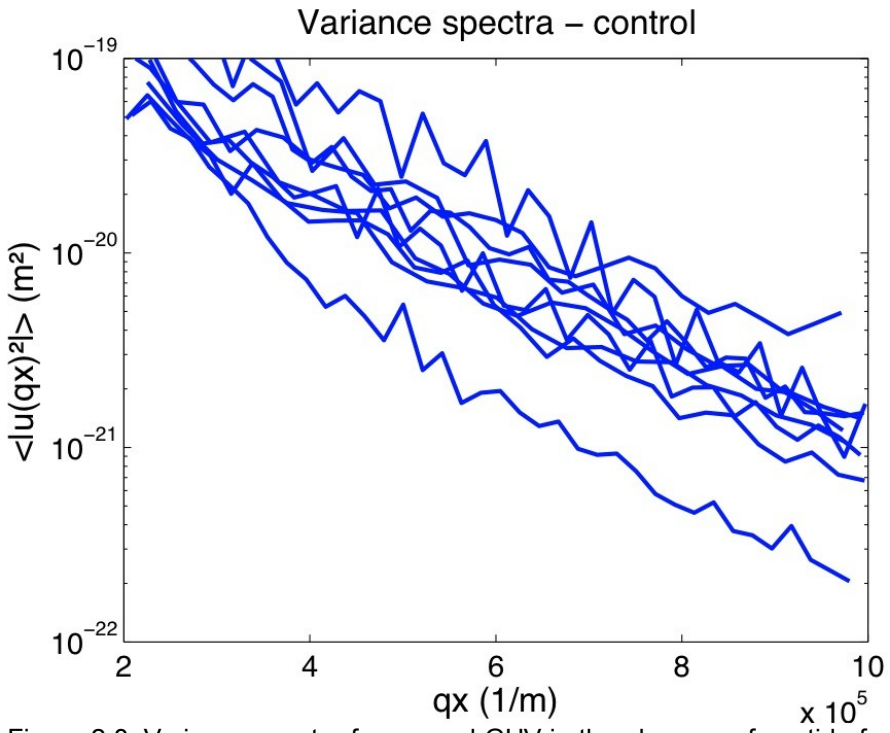

Figure 2.8: Variance spectra for several GUV in the absence of peptide from the sample from 030610.

For other samples, however, the variance spectra of different GUV did not look similar. Figure 2.9 shows variance spectra from several GUV in the absence of peptide from the sample from 022110. The spectra are quite different in magnitude and shape, indicating that the GUV sampled from this batch presented different values of bending rigidity and surface tension.

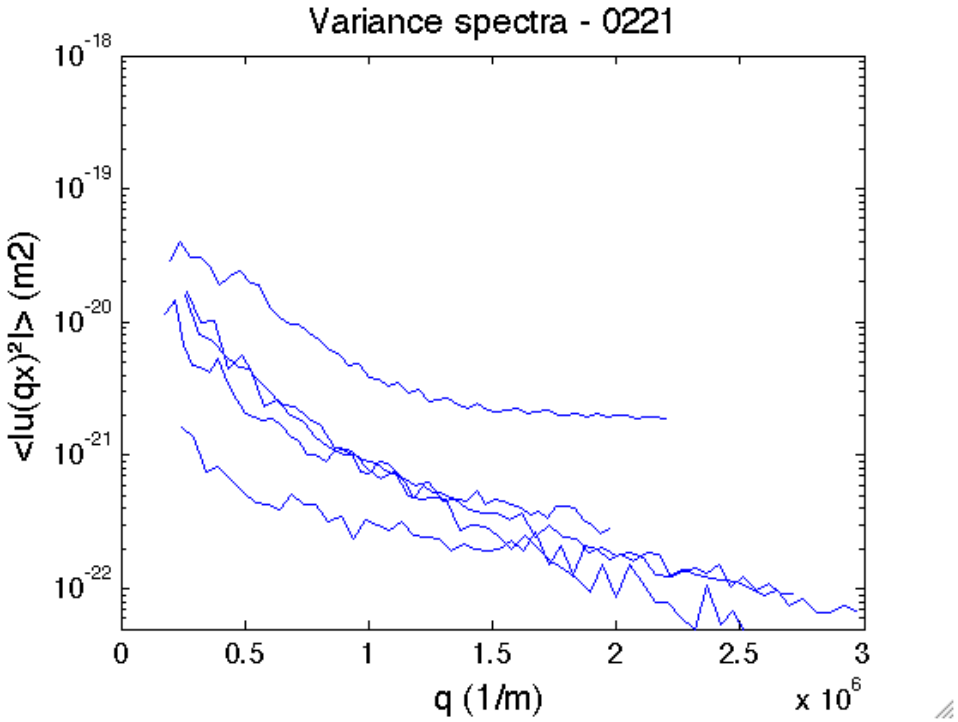

Figure 2.9: Variance spectra for several GUV in the absence of peptide from the sample from 022110.

The large variability of the variance spectra among GUV from the same batch makes drawing conclusions from these spectra difficult when the peptide concentration is increased, since any changes observed will likely fall within the large error bars. For GUV in the presence of peptide, only the data from batches that showed a somewhat consistent form or shape for variance spectra from GUV without peptide added were considered for further analysis. These results will be presented in section 2.3.4.

2.3.2 Bending rigidity and surface tension are independent of vesicle radius

The bending rigidity and surface tension can be obtained by fitting the variance spectra to the equation presented in section 2.1.1. We fit the variance

spectra for GUV in the absence of peptide from different batches. Figure 2.10 shows the bending rigidity of the GUV sampled as a function of average vesicle radius for GUV from different batches. The bending rigidity should not depend on vesicle size, since it is assumed that it is an intrinsic property of the material. The bending rigidities obtained by the fits ranged from 9 $x10^{-20}$ J to 165 $x10^{-20}$ J, about 1-20 times larger than the values reported in the literature.

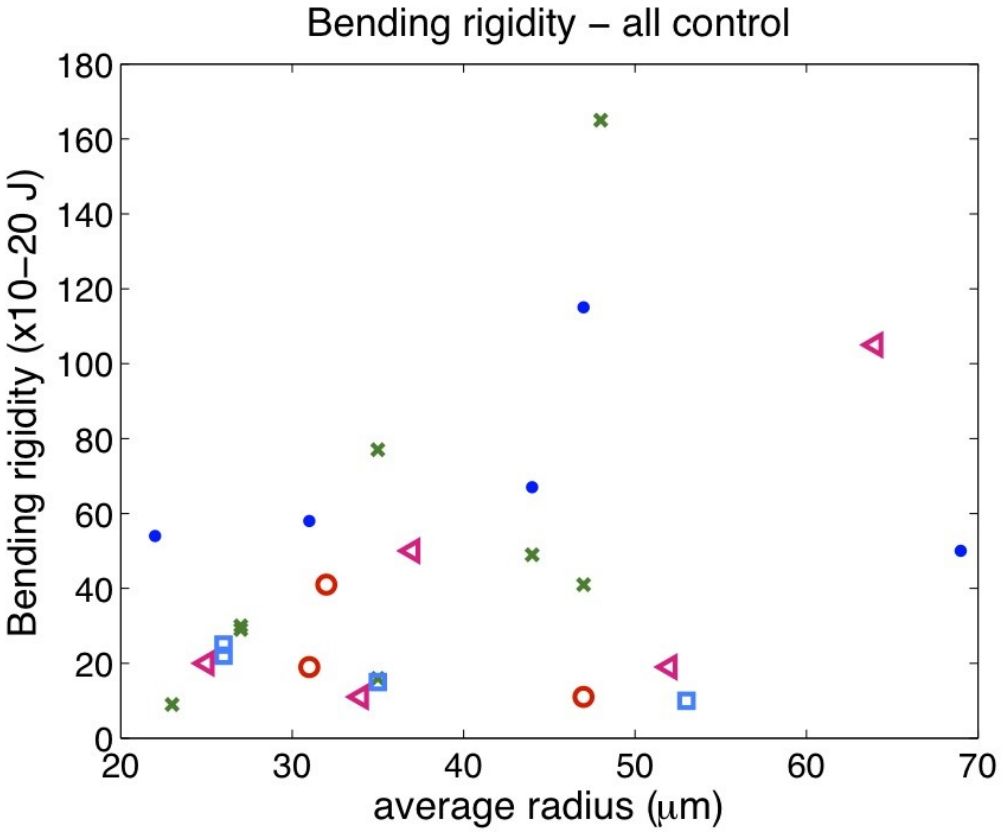

Figure 2.10: Bending rigidity as a function of radius obtained from fits to variance spectra from GUV in the absence of peptide. Different symbols represent different samples. Closed circles (02/12/2010) and crosses (03/06/2010) have variance spectra fall along same line. Open circles (02/21/2010), open squares (03/08/2010) and open triangles (06/22/2010) have variance spectra that have wide variability.

The bending rigidities of all the GUV from the same batch were compared to the values obtained for the rest of the batches using one-way ANOVA (analysis

of variances). This technique compares the between-group variability and the within-group variability to determine if the means of the groups are the same. The calculated F value for the bending rigidities from the 5 different samples is 0.37, whereas the F value for 5 groups with 26 total data points is 2.84, for a P value of 0.05 (Walpole and Myers, 1992). Calculated F values higher than this would mean that the null hypothesis (that the means are the same) is rejected, and that there is a 5% chance that the calculated F value could be obtained through random chance alone. Since the calculated F value is smaller than the F value for the given degrees of freedom, the null hypothesis is accepted, and the means are considered to be the same. Hence, the bending rigidity of GUV in the absence of peptide does not change form one batch to the other. However, one must keep in mind that there is a large variability not only in the bending rigidities obtained from the fits, but also in the shape of the variance spectra of the fluctuating GUV.

The fits to the variance spectra also have as a fitting parameter the surface tension of the lipid bilayer. Figure 2.11 shows the surface tension obtained form the fits for GUV in the absence of peptide from different batches as a function of average vesicle radius. Unlike bending rigidity, surface tension is not a property of the material, but is context dependent. Changes in environmental conditions, such as temperature and contact area, could potentially change this parameter.

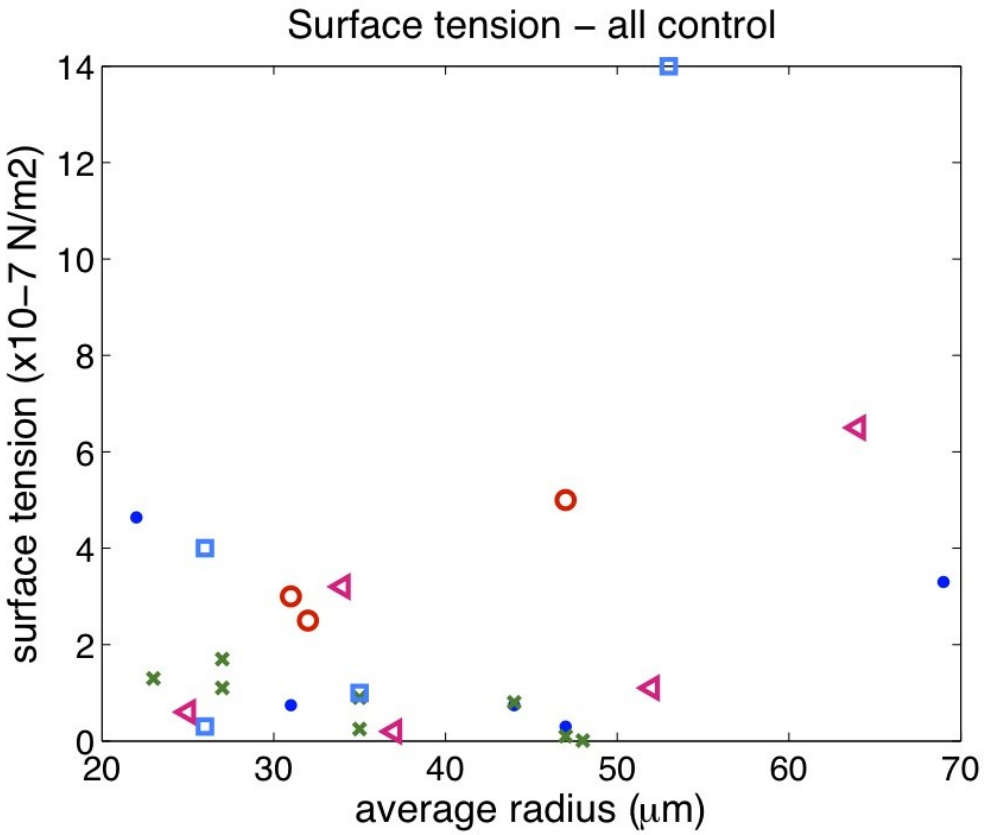

Figure 2.11: Surface tension for GUV in the absence of peptide as a function of radius. Closed circles (02/12/2010) and crosses (03/06/2010) have variance spectra fall along same line. Open circles (02/21/2010), open squares (03/08/2010) and open triangles (06/22/2010) have variance spectra that have wide variability.

We also performed a one-way ANOVA comparing the surface tension obtained by the fits for GUV from different batches. The calculated F value for the surface tensions is 0.38, while the F value for 5 groups and 26 total data points is 2.84 for a P value of 0.05. Since the calculated F value is less than the F value for the given the degrees of freedom, the null hypothesis is accepted, and the means are considered to be the same. The same caveat as with bending rigidity applies. Namely, that even if the analysis leads one to conclude that surface tension of GUV in the absence of peptide does not change from one batch to the next, there is large variation in the values obtained from the fits, as well as the

shapes of the variance spectra for which the fits are made.

2.3.3 Bending rigidity vs surface tension

As noted in section 2.2.2, in our experimental setup the surface tension on the membrane is set in part by non-specific interactions between the vesicle and the cover slip. On the other hand, bending rigidity is an intrinsic property of the material. Figure 2.12 shows that there is no detectable relationship between the bending rigidities and surface tensions found by the fits.

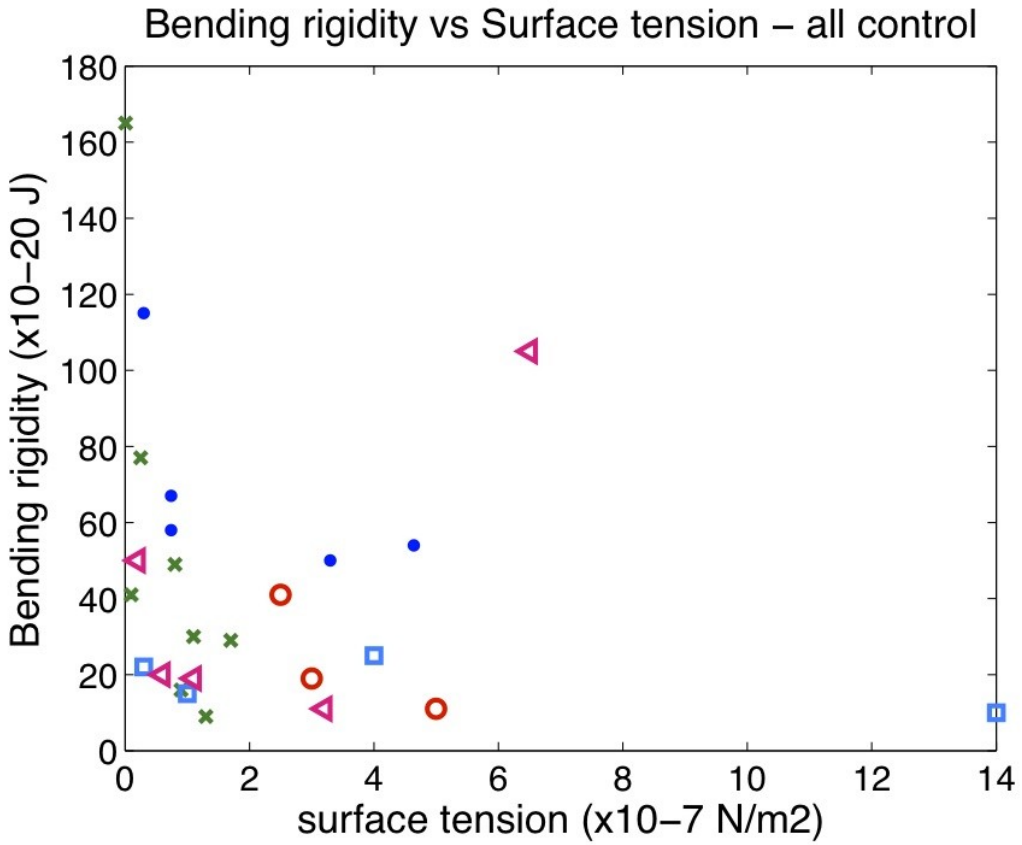

Figure: 2.12 Bending rigidity of GUV in the absence of peptide as a function of surface tension.

2.3.4 Addition of Myrisoylated N-terminus of Arf1 peptide changes the shape of the fluctuation variance spectra

We obtained variance spectra for GUV in the presence of varying concentrations of peptide as described in section 2.2.2. Figure 2.12 shows the variance spectra for GUV in the absence of peptide and in the presence of two concentrations of peptide for the batch from 030610. The variance spectra for GUV in the absence of peptide (blue lines) all fall closely together, so comparison with the spectra for GUV in the presence of peptide can be made.

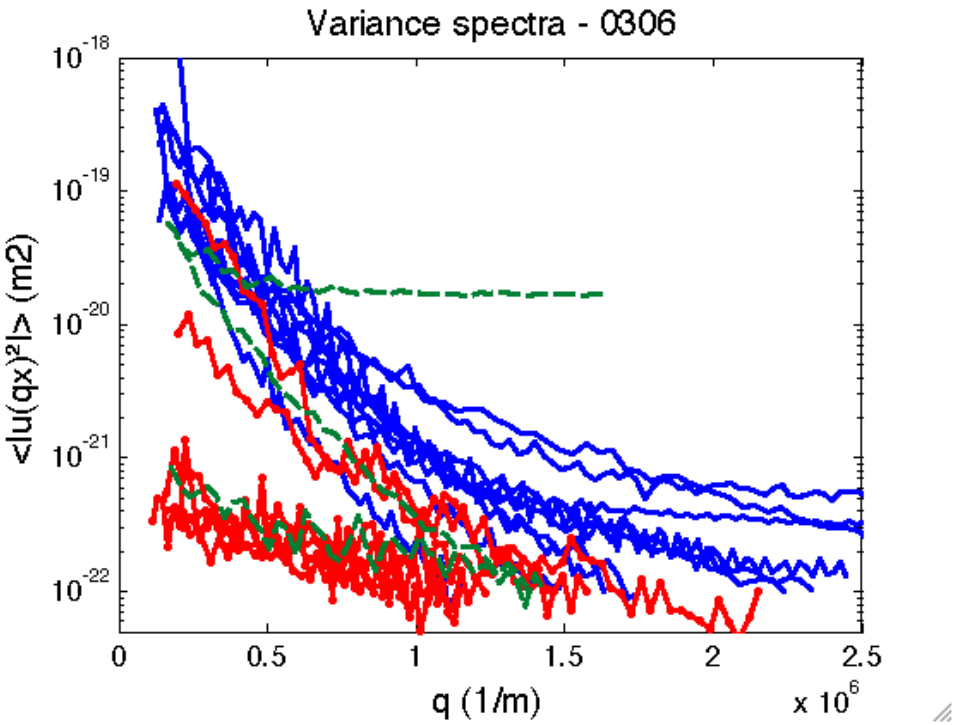

Figure 2.13: Variance spectra for GUV from the batch 030610. Blue lines represent no peptide, red lines represent 0.2 μM myr-Arf1 N-terminus, and green lines represent 2.2 μM myr-Arf1N-terminus.

There are only 3 spectra for GUV with 2.2 μM peptide and each have a different shape. One has a very high noise level, which can be seen by the

constant variance of around 10^{-20} m^2 for a wide range of wave vector values. For the other two spectra, one falls within the group of the spectra from GUV in the absence of peptide and the other does not. Hence, no conclusion can be made about the effect of 2.2 μM peptide on the fluctuations of GUV.

For the 0.2 μM peptide sample, most of the spectra fall close together in what appears to be a separate group from the no peptide sample. However, two of the low peptide spectra seem to be closer to the no peptide spectra than the others. Since there are only a few spectra for each sample, one cannot conclude that the two populations are the same or different based on this plot alone. This phenomenon was observed as well on the other samples in which the variance spectra of GUV in the absence of peptide fall close together. We found no relation between vesicle size and variance spectra shape.

In addition, the cluster of variance spectra from GUV in the presence of peptide are not fit well by the model, as shown in an example in figure 2.13. Hence, comparisons of the bending rigidity and surface tension cannot be made. It is possible that association of the peptide on the membrane affects the membrane in such a way that the assumptions underlying the model of flicker spectroscopy, such as assuming the membrane is homogeneous throughout, no longer apply. We note that this possibility is not considered in any of the current models of COPI vesicle transport, nor in the hypotheses we listed in section 1.4. It is not possible in this experimental setup to measure parameters such as peptide concentration on the membrane that could allow one to distinguish the

two groups of variance spectra. Speculations about the possible interpretation of these results as well as possible future experiments are presented in chapter 5.

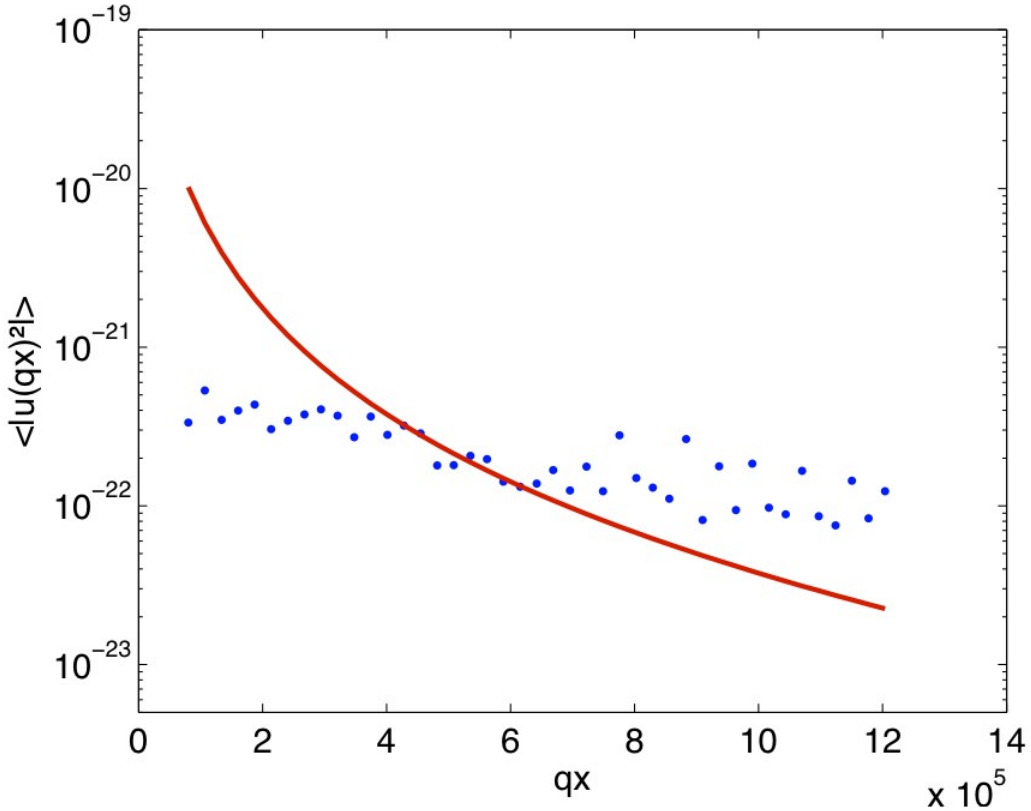

Figure 2.14 Variance spectra of vesicle in presence of peptide. The model (red line) does not fit the data (blue dots) well.

2.3.5 Addition of buffer alone does not change the variance spectra

The changes in variance spectra shape were observed for concentrations of peptide as low as 0.2 μM. This led us to hypothesize that perhaps the buffer was having an effect. In order to test this hypothesis, we repeated the experiments as before, but adding PBS buffer without any peptide. Figure 2.14 shows a representative sample of the results we obtained.

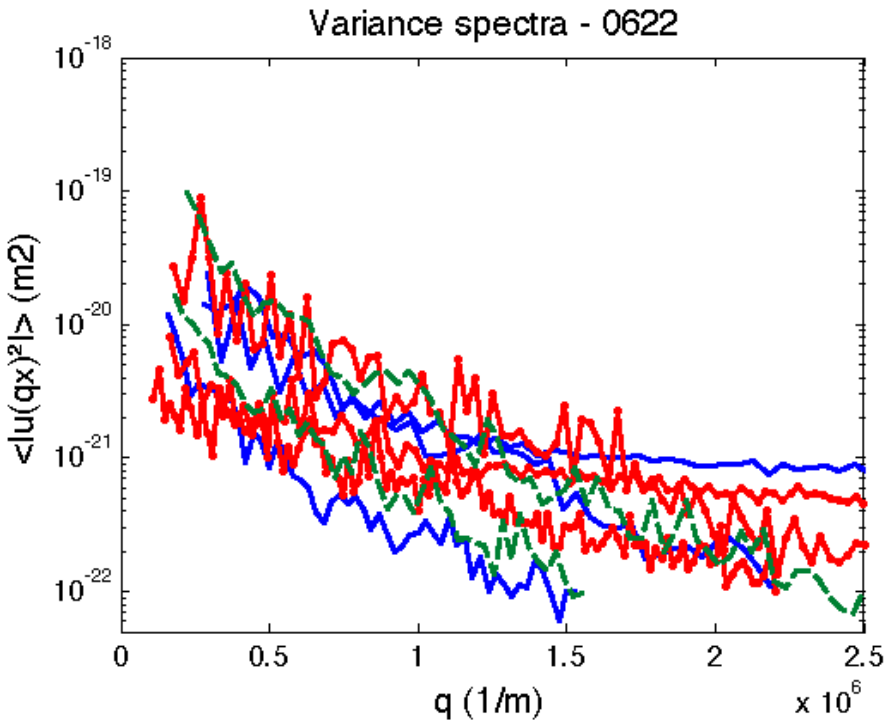

Figure 2.15: Variance spectra GUV from sample 062210. Blue: no peptide; Red: buffer (PBS); Green: 2.2 μM myr-Arf1(2-17).

The variance spectra for GUV in the absence of peptide had a large variability, making comparison between data for different conditions troublesome. The variance spectra for GUV in the presence of PBS buffer (red lines) fall within the variability of the control GUV. From this we conclude that the addition of buffer has no effect on the variance spectra of fluctuating GUV. The variance spectra for GUV in the presence of 2.2 μM peptide also fall within the range of variance spectra for the control GUV.

Unlike the data from 030610, the shapes of the variance spectra for GUV in the presence of buffer and peptide are close to what is expected based on the model for flicker spectroscopy. However, there are only a few variance spectra for

each condition. Hence, no definitive conclusion can be drawn about any changes in bending rigidity and surface tension of lipid bilayers due to the action of PBS buffer or peptide.

2.4 Summary

Flicker spectroscopy provides a way to estimate the bending rigidity and surface tension of GUV. We observed limited reproducibility in the fluctuation variance spectra of GUV made of DOPC, with some samples having GUV displaying similar variance spectra while GUV from other samples presented highly variable variance spectra. Though bending rigidities and surface tension estimated from fitting the measured variance spectra to the equation from flicker spectroscopy are statistically the same for all GUV in all samples, the large variability in the calculated values as well as the shape of the spectra from which these values are obtained makes it nearly impossible to draw definite conclusions about any effect that adding peptide could have on the membrane.

Addition of buffer alone to the outside solution shows no detectable effect on the fluctuations of GUV. Some GUV in the presence of peptide display a variance spectra with a different shape as that predicted by flicker analysis, indicating that the membrane may no longer be homogeneous and raising the possibility of additional physical effects of Arf1 beyond the 6 possible effects listed in chapter 1.4.

Chapter 3: Pulling and retraction of tethers

The pulling and retraction of thin, long tubes from a GUV, called tethers, provides a way of measuring the large-scale properties of membranes by directly measuring the forces required to bend lipid bilayers, and the kinetics of the retraction. When the retraction speed is constant, this retraction speed is directly proportional to the bending rigidity of the membrane. When the retraction speed is not constant, the length of the retracting tether is logarithmic in time. This chapter presents data for the pulling and retraction of tethers from GUV in the presence of varying concentrations of the myristoylated N-terminus of Arf1. Definite conclusions about the effect of the peptide on the force required to pull a tether and on the bending rigidity of lipid membranes, cannot be drawn due to wide variations between and within batches of GUV. However, it is clear that adding myristoylated N-terminus of Arf1 to the outside of GUV does not make the formation of tethers significantly easier.

3.1 Theory of the pulling and retraction of tethers from GUV

3.1.1 Stability of static tethers

Experiments for measuring the bending rigidity and surface tension of lipid bilayers include the pulling of long, thin tubes called tethers from giant vesicles, and the deformation of the membrane locally into a tubular segment under longitudinal tension, as seen in figure 3.1. The precise structure of the tether is not known, since it is smaller than the diffraction limit of bright field microscopy. However, it is often assumed that the tether consists of a single lipid bilayer and has a roughly cylindrical shape (Bukman *et al*, 1996). Using energy functional analysis of lipid membranes, Bukman *et al* found the conditions under which stable cylindrical tubes subjected to longitudinal tension can exist. From these results, and by making assumptions valid in our experimental setup, we can obtain an expression for the critical force necessary to maintain stable cylindrical tubes, and we find the relationship of this force with the tether's radius and the membrane's bending rigidity. In this section, I will present the theory of stable tethers. The theory of the dynamics of pulling tethers will be presented in section 3.1.2.

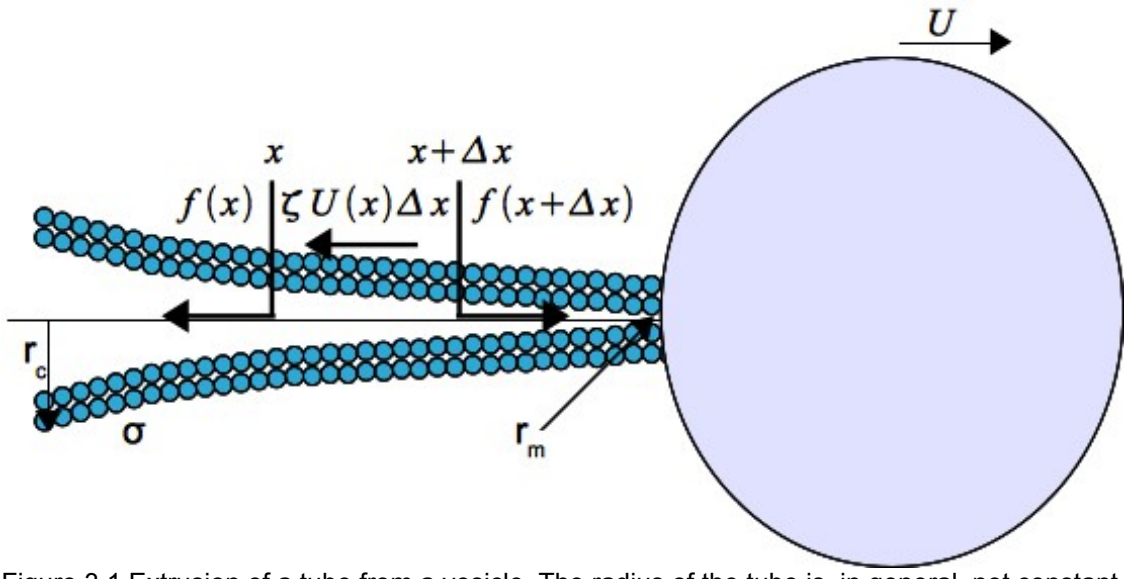

Figure 3.1 Extrusion of a tube from a vesicle. The radius of the tube is, in general, not constant, with a value of r_c at the position where the tube joins the vesicle and r_m where the tube joins the bead. The friction exerted on the tube by the surrounding fluid generates a force gradient along the side of the tube, with a coefficient of friction (ζ) proportional to the viscosity of the fluid.

The energy functional of a tether connected to a lipid reservoir and subject to a longitudinal force can be constructed by starting from the Canham-Helfrich energy functional and adding terms appropriately. The Canham-Helfrich energy functional, first derived by Canham (1970) and Helfrich (1973), of the energy cost to bend a planar sheet is:

$$F = \frac{\kappa}{2} \int dA (c_1 + c_2 - c_0)^2 \qquad 3.1$$

where c_1 and c_2 are the principal curvatures, c_0 is the spontaneous curvature, which arises due to the preferred alignment of the individual lipid molecules forming the membrane, and κ is the local bending modulus, and has units of energy.

To this energy functional, one can add a second term for the elastic

stretching energy due to the difference in area between the inner monolayer and the outer monolayer. This term introduces the area-difference-elasticity (ADE) model, first derived by Miao *et al* (1994),

$$F = \frac{\kappa}{2}\int dA(c_1 + c_2 - c_0)^2 + \frac{\bar{\kappa}\pi}{2AD^2}(\Delta A - \Delta A_0)^2 \qquad 3.2$$

In the ADE model, the areas of the different monolayers are not fixed, but can expand under stress. Each monolayer has a preferred area based on the number of lipid molecules that form it, but can have an actual area that is larger or smaller, due to the interactions with the other monolayer. This area difference has an energetic cost, and the effect of stretching is important. In this equation, $\bar{\kappa}$ is the non-local bending modulus. It has units of energy, and arises from the local bending moduli of the monolayers, as well as from the preferred or relaxed areas occupied by them. ΔA is the actual area difference between the inner and outer monolayers, ΔA_0 is the relaxed area difference, that is, the difference between the relaxed or preferred areas of the monolayers, and A is the total (average) area of the bilayer. D is the distance between the neutral surfaces, or the position of action of planar tensions, of the monolayers and can be taken to be the bilayer thickness. For a detailed derivation of the ADE term starting from the area stretching or compressing elasticity of lipid molecule's interactions, see Miao *et al*.

There is an energy contribution by the longitudinal force keeping the tether in place, proportional to the point force applied, F_0 , and the length of the

tether. Finally, area and volume constraints have to be included in the final energy functional. The Lagrange multipliers σ and P can be interpreted as surface tension and pressure respectively in the micropipette experimental setup. The complete energy functional of a membrane tether can be written as:

$$F=\frac{\kappa}{2}\int dA(c_1+c_2-c_0)^2+\frac{\bar{\kappa}\pi}{2AD^2}(\Delta A-\Delta A_0)^2-F_0L+\sigma A-PV \qquad 3.3$$

The contribution of the Gaussian curvature is omitted, since the topology of the vesicle does not change, and the Gaussian curvature does not contribute to the total free energy.

Assuming the tether is on average a cylinder of radius R_0 with small fluctuations in the direction normal to the cylinder surface, $R(z,\theta)=R_0(z,\theta)+\epsilon(z,\theta)\hat{n}$, one can then expand the energy functional up to second order in these fluctuations, $\delta F=\delta^{(1)}F+\delta^{(2)}F+O(\epsilon^3)$.

Having stable tethers implies that the energy is at a minimum; the first variation of the energy functional is equal to zero, and the second variation is positive. From the first condition one obtains the following relationships (see Bukman *et al* for details):

$$P=\frac{F_0}{\pi R_0^{\,2}}-\frac{2\kappa}{R_0^{\,3}}(1-R_0c_0)-\frac{4\bar{\kappa}\pi^2L}{AR_0^{\,2}}(1-\Delta a_0) \qquad 3.4$$

$$\sigma=R_0P+\frac{\kappa}{2R_0^{\,2}}(1-R_0^{\,2}c_0^{\,2}) \qquad 3.5$$

with $\Delta a_0=\bar{\Delta A}_0/2\pi LD$ and where $\bar{\Delta A}_0$ is the preferred area difference between the inside and outside monolayers of the tether due to the electrostatic

interactions of the lipid head groups and tail groups in each monolayer. The second condition leads to the conclusion that fluid membrane tethers are only stable when F_0 > 0, that is when they are under tension (Bukman *et al*, 1996).

From the first equation above, one can derive a simplified relationship between the terms by making the following assumptions: 1) the length of the tether is relatively short (L ~ 1000 R_0); 2) the membrane is unlikely to have a preference for curvature on the length scale of the tether radius ($c_0 R_0$ >> 1); and 3) the pressure difference between the inside and the outside of the vesicle is negligible. These assumptions are reasonable for our experimental setup, and they lead to the following expression: $F_0 = (2\kappa\pi)/(R_0)$ which shows that the critical force for having stable tethers is directly proportional to the bending rigidity and inversely proportional to the tether radius. This relationship is valid only for constant values of surface tension, since bending rigidity and surface tension are related through the tether radius (see equation 3.17). From this we can assume that the higher the force required to pull a tether from a given vesicle, the higher the bending rigidity of the membrane, if the tether radius is somewhat constant from one tether pull to the other.

3.1.2 Dynamics of pulling tethers

Evans and Yeung developed a theory of the dynamics of tether pulling, in which they assumed the radius of the tether remained constant throughout. However, there is no reason to believe *a priori* that this should be the case.

Rossier *et al* developed a theory of the dynamics of pulling tethers for the general case, of varying tether radius. In their theory, the surface tension is fixed by the experimental setup, as it is in the micropipette experiments and our experiments. Depending on the history of the tether's formation, the retraction of the tether will be different. The relationship between tether length and retraction time is related to the physical properties of the membrane from which the tether is formed, as well as the tether's history. In this section I will present Evans and Yeung's as well as Rossier's models of the dynamics of pulling tethers. The details of Rossier's model's predictions for tether retraction will be presented in the following section.

The dynamics of tether pulling that Evans and Yeung derived is based on the idea that there exists a drag when the two monolayers in a lipid bilayer move past each other. Figure 3.1 shows a schematic of the lipid bilayer as a tether is pulled from a point along the bilayer. In general, this drag will contribute very little to the total energy of the membrane. However, when the shape changes rapidly, as when a thin tube is pulled from a giant vesicle, there will be added energy dissipation due to this inter-monolayer drag. The elastic energy for a bilayer can be modeled by adding two stretch energies to the local term for bending:

$$F = \frac{\kappa}{2}\int dA(c_1 + c_2 + c_0)^2 + \sigma A + \frac{\bar{\kappa}_c}{2}(\Delta A/D - \Delta A_0/D)^2 \qquad 3.6$$

This is the same energy functional as the ADE model, with $\bar{\kappa_c} = \bar{\kappa}\pi/A$ and the surface tension and area constraint term explicitly included.

When the two monolayers move past each other, there will be a change in the differential dilation between the monolayers, α. This can be expressed in a

conservation equation describing the dynamic evolution of the differential density field, with an apparent diffusivity D_{diff} that represents the viscous drag at the inter-monolayer region. Multiplying by appropriate factors (see Evans and Yeung for details), one can then obtain the time-dependent behavior of the force between monolayers, M .

$$\frac{dM}{dt} = D_{diff} \nabla_s^2 M + 2\bar{\kappa}_c \frac{d\bar{c}}{dt} - M / t_p \qquad 3.7$$

Here, $\bar{c}$ is the curvature tensor, $\bar{c} = c_1 \hat{n}_1 + c_2 \hat{n}_2$, and $1/t_p$ is the rate of flip-flop, or exchange of lipid molecules from one monolayer to the other. The tension coupling between the monolayers due to the difference in area is defined as:

$$M = \bar{\kappa}_c (\Delta A / D - \Delta A_0 / D) \qquad 3.8$$

Neglecting conventional hydrodynamics, such as Stoke's drag on the tube as it is pulled through the aqueous fluid, one can then use a reduced equation for the conservation equation for interlayer coupling to obtain the forces applied to the tether:

$$\frac{dM}{dt} \approx D_{diff} \nabla_s^2 M \qquad 3.9$$

and

$$D_{diff} \frac{\partial M}{\partial s} = 2\bar{\kappa}_c \dot{L} \qquad 3.10$$

measured at the point of formation of the tether, evaluated at the radius of the tether.

This reduced equation is functionally the same as that of temperature diffusion along the surface of a sphere with a heat source at one of the poles

(see Evans and Yeung). The force coupling will have two contributions, one proportional to tether length and one proportional to extrusion speed:

$$M \approx b D^2 \ln(R/r)\dot{L} + \bar{\kappa_c} L/(2\mathrm{R}^2) \qquad 3.11$$

where b is the inter-monolayer viscous drag coefficient, R the size (radius) of the vesicle or lipid reservoir, r the radius of the cylindrical tether, L the length of the tether, and $\dot{L}$ the speed of extrusion.

The total force on the tether will then consist of three terms: a threshold force due solely to the mechanical properties of the bilayer present before the extrusion of a tether, a velocity-dependent term driven by the viscous drag between the monolayers and a length-dependent, area-difference-elasticity term: $f \approx 2\pi(r\sigma + \kappa/r + M)$, or

$$f \approx 4\pi\sqrt{(\kappa\sigma)} + 2\pi\left(b D^2 \ln(R/r)\dot{L} + \frac{\bar{\kappa_c}}{2\mathrm{R}^2} L\right) \qquad 3.12$$

Figure 3.2 shows the force measured on the tether as it is being pulled at a constant speed, labeling the three contributions. Three regimes exist:

1) A large jump in force on tether as stage (and GUV) accelerates.
2) Stage and GUV move at a constant speed. The force continues to increase due to non-local bending elasticity, arising from the fact that the outer monolayer experiences a more abrupt shape change.
3) Deceleration of stage (and GUV). The slight decrease in total force is due to vesicle and tether relaxation. The difference between the final force and the maximum force is called the dynamic force by Evans and Yeung, and is due to inter-monolayer friction.

The final force that is left after relaxation of the two monolayers is the same as the critical force from the stability analysis (section 3.1.1).

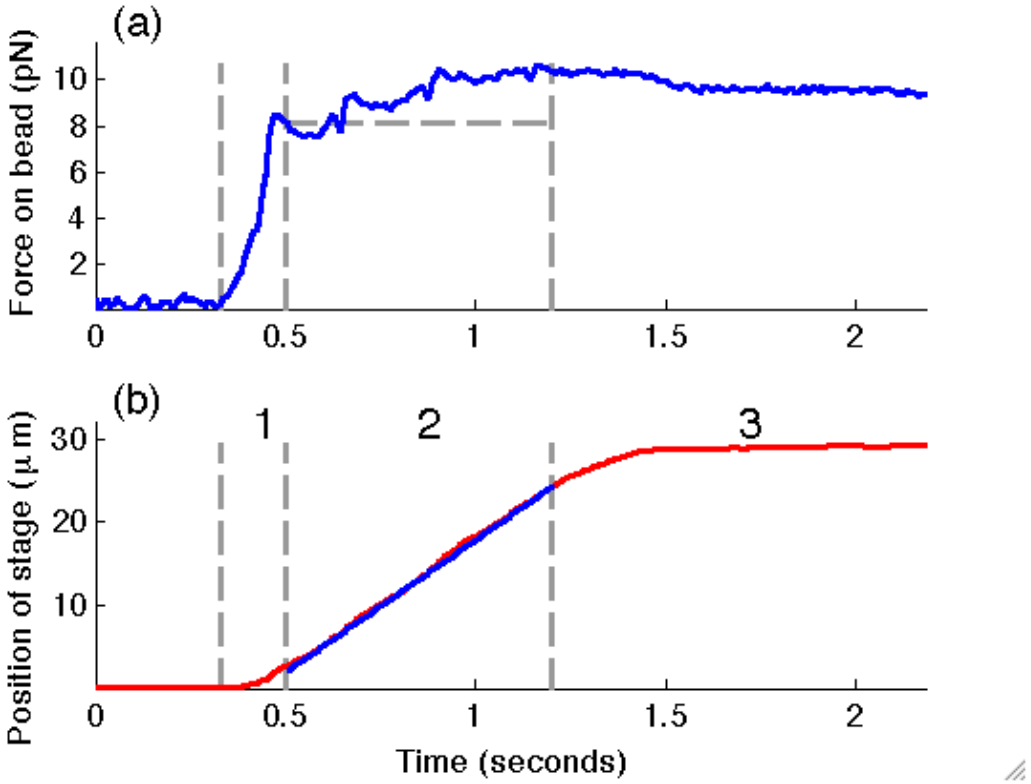

Figure 3.2: (a) Force for forming tether from vesicle as a function of time; label regimes. (b) Position of stage while tether is pulled as a function of time.

Rossier *et al* also derived the force required to pull a tether using another approach. Unlike the work by Evans and Yeung, which places great emphasis on the inter-monolayer drag as the tube is pulled, but ignores conventional hydrodynamic forces like Stokes drag on the tube, the work by Rossier *et al* neglects inter-monolayer effects but takes into account hydrodynamic forces due to pulling a tube inside a fluid. Next, we present a summary of this approach and the predictions derived from it.

The energy of a stable cylindrical tube can be written as the sum of the

contribution from the curvature and the contribution from the surface tension:

$$\frac{F}{2\pi} = \frac{1}{2}\frac{\kappa}{r^2} rL + \sigma rL \qquad 3.13$$

Note that this model neglects the effect of having a membrane formed out of two monolayers, which is why the ADE and the inter-monolayer drag terms are not included. The longitudinal force associated with this energy can be calculated as the derivative of the energy, F, with respect to the tube length. Assuming the volume of the cylinder, $\pi r^2 L$, is conserved, the equation for force becomes:

$$\frac{f}{2\pi} = \frac{3}{4}\frac{\kappa}{r} + \frac{1}{2}\sigma r \qquad 3.14$$

The pressure inside the tube can be derived from the same energy, by differentiating with respect to r to find the pressure force in the radial direction, and then dividing by the surface of the tube:

$$p = [2\pi\sigma L - \frac{\pi\kappa L}{r^2}]/[2\pi r L] \qquad 3.15$$

$$p = \frac{\sigma}{r} - \frac{1}{2}\frac{\kappa}{r^3} \qquad 3.16$$

For the analysis of pulling tethers, one can assume that this pressure is zero, that is, that the system is in quasistatic equilibrium. This leads to a relationship between the surface tension, the bending rigidity and the radius:

$$\sigma r = \frac{\kappa}{2\mathrm{r}} \qquad 3.17$$

The longitudinal force then becomes: $f = 2\pi\kappa / r$. Note that this equation has the same functional form as the critical force required for maintaining stable

tubes under lateral tension as described in section 3.1.1. The main difference, however, is that the radius is not assumed to be constant. Assuming, furthermore, that the flow of lipids is conserved while the tether is pulled, $U(x)r(x)=Ur_m$, where x is the distance from the base of the tether, U is the speed at which the bead is being pulled and r_m is the radius of the tether at the point where the tether unites with the bead, one can construct the balance of forces on a small segment of tether as it is being pulled (see figure 3.1):

$$f(x+dx)=f(x)+\zeta_p U(x)dx \qquad 3.18$$

ζ_p is the friction coefficient per unit length of a cylinder in a laminar flow parallel to the symmetry axis of the cylinder, and is given by $\zeta_p=4\pi\eta/(\ln(L/r)-1/2)$, where η is the viscosity of the fluid.

Combining the balance of forces with the expression of longitudinal force and taking a continuous limit, one can obtain the following relation:

$$-2\pi\frac{\kappa}{r^2}\frac{dr}{dx}=\zeta_p U\frac{r_m}{r} \qquad 3.19$$

The integral of this equation with the boundary condition that $r(0)=r_c$ gives:

$$\ln(\frac{r}{r_c})=\frac{-d\eta U}{\kappa}r_m x \qquad 3.20$$

or, defining a characteristic length as $l^2=\kappa/d\eta U$, this equation can be rewritten as:

$$\ln(\frac{r}{r_c})=-x r_m/l^2 \qquad 3.21$$

d is a numerical coefficient including hydrodynamic interactions, and it is

approximately $2/\ln(L/r_c)$. The profile of the radius of the tether is then:

$$r = r_c \, e^{-x r_m / l^2} \qquad 3.22$$

and the force along the tube is:

$$f = f_c \, e^{+x r_m / l^2} \qquad 3.23$$

with $f_c = 2\pi\kappa / r_c$, as before.

In our experimental setup, the surface tension of the vesicle is not determined by a micropipette, though it cannot be assumed to be zero. As explained in section 2.2, the vesicles are filled with sucrose and then placed inside a lower density solution. Prior to imaging them they sink to the bottom of the sample chamber and attach non-specifically to the cover slip. This will set a surface tension, though it will be unknown to the experimenter. However, the theoretical framework for tether pulling and retraction based on micropipette experiments also applies to our experimental setup.

3.1.3 Tether retraction

Once a tube is pulled, and the longitudinal force is removed, the tube will shrink from the free end, where the bead is attached. Neglecting memory forces, the drag force of the bead will be equal to the force along the tube.

$$f(L(t)) = -6\pi\eta R_b \frac{dL}{dt} \qquad 3.24$$

For a retraction at constant speed, the force on the tube will be approximately equal to the critical force, $f(x = L(t))/2\pi = \kappa / r$. Note that the subsequent equation of the tether length as a function of time,

$L(t)=(2\pi\kappa)/(6\pi\eta R_b r)*t$ still has two unknown quantities: the bending rigidity, κ, and the tether radius, r. The speed of the retracting bead can then be used to calculate the ratio between these two parameters.

$$\frac{dL}{dt}=\frac{\kappa}{r}\frac{1}{3\eta R_b} \tag{3.25}$$

or

$$L-L_0=\frac{\kappa}{r}\frac{1}{3\eta R_b}t \tag{3.26}$$

Figure 3.3 shows how by plotting the bead's position as a function of time, and obtaining the slope, one can estimate κ/r for a given vesicle.

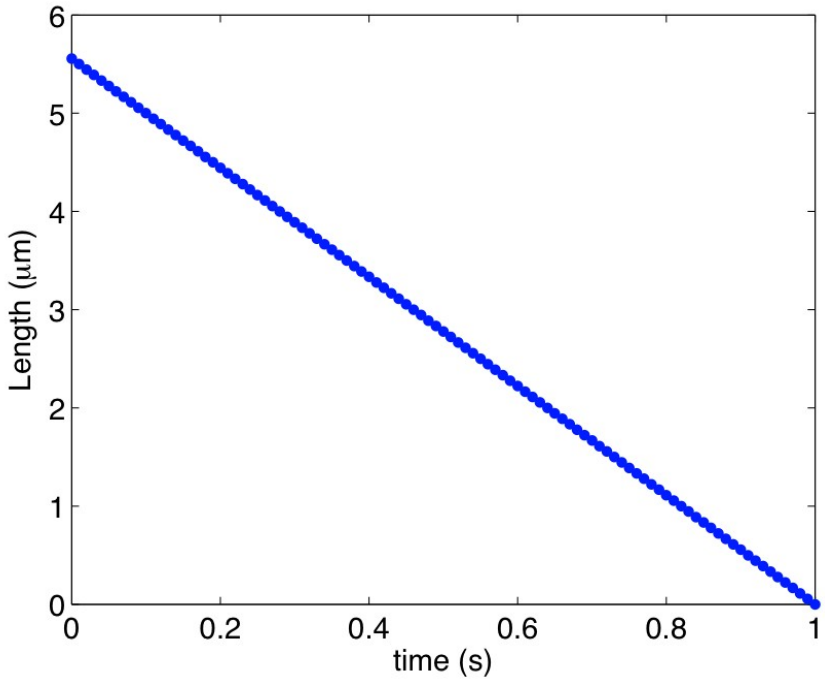

Figure 3.3 Length of tether as a function of time for the case with constant retraction speed. This plot was generated with the equation for a straight line: $L=at+b$. The slope of the plot multiplied by $3\eta R_b$ = 1.8 x 10^{-7} $J/\mu m$ gives the ratio of κ/r.

In the case of non-constant speed, the drag on the retracting bead will be equal to the force along the tube:

$$f_c e^{+L r_m / l^2} = 6\pi\eta R_b \frac{dL}{dt} \qquad 3.27$$

Integration of this equation leads to:

$$e^{L r_m / l^2} = \frac{d}{3}\frac{U}{R_b}\frac{r_m}{r_c} t + e^{L_0 r_m / l^2} \qquad 3.28$$

or,

$$e^{L r_m / l^2} = \frac{d}{3}\frac{U}{R_b}\frac{r_m}{r_c} t + \frac{r_m}{r_c} \qquad 3.29$$

since $r(L = L_0) = r_m = r_c e^{-L_0 r_m / l^2}$.

The shape of tube length as a function of time is of the form $L = -\alpha \ln(\beta t + \gamma)$, where $\alpha = l^2 / r_m$, $\beta = d\,U\,r_m / (3\,R_b r_c)$, and $\gamma = r_m / r_c$. Even though the equation for L has three parameters, only two of them are independent, since β can be expressed in terms of γ , and the other variables can be measured or estimated from the experiment. The variable l^2 contains within it information about the bending rigidity and the radius of the tether at the end attached to the bead, which allows one to rewrite the parameter α as $\alpha = \kappa / (\eta\, d\, U\, r_m)$. Fitting the retraction of the bead to this form of L and obtaining the three fit parameters, one can obtain the value of κ / r_m . Figure 3.4 shows the functional form of L as a function of time with reasonable estimates for the physical quantities.

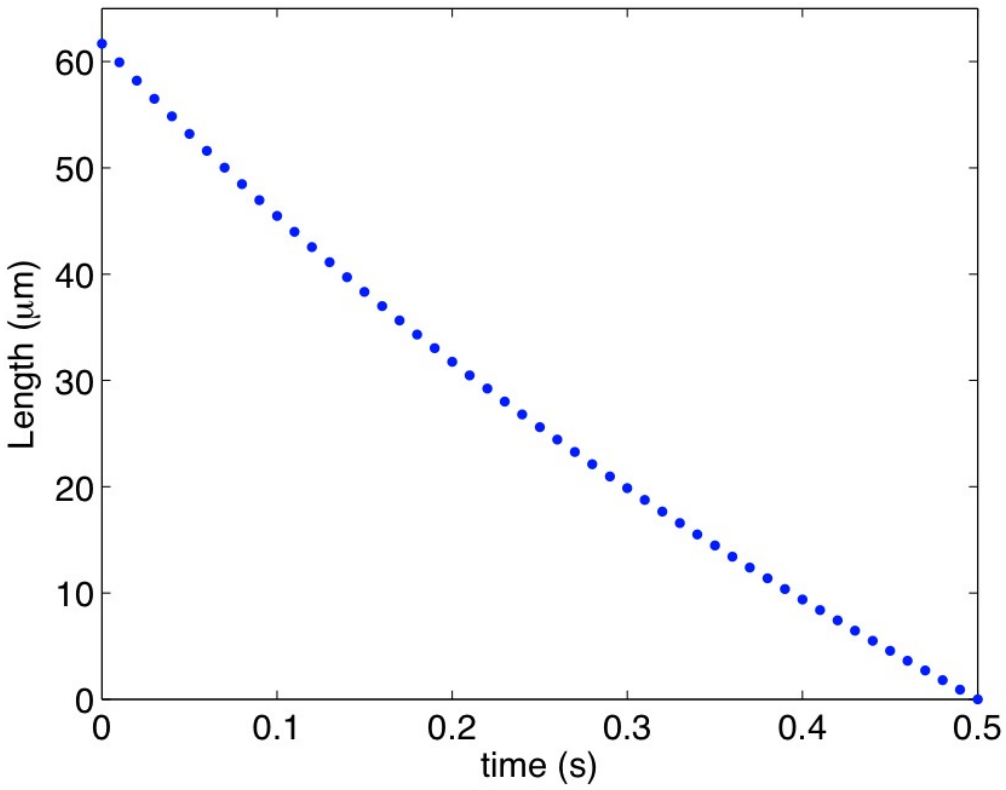

Figure 3.4 Length of tether as a function of time for the case with non-constant retraction speed. This plot was generated using the equation: $L=-aln(bt+c)$, for $a=89, b=1, c=0.32$.

3.2 Experimental Methods

3.2.1 Making GUV

GUV were prepared following the electroformation technique explained in section 2.2.1.

3.2.2 Sample preparation and setup

Viewing chambers were constructed as explained in section 2.2.2. When

preparing the sample, first, 2 to 5 μL of GUV were placed on the cover slip in three droplets. Then, 100 μL of a suspension of silica beads (5 μm in diameter, streptavidin-coated, Bangs Labs), and peptide (Myristoylated N-terminus of Arf1, Anaspec) in PBS (8 g/L NaCl, 0.2 g/L KCl, 1.44 g/L Na_2HPO_4, 0.24 g/L KH_2PO_4) was added while the sample chamber was on the microscope.

Samples were viewed under a Nikon inverted microscope with a 60x magnification, 1.40 NA, oil immersion lens. Images were taken with a Photron Fastcam at 60 or 125 frames per second, or with a Foculus IEEE1394 camera at 15 frames per second. A single optical trap was formed using a BioArryx system, with a 532 nm laser operating at 2.0 W of power, and was controlled using Arryx software. The stage (Proscan Model CS152EF, Prior Scientific Instruments) was moved manually at a reasonably constant speed. The contour of the bead was found using a modified Snake Demo program for Matlab (interface by Dejan Tomazevic, Snake functions by Chenyang Xu and Jerry L. Prince), as explained in section 2.2.3.

When in PBS buffer, 5- μm silica beads will sink to the bottom of the sample chamber. The force on our optical traps is not strong enough to lift the settled beads. Also, adding the beads, peptide and buffer when the sample is on the microscope minimizes flows to which GUV are subjected, minimizing deformations and ruptures. A single bead was trapped in an optical trap as it fell towards the bottom. The stage was then moved around and the bead was pushed against several GUV until it remained attached to one. In order to test if

the bead and the GUV were attached to each other, the stage was moved slowly so that the bead and GUV were separated, and then the optical trap was turned off, by closing a shutter on the laser path. If the bead moved toward the GUV, then they were likely attached, and the experiment could proceed. If, on the other hand, the bead sunk to the bottom of the sample chamber, the bead and GUV were not attached, and the sample had to be replaced.

In order to pull tethers from GUV, the bead was held in place by the optical trap while the stage was moved at constant speed so that the GUV moved away from the bead. This formed a tether, which cannot be seen on the microscope, even though its 'shadow' can be observed in enhanced images. The optical trap was turned off, by closing a shutter in the path of the laser which released the bead and allowed it to retract back into the GUV.

3.2.3 Measuring forces with a single optical trap

Optical traps are formed by focusing a laser beam with a large numerical aperture objective. A streptavidin-coated silica bead trapped in an optical trap can be attached to a GUV with a few Biotinilated lipids. The force required to keep the bead in the optical trap can then be monitored as a tether is pulled, by moving a GUV away from the bead. This section describes the principles of optical trapping, trap force calibration, and how this technology is used to monitor the force required to deform a lipid bilayer into a long, thin tube.

A dielectric object close to the focus of a laser beam will be subjected to optical forces that will keep the object confined to the center of the beam due to

momentum transfer between the photons and the dielectric object. The resulting optical force can be separated into two components: a scattering force and a gradient force. The scattering force is caused by forward momentum being transferred by the incoming photons to the dielectric object due to scattering or absorption. The net result of these interactions is that the dielectric object will feel a force in the forward direction. The gradient force is formed by a steep intensity gradient, like that present close to the focus of a laser beam. In an optical trap, the inhomogeneous electric field of a tightly focused laser will induce fluctuating dipoles on the dielectric object and each dipole will feel a force in the direction of the intensity gradient, which in turn causes the dielectric object to experience a force towards the focal point of the beam.

In order for an optical trap to be stable, the gradient force pulling the dielectric object towards the center of the focal region must exceed the scattering force pushing the object away. This condition can be met with a very steep intensity gradient, formed by focusing the laser beam through a high numerical aperture objective. The optical trap will then act as a Hookean spring with a characteristic stiffness proportional to the light intensity. Figure 3.5 presents a cartoon depiction of the force experienced by a bead near the focal point of an optical trap.

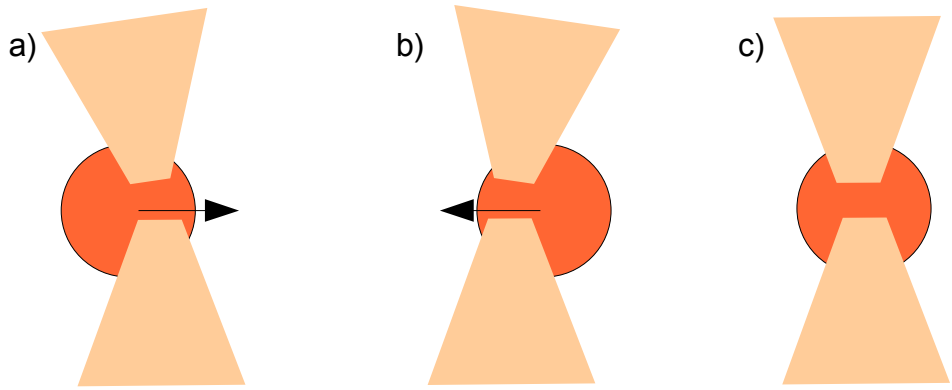

Figure3.5: A bead slightly off the axis of a focused beam will feel a restoring force. a) Bead to the left of beam axis feels a force to the right. b) Bead to the right of beam axis feels a force to the left. c) Bead in the center of beam axis fells no force (left or right).

Quantitative optical trapping requires accurate position calibration. The determination of the displacement of the dielectric object from its equilibrium position is key to determining the applied force, calculated as $F = -\kappa_{trap} x$, where F is the force, κ_{trap} is the optical trap stiffness, and x is the displacement from the equilibrium position. The position of the center of a bead in the optical trap was determined by digitally processing images acquired by a camera. In our experiments, the edge of the bead is found using a modified code for the snake algorithm, described in detail in Section 2.2.3, and the centroid of the bead was calculated as the average x-position and y-position of the edge points. Section 3.2.4 presents the calibration of the optical traps used in the experiments, while Section 3.2.5 presents an estimate of the accuracy of determining the position of the bead's center.

The thermal fluctuations of a trapped object can be used to obtain the trap stiffness. For an object in a harmonic potential, the Equipartition Theorem leads

to the following relation:

$$\frac{1}{2} k_B T = \frac{1}{2} \kappa_{trap} \langle x^2 \rangle \qquad 3.30$$

where k_B is Boltzmann's constant, T is the absolute temperature, κ_{trap} is the trap stiffness, and $\langle x^2 \rangle$ is the variance of the displacement of the trapped object from the equilibrium position. Measuring the variance of the position of a trapped object, one can then calculate the trap stiffness. An advantage of this method is that it does not depend explicitly on the viscous drag of the trapped particle, so the viscosity of the medium and the precise shape and size of the particle are not needed for the calibrations. A drawback of this method is that it depends on measuring a variance, which is intrinsically biased: any added noise in the position measurement will lead to an under-estimation of the trap stiffness, while any low-pass filtering of the position signal will result in an over-estimation of the trap stiffness (Neuman and Block, 2004).

Applying and measuring point forces on a GUV can be achieved by attaching a streptavidin-coated bead to a GUV made with 1% Biotinilated lipids, and imaging the bead's movement in the trap. The bead's motion will be a reflection of the bilayer's motion at the attachment point, since the bead and the membrane are attached over a small area. The bead and membrane are held together by a few biotin-avidin bonds, which are among the strongest non-covalent bonds known (Willemsen *et al*, 2000). Holding a bead attached to a GUV via biotin-avidin bonds in an optical trap, one can measure the forces needed to deform the bilayer by measuring the force on the bead.

3.2.3 Force calibration

Formation of a single optical trap was done using a commercial system by Arryx Incorporated. It is a complete optical trapping workstation with a 2W diode pumped solid-state laser (λ = 532 nm), a spatial light modulator for holographic beam shaping, an inverted microscope, and computer control. The working distance of a high numerical aperture oil immersion objective is around 20 μm from the coverslip, since high numerical aperture objectives have an already short working distance that is reduced even further by spherical aberrations caused by the large difference in refractive index between the immersion oil and the aqueous environment of the sample (Hell *et al*, 1993).

In order to measure the force on the silica bead as the tether was being formed, the optical trap had to be calibrated for the bead size, the position of the trap, and the laser power. To ensure that the same calibration applied to separate measurements, the trap position was saved using the Arryx software. Several thousand images of a 5- μm -diameter silica bead thermally fluctuating in a single trap were taken. The outline and center of the bead were obtained using a snake algorithm, and histograms of the bead's position in the horizontal and vertical directions were plotted. As figure 3.8 shows, this histogram can be fit to a Gaussian function. The equation that was fit to the histogram shape is the non-normalized Gaussian function: $f(x|\sigma,\mu)=A\,\mathrm{e}^{-(x-\mu)^2/2\sigma^2}$, where σ is the standard deviation and μ is the mean. From the fit parameters, one can obtain

the variance of the bead's position, which is related to the trap stiffness. During these experiments, three different trap positions, with their respective trap stiffness, were used. The values obtained for the calibrations of these traps are presented in tables 3.1 and 3.2.

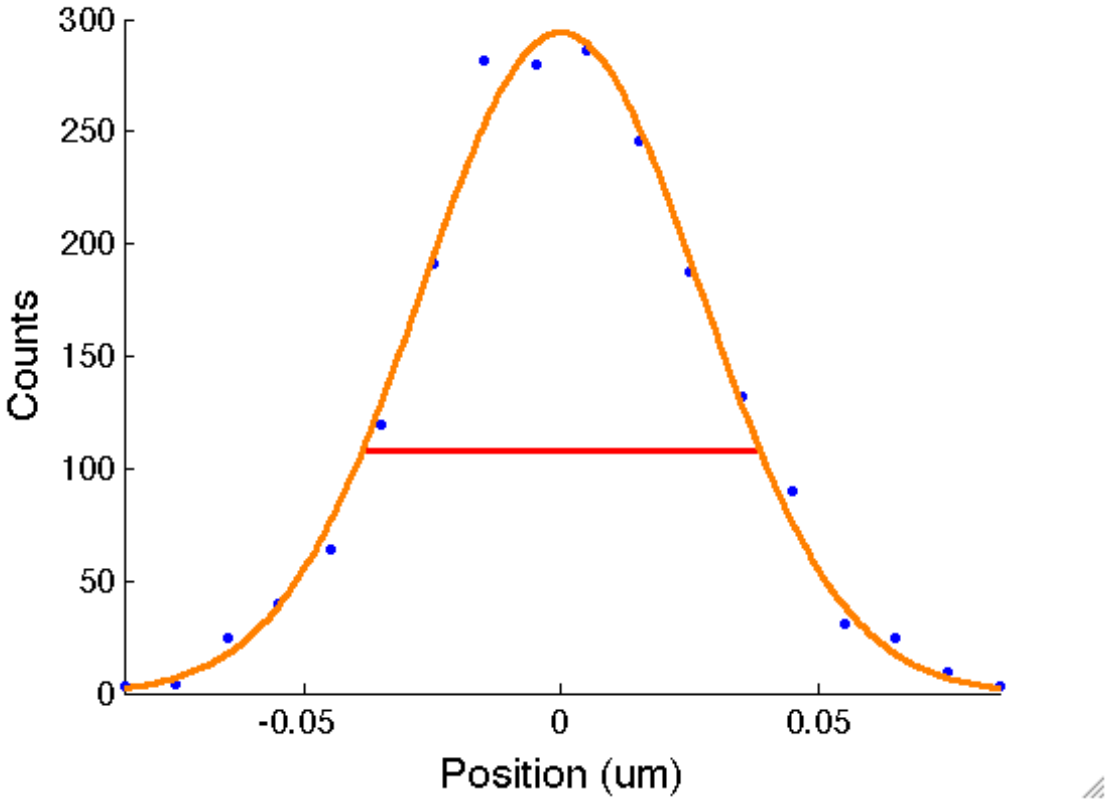

Figure 3.6: Sample histogram of the x-position of an optically-trapped bead. Blue dots represent data, the orange line represents the best fit, and the red line represents the variance.

Trap Name	μ (μm)	σ (μm)	$k_B T$ (pN. μm)	κ_{trap} (pN/ μm)
102109up	5.19	0.42 x 10^{-3}	4.07 x 10^{-3}	9.69
102109down	5.28	0.74 x 10^{-3}	4.07 x 10^{-3}	5.50
111009	5.52	0.36 x 10^{-3}	4.07 x 10^{-3}	11.3

Table 3.1 Fit parameters and trap stiffness for the calibration of optical traps in the x-direction.

Trap Name	μ (μm)	σ (μm)	$k_B T$ (pN. μm)	κ_{trap} (pN/ μm)
102109up	4.64	0.42 x 10^{-3}	4.07 x 10^{-3}	9.69
102109down	4.38	0.55 x 10^{-3}	4.07 x 10^{-3}	7.40
111009	5.30	0.42 x 10^{-3}	4.07 x 10^{-3}	9.69

Table 3.2 Fit parameters and trap stiffness for the calibration of optical traps in the y-direction.

3.2.4 Accuracy in center of bead calculation

In order to find the accuracy of the method we used to determine the center of a trapped bead, we measured the center of a bead that was stuck to the glass surface and thus, not fluctuating. As can be seen from the Gaussian fit of the histogram of the center's position (figure 3.7), we can determine the center of the bead to an accuracy of 8 nm.

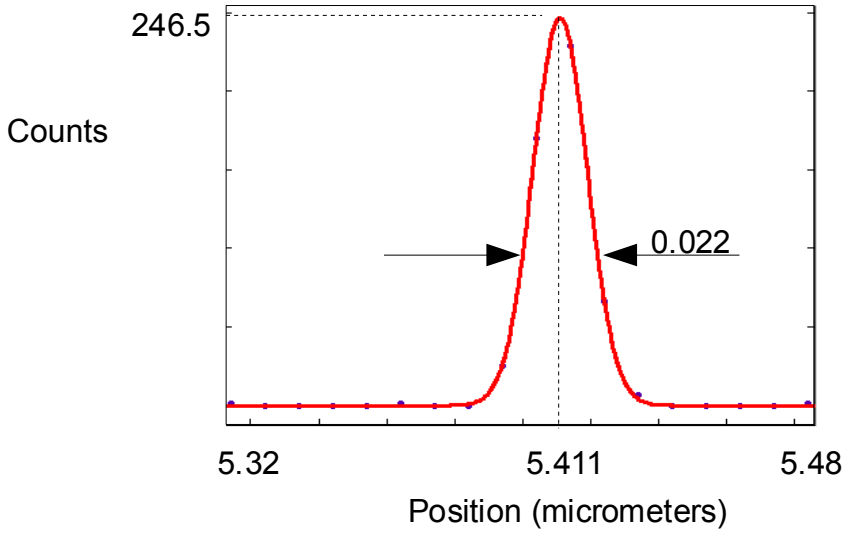

Figure 3.7: The center of a 5-μ silica bead can be determined to within 8 nm. Purple dots represent data and the red line represents the best fit to a Gaussian function. The average x-position of the bead is 5.411 , and the variance of the x-position is 0.011.

3.3 Results

3.3.1 GUV display wide inter-batch variations

We measured the force on beads as tethers were being pulled from GUV. The shape of the force plot as a function of time is the same as that predicted by Evans and Yeung's theory. Both the average non-local force and the average final critical force for tethers pulled from GUV in the absence of peptide were within the same range from batch to batch, though with a wide variability within the same batch.

Figure 3.8 shows the force on the bead as the tether is being pulled. The increase in force during the second regime, in which the stage is moving at a constant speed, is the non-local force, shown on the graph. We measured the non-local force this way for GUV from different samples in the absence of peptide. The results are shown in table 3.3.

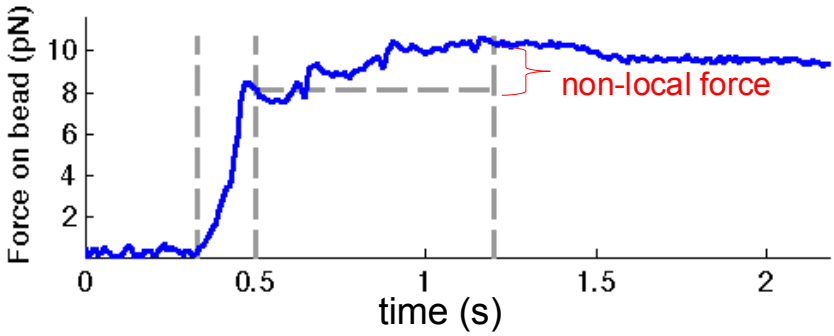

Figure 3.8: Force on bead a tether is pulled as a function of time. The vertical gray lines show the limits of the three regimes, as explained in section 3.1.2. The increase in force during the second regime, as the stage is moved at a constant speed, is equal to the non-local force due to area difference elasticity.

Sample date	Peptide concentration (uM)	Non-local force (pN)
102709	0	3.23
110309	0	3.05
110309	0	2.54
110309	0	6.11
110309	0	10.46
112309	0	10.93
120209	0	4.95

Table 3.3 Non-local force measured for GUV from different samples in the absence of peptide.

The average non-local force for tethers pulled from GUV in the absence of peptide is 6.16 ± 3.33 pN. The two cases where the force is greater than 10 pN (samples 110309 and 112309) correspond to tether extrusion speeds of around 30 $\mu m/s$. There is a third instance in which the extrusion speed is around 30 $\mu m/s$, the first sample from 110309, but in that case the non-local force is only around 3 pN. The large variation in the measurements of non-local force with this technique even for GUV alone make changes caused by external agents or changing environmental conditions difficult to detect.

The critical force to maintain a stable tether can be measured once the stage stops. We measured the critical force for tethers pulled from GUV from different samples in the absence of peptide. The results of these measurements are presented in table 3.4.

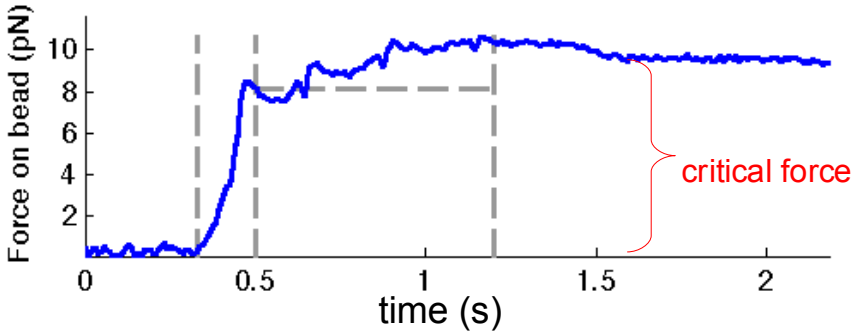

Figure 3.9: Force on bead as tether is being pulled as a function of time. The final force after the stage has stopped moving is the critical force – the force required to maintain a stable tether.

Sample date	Peptide concentration (uM)	Critical force (pN)
102709	0	7.02
110309	0	4.88
110309	0	4.49
110309	0	5.95
110309	0	6.06
112309	0	8.74
120209	0	2.49

Table 3.4 Non-local force measured for GUV from different samples in the absence of peptide.

The average critical force for tethers pulled from GUV in the absence of peptide is 5.9 ± 2.66 pN. As with the non-local force, there is wide variability in the critical force measurements, making changes due to external factors hard to detect.

3.3.2 Myristoylated Arf1 peptide does not change the force required to form a tether from GUV

We measured the non-local force for tethers pulled from GUV in the presence of varying concentrations of peptide. The force on the bead as a

function of time had a similar shape as figure 3.8. The results for the non-local force for tethers pulled from GUV in the presence of varying concentrations of peptide are presented in table 3.5.

Sample date	Peptide concentration (μM)	Non-local force (pN)
102709	0	3.23
110309	0	3.05
110309	0	2.54
110309	0	6.11
110309	0	10.46
112309	0	10.93
120209	0	4.95
102109	0.96	2.18
102109	0.96	2.55
102109	0.96	2.45
120209	2.17	3.73
120209	2.17	3.4
120209	2.17	5.22
111609	2.27	3.65
111609	2.27	5.53

Table 3.5 Non-local force for tethers extruded from GUV in the presence of varying concentrations of peptide.

The average non-local force for tethers pulled from GUV in the absence of peptide is 6.16 ± 3.33 pN, while the average non-local force for all cases in the presence of peptide is 3.92 ± 1.3 pN. These two intervals overlap considerably, and the two groups cannot be said to be different. It may appear that there is a concentration-dependent effect, since the non-local force appears to be higher for peptide concentrations of 2.17-2.27 μM (3.4-5.53 pN) than for peptide concentrations of 0.96 μM (2.18-2.55 pN). However, as can be seen in figure

3.10, all of these non-local force values fall within the limits of the forces measured from GUV in the absence of peptide. Hence, one cannot conclude that addition of peptide changes the non-local force due to area-difference-elasticity for pulling tethers from GUV.

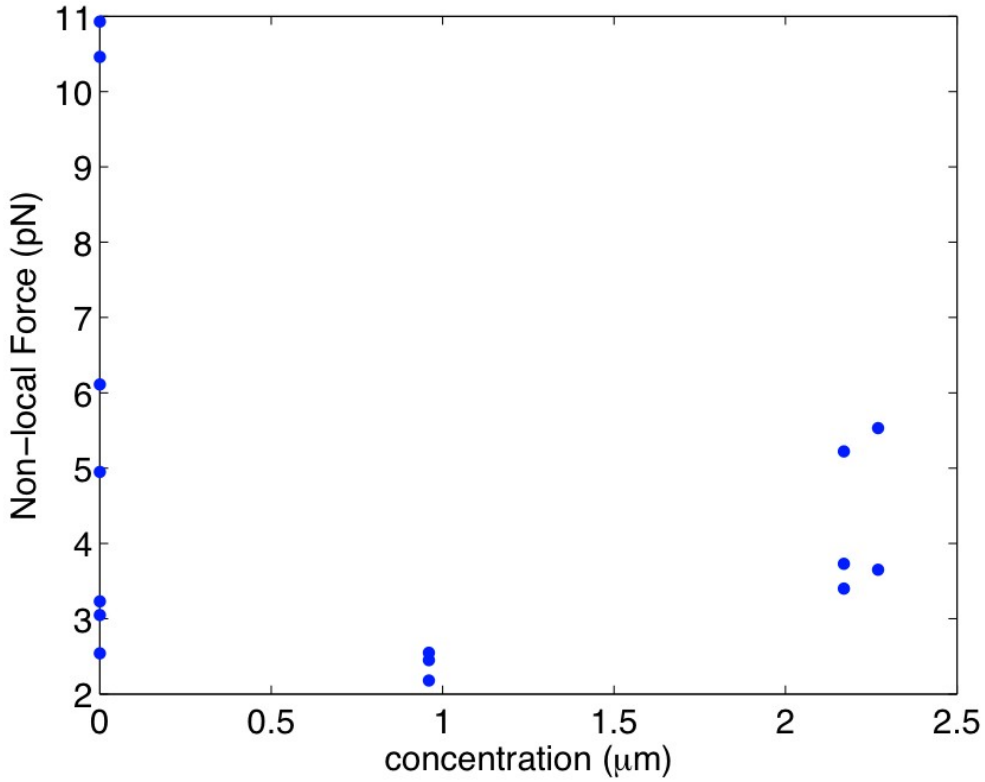

Figure 3.10: Non-local force as a function of peptide concentration. Each point represents one tether pull for a single GUV. Addition of peptide does not change the non-local force on the tether.

We measured the critical force required to maintain a stable tether under tension for GUV in the presence of varying concentrations of peptide, as described above. Figure 3.11 shows the results of measuring these forces for all cases. The large variability in the measurements leads to the conclusion that

changes in critical force caused by the peptide cannot be seen using this technique.

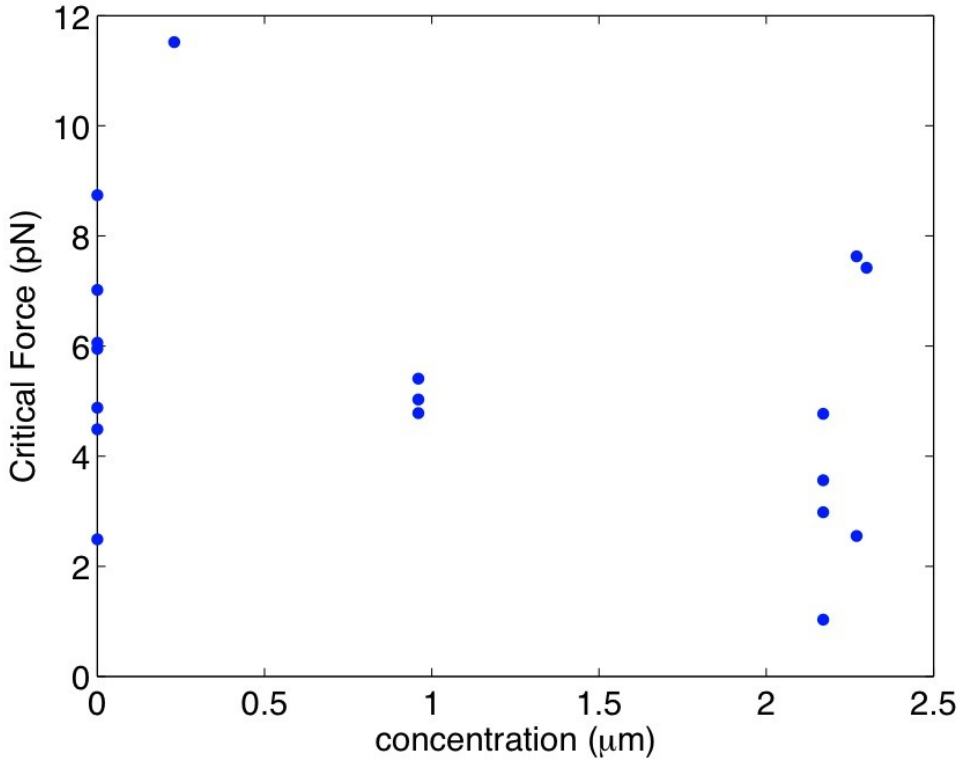

Figure 3.11: Critical force for maintaining a stable tether pulled from GUV in the presence of varying concentrations of peptide. Each point represents one tether pull for a single GUV. Addition of peptide does not change the critical force on the tether.

The initial hypothesis was that addition of peptide would make the membrane easier to bend, and that this change could be seen in a significantly smaller force required to pull a tether. Even though there is wide variation from sample to sample and within samples, we did not observe a large decrease in the critical force required to maintain a stable tethers upon addition of peptide.

3.3.3 Tether retraction is logarithmic in shape for most cases without peptide; linear otherwise

We tracked the motion of the bead attached to the end of the tether as it retracted back into the GUV after the shutter in the path of the laser was closed. The position of the bead from the edge of the GUV, or the length of the tether, as a function of time was fit to either a linear equation or a logarithmic equation. Determination of whether the retraction followed a linear or logarithmic shape was done by comparing the residual for each fit. The retraction was considered either linear or logarithmic if the residual for the fit was considerably larger for one fit or the other. Figure 3.12 shows an example of a case where the retraction was considered to be logarithmic, since the linear fit did not work well, while the logarithmic one did.

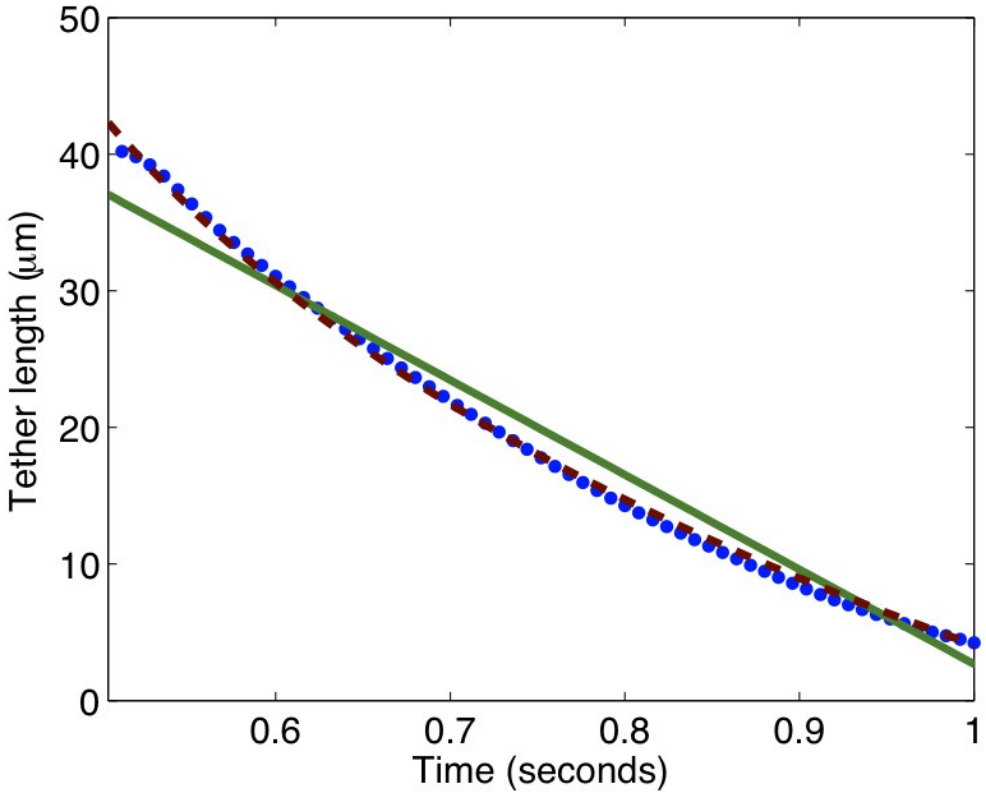

Figure 3.12 Length of retracting tether as a function of time. Blue dots: data points; dashed red line: fit to $L=-a\ln(bt+c)$; continuous green line: fit to $L=at+b$. The logarithmic fit is better than the linear fit, and the retraction was considered to be logarithmic.

If both residuals were close in value, then the retraction was considered to be linear. The linear fit has only two parameters, while the logarithmic fit has three. If both fits were equally good, based on the magnitude of the residual, then the fit with less parameters was chosen. Figure 3.12 shows an example of a case where the retraction was considered to be linear, since both linear and logarithmic fits worked equally well.

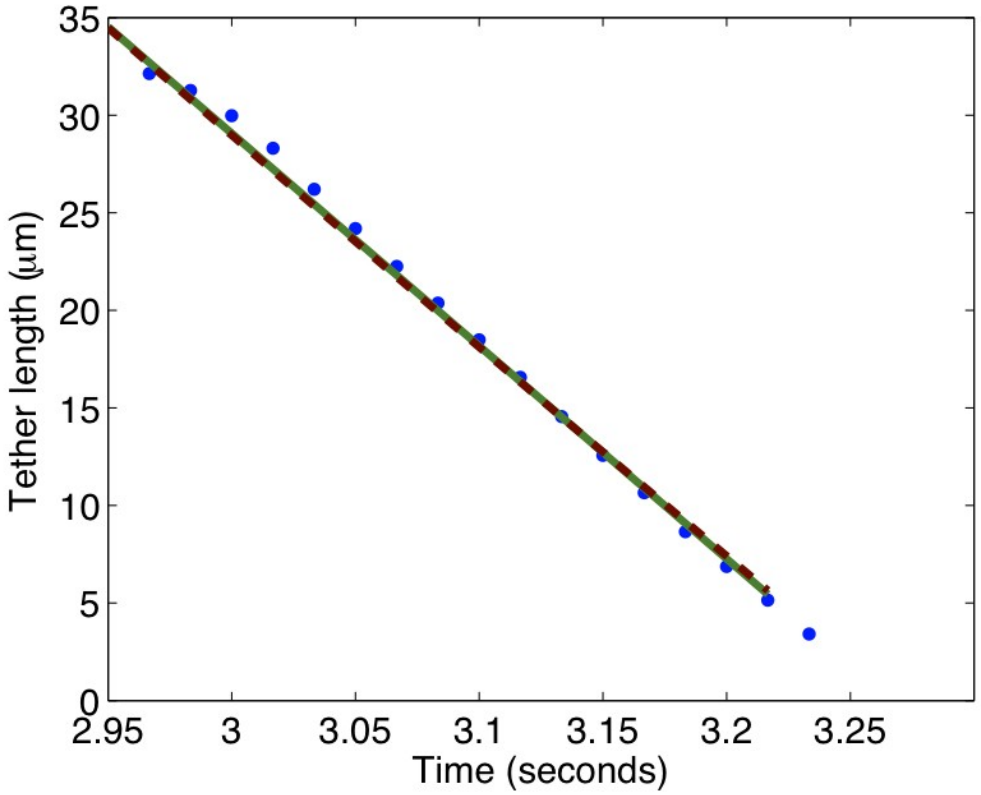

Figure 3.13 Length of retracting tether as a function of time. Blue dots: data points; dashed red line: fit to $L=-a\ln(bt+c)$; continuous green line: fit to $L=at+b$. Both fits were equally good. The retraction was considered to have a linear shape.

Table 3.6 shows the residuals for the linear and logarithmic fits. Residuals are defined as: $res=\sum(data-best\ fit)^2$ and have units of length squared.

Sample date	Peptide concentration	Linear fit residual (μm^2)	Log fit residual (μm^2)	Retraction shape

	(μM)			
102709	0	17.3	11.5	linear
110309	0	201.8	9.56	logarithmic
110309	0	32.4	6.25	logarithmic
110309	0	22.3	15.7	linear
110309	0	88.6	30.6	logarithmic
112309	0	101	61	logarithmic
120209	0	5.39	3.83	linear
10710	0.2	0.74	4.94	logarithmic
10710	0.2	68.5	8.61	logarithmic
102109	0.96	1.38	0.71	linear
102109	0.96	4.9	4.5	linear
120209	2.17	6.08	2.98	linear
120209	2.17	83	54.5	linear
111609	2.27	26	15	linear

Table 3.6 Residuals of linear and logarithmic fits.

Some tethers in GUV in the absence of peptide retracted with a constant speed (3 of 7), while others retracted with a logarithmic length as a function of time (4 of 7). Only two cases of tethers pulled form GUV in the presence of peptide retracted in a logarithmic fashion, while the rest (5 of 7) retracted with constant speed. These logarithmic retractions happened only for the smallest concentration of peptide used, 0.2 μM.

3.3.4 Initial retraction speed does not change upon addition of peptide

The speed of the bead as the tether retracts will be proportional to the drag on the bead due to the medium viscosity. As can be seen in figure 3.14, there is wide variability in the initial retraction speed for the cases without

peptide. Also, there is no drastic change in the initial retraction speed upon addition of peptide. This is consistent with our previous finding, that the force along the tether is not dramatically altered in the presence of the myristoylated N-terminus of Arf1.

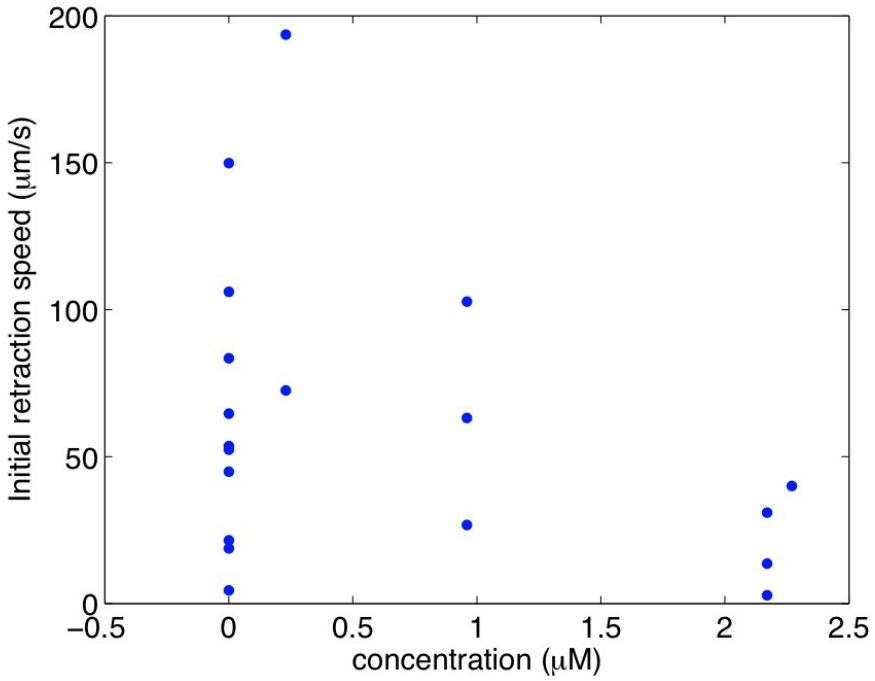

Figure 3.14: Initial tether retraction speed as a function of peptide concentration.

There is no correlation between the initial retraction speed and the functional shape of the retraction curve (linear or logarithmic) for the cases without peptide. That is, the tethers in the absence of peptide that exhibited a linear retraction, had initial retraction speeds between 18 and 106 μm/s. This wide variability makes comparisons between cases with and without peptide

inconclusive.

3.3.5 Addition of peptide makes it more likely that the GUV deforms during tether retraction

In order to further explore the suggestion that addition of high concentrations of peptide makes the tether retract linearly, an indication of constant tether radius according to the theory, we went back and compared the images of GUV and tethers. We found that some GUV were deformed with a bulge at the point where the tether joined the vesicle during retraction, while others were not (figure 3.14). We then compared the shape of the GUV with the shape of the tether length during retraction and found that only GUV where the tether retracted at constant speed presented this bulge.

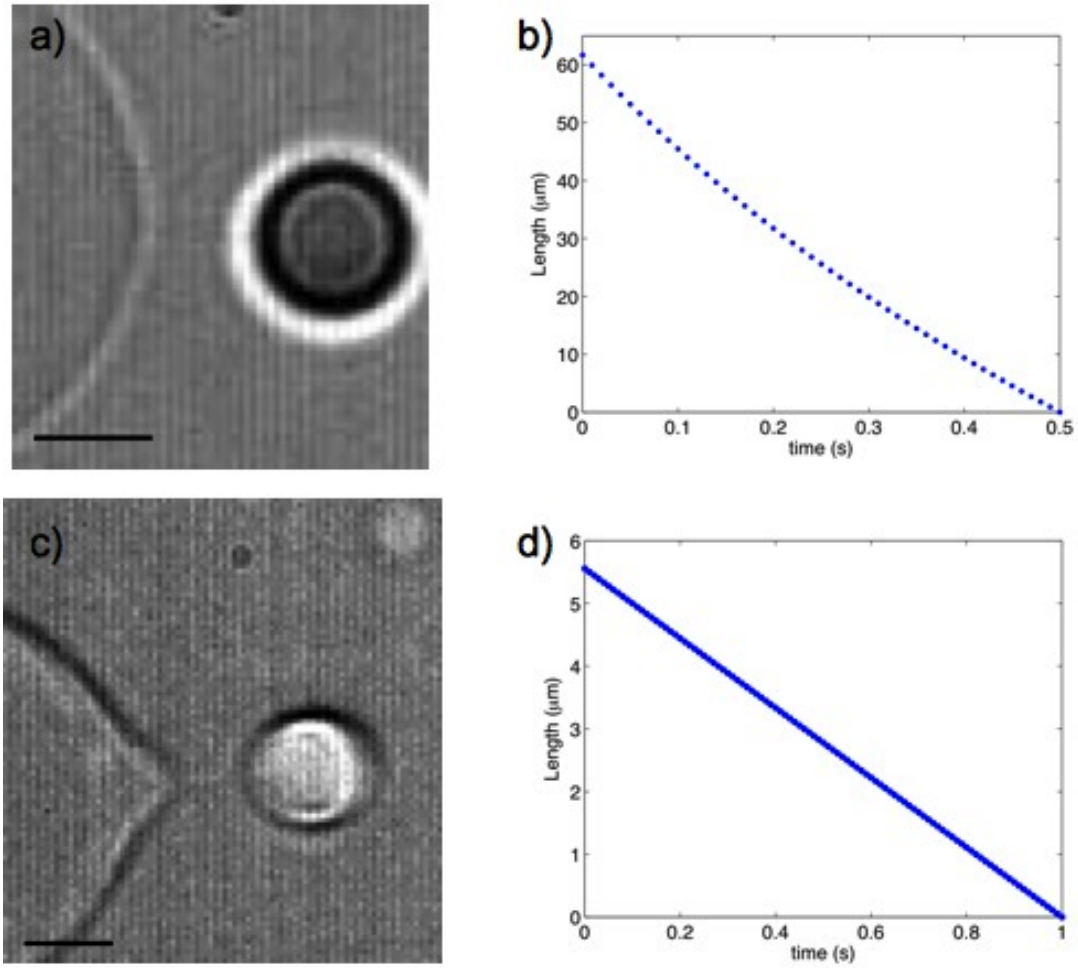

Figure 3.15 a) Image of GUV and bead during tether retraction. b) Sample logarithmic shape of tether length as a function of time. c) Image of deformed GUV and bead during tether retraction in presence of peptide. d) Sample linear retraction of tether. BAR in images represent 5 μm.

As noted in the previous section, all of the tethers from GUV in the presence of peptide in concentrations higher than 0.2 μM retracted with a constant speed. All of the GUV from which these tethers were pulled presented the bulge as shown in figure 3.14. However, some tethers pulled from GUV in the absence of peptide also displayed this behavior. Hence, one cannot definitely conclude that addition of peptide causes this bulge to form, or changes the tether retraction shape from logarithmic to linear. It seems from our experiments that

addition of peptide makes this bulge more likely to appear, though further considerations may be needed (see chapter 5).

3.4 Summary

Pulling tethers from GUV while holding a bead attached to the tether in an optical trap provides a way to directly measure the forces required to bend the membrane. The force on the bead as the tether was pulled had the shape and regimes predicted in Evans and Yeung's theory, both for tethers pulled from GUV in the absence and in the presence of peptide. However, we observed large variations in the critical force required to maintain the tether in place, as well as in the non-local force due to area differences from the monolayers. The range of values of these forces for different concentrations of peptide overlap considerably. Hence, we cannot conclude whether addition of peptide has an effect on the forces present while forming a tether.

Tether retractions depend on the physical properties of the membrane, as well as on the history of the tether. We found that some tethers retracted with length varying logarithmically in time, while others retracted at a constant speed. Except for the cases with very low concentration of peptide, the tethers formed from GUV in the presence of peptide retracted linearly with time. The GUV from such tethers presented a bulge at the junction between GUV and tether, that was not present with tethers retracting logarithmically. However, this bulge and the linear retraction of the tether were also observed in some cases when no peptide

was added.

Chapter 4: Fluorescence Spectroscopy

One of the measures of lipid bilayer physical properties is the packing of the lipids. Lipid bilayers can be in a “gel-like” state, where lipid molecules are closely packed, or in a “fluid-like” state, where lipid molecules are not closely packed. Lipid packing can be assessed using fluorescence spectroscopy, and has been traditionally been studied as a function of temperature and lipid composition (Wilson-Ashworth *et al*, 2006). Some newer studies measure the effect of membrane-binding peptides on lipid packing (Sanchez-Martin *et al*, 2009). In order to test the hypothesis that addition of peptide affects the packing of the lipid molecules we conducted fluorescence spectroscopy measurements of three fluorescent probes incorporated into Large Unilamelar Vesicles (LUV): Prodan, Diphenylhexatriene (DPH), and Bispyrene, with varying concentration of four test molecules: myristoylated N-terminus of Arf1, non-myristoylated N-terminus of Arf1, the ALPS domain of the yeast protein Kes1p, and myristic acid. Increasing concentration of myristoylated N-terminus of Arf1 increases the 3-wavelength generalized polarization (3wGP) of Prodan, as well as the polarization of DPH embedded in LUV, while the non-myristoylated N-terminus of Arf1, ALPS domain of Kes1p and myristic acid had no effect on the fluorescence properties of either probe. None of the four molecules tested had an effect on the excimer-to-monomer emission intensity ratio of Bispyrene. Only the myristoylated N-terminus of Arf1 had an effect on the probes used, indicating that myristoylation might be important for the effect of Arf1 on lipid membranes, making the membranes more gel-like.

4.1 Introduction

4.1.1 Fluorescence spectroscopy

Luminescence is the emission of photons by molecules transitioning from a high-energy state to a low energy one. Two possible luminescence pathways exist, depending on the coupling between the electron in the high-energy state and one in the lower-energy state. When the two electrons have opposite spin, the decay of the higher-energy electron in a singlet state will not require a spin change. This transition, known as fluorescence, happens with a lifetime of about 10 ns. When the two electrons have the same spin, decay from the high-energy state will require a spin change. This decay from a triplet state is known as phosphorescence and happens with lifetimes of ms to a few seconds.

Fluorescent data are usually presented as emission intensity plotted as a function of wavelength. Fluorescence emission is shifted to lower energies than the excitation light, due to rapid relaxation to lower-energy vibrational modes, called Stoke's shift. Both excited and ground states have these modes, and the relaxation can take place before the emission of a photon, or after. Further shifts due to solvent effects are also possible (Laskowicz, 1983).

Fluorescence spectroscopy is sensitive to processes occurring up to 100 Å away from the fluorescent molecule, as long as the process occurs during the lifetime of the excited state. This time span between absorption and emission allows for several processes to affect the excited fluorescence molecule, or

fluorophore, such as collisions, rotational and translational diffusion, formation of complexes and changes in the environment surrounding the fluorophore. All these processes affect the fluorescence properties, like polarization and emission spectra, of the fluorophore sample.

4.1.2 Fluorescence Polarization

The theory of fluorescence polarization is based on considering the fluorophore as an oscillating dipole. Though fluorophores emit single photons, the spatial distribution of the energy emitted can be calculated using classical (non-quantum) electricity and magnetism theory. A planar fluorophore aligned along the z-direction is just like an antenna, and will emit electromagnetic waves equally in the x-y directions, but not in the z-direction. The absorption and emission of dipoles need not be perfectly aligned in the z-direction (the direction of the electric field vector of the incident light) in order to absorb or emit. The probability of absorption or emission will be proportional to $\cos 2\theta$ where θ is the angle between the molecule's absorption or emission dipole and the z-direction. Hence, excitation and emission can happen in a symmetrically distributed volume around the z-axis (Laskovicz, 1983).

In a fluorescence polarization experiment, the sample is illuminated with vertically polarized light, and the intensity of the emitted light is measured after passing through a polarizer. The intensity measured with the exit polarizer placed parallel to the direction of the incident light is I_v , while the intensity measured

with the exit polarizer perpendicular to the direction of the incident light is I_h . The polarization can then be calculated using the following formula: $P=(I_v-I_h)/(I_v+I_h)$. For completely vertically polarized light, P = 1, whereas for unpolarized light P = 0.

If the solution is isotropic, the fluorescent molecules will be oriented randomly. When the sample is illuminated with polarized light, only those molecules whose absorption transition dipole is within the volume around the axis of the electric field vector direction will be excited. This photoselection results in a partially polarized fluorescence emission. The maximum polarization possible for a given fluorophore will be determined by the relative angle between the absorption and emission dipole moments.

Several processes can further decrease the emission polarization. The dominant cause of depolarization is rotational diffusion. One can assume that upon a pulsed excitation the polarization decay will be a single exponential, $P(t)=P_0 \mathrm{e}^{-t/\phi}$. The rotational correlation time of the fluorophore, ϕ is dependent on solvent viscosity, temperature, and molecule volume. While this single exponential decay is valid only for spherical molecules, more complex expressions needed for other molecule shapes will also depend on these physical parameters. Fluorescence polarization measurements then reveal the average rotation of the fluorophore, depending on the magnitude of the rotation in the time between absorption and emission, as well as the viscosity of the medium. Hence, a change in medium viscosity will be seen as a change in

fluorescence polarization.

Fluorescence polarization can be used to estimate the microviscosity of biological membranes. The probe selected must partition into the hydrophobic core of the lipid bilayer. DPH is ideal for this application, since it can be excited with a range of wavelengths (from 320 nm to 380 nm), it allows for highly diluted sampling, and the depolarization rotations are isotropic (Laskowicz, 1983).

Earlier experiments compared the anisotropy or polarization for fluorophores embedded in lipid bilayers and that of the fluorophore in a solvent of known viscosity. This comparison allowed one to estimate a 'microviscosity' of the bilayer. However, the behavior of the fluorophore in the isotropic environment of the solvent cannot be compared to the behavior of the fluorophore in the anisotropic environment of the lipid bilayer. Hence, alternative interpretations of the polarization changes of DPH fluorescence, such as lipid packing and gel-like vs liquid-like phase behavior, are used now (Wilson-Ashworth *et al*, 2006).

4.1.3 Effects of Environment on Fluorescence Emission Spectra

The emission spectra of fluorophores will shift to lower energy as a result of interactions of the fluorophores with the surrounding molecules, as long as the relaxation time of the solvent (surrounding molecules) is much smaller than the fluorescence lifetime. The emission will then occur from the relaxed (lower energy) state. The shift in the emission spectra can be a result of general solvent effects or specific effects based on chemical interactions between the

fluorophores and the solvent. For example, the polarity of the solvent will have great impact on the fluorescence emission spectra of the fluorophore (Laskowicz, 1983). The precise changes in emission spectra will depend on the specific characteristics of the fluorophore used.

4.2 Methods

4.2.1 Fluorescence spectrometry and sample preparation

Fluorescence spectrometry measurements were performed in a Perkin Elmer LS55 Luminescence Spectrometer controlled with FLWinLab software. The LS55 Spectrometer has a Xenon lamp, and the emission and detection wavelengths are selected using filters. The emission and detection wavelengths for the three fluorescent probes used are presented in table 4.1.

Probe	Excitation	Emission
Bispyrene	344 nm	360-600 nm
DPH	360 nm	430 nm
Prodan	350 nm	360-600 nm

Table 4.1 emission and excitation wavelength for the fluorescent probes used.

LUV composed of 100% DOPC (Avanti Lipids) were made by extrusion through 1 μm membranes after resuspending dried lipids in PBS buffer (9 g/L NaCl, 144 mg/L KH_2PO_4, 795 mg/L Na_2HPO_4) and five cycles of freezing and thawing. LUV were then incubated for 5 minutes at 45°C or 15°C with varying

concentrations of peptide before measurements were taken. The temperature was held constant using a Fisher Scientific Isotemp 3006D water bath. The final lipid concentration in the sample was 160 μM . Fluorescent probes constituted less than 1% (molar) of the LUV composition. Bispyrene (Invitrogen) and Prodan (Invitrogen) were added to the chloroform solution of lipids before drying; DPH (Invitrogen) in acetonenitrile was added to the LUV solution and incubated for 15 minutes at room temperature.

4.2.2 Emission spectra as measure of lipid bilayer properties

We used three fluorescent molecules whose emission depends on the environmental conditions in which they are found. Each of these molecules responds to different properties of the environment and inserts into a different part of the lipid bilayer, allowing one to probe distinct aspects of membrane fluidity. Figure 4.1 shows a cartoon representation of the chemical structure of these probes and their spatial location withing a phospholipid bilayer.

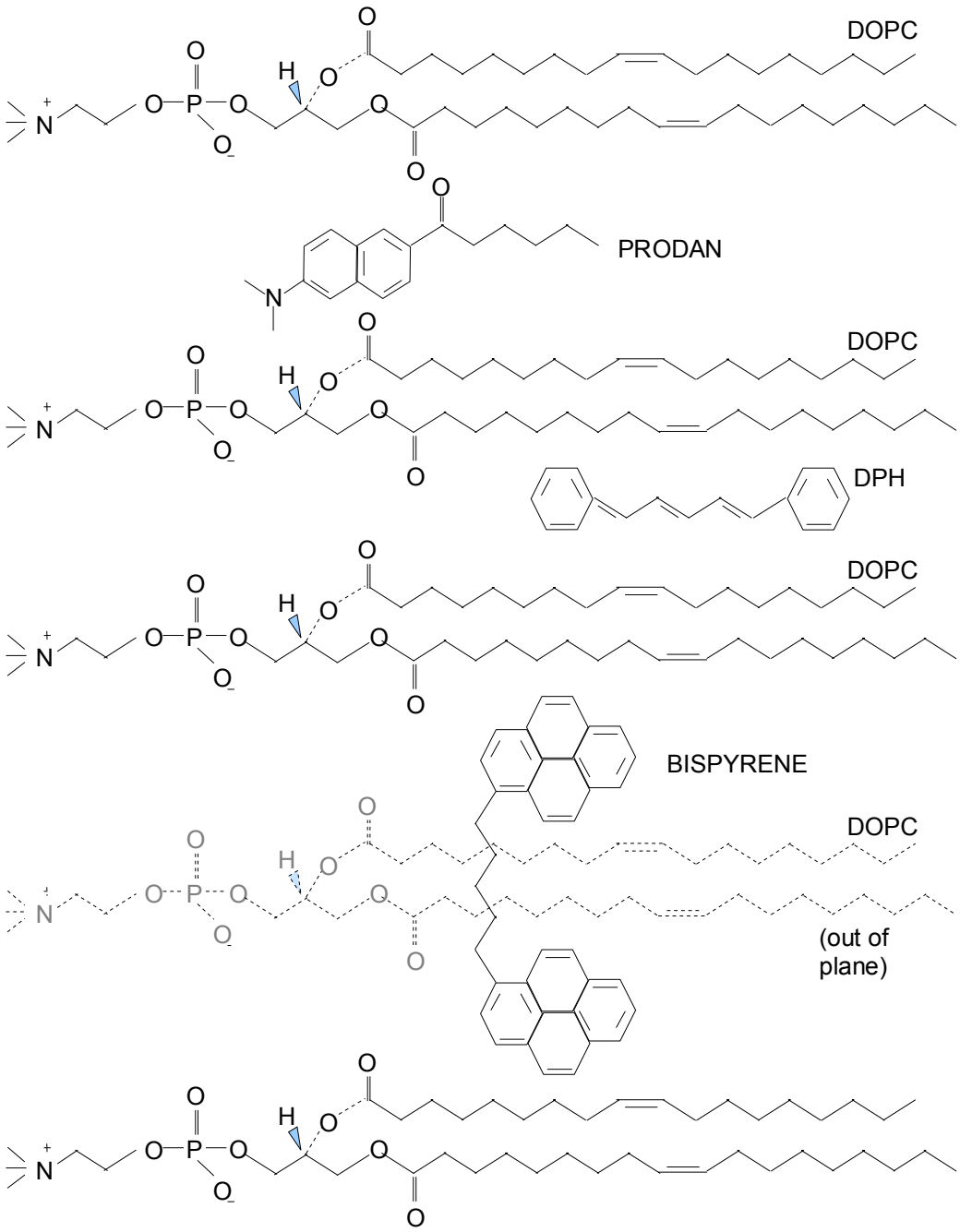

Figure 4.1: Location of fluorescent probes within a lipid bilayer. Location of prodan and DPH from (Kremer *et al*, 2001); location of bispyrene from (Galla and Sackmann, 1974).

1,6-diphenylhexatriene, or DPH, is a linear molecule that inserts in the hydrophobic region of the lipid bilayer. The absorption and emission dipoles of DPH are parallel, such that when DPH is excited using polarized light, it emits a polarized photon in the same direction as the excitation one. If the molecule is free to rotate in time scales similar to the decay time of the excitation, the emitted light will have a different polarization than the excitation light. If, on the other hand, its motion is restricted and it cannot rotate, the emitted light will have the same polarization as the excitation light.

Polarization of DPH embedded in LUV increases with decreasing temperature (figure 4.2), as the lipid tail groups, the hydrophobic core, get more tightly packed, restricting the probe's motion. This restricted motion results in a more polarized emission. Higher polarization values for DPH fluorescence indicate a more tightly packed membrane, or a more gel-like membrane.

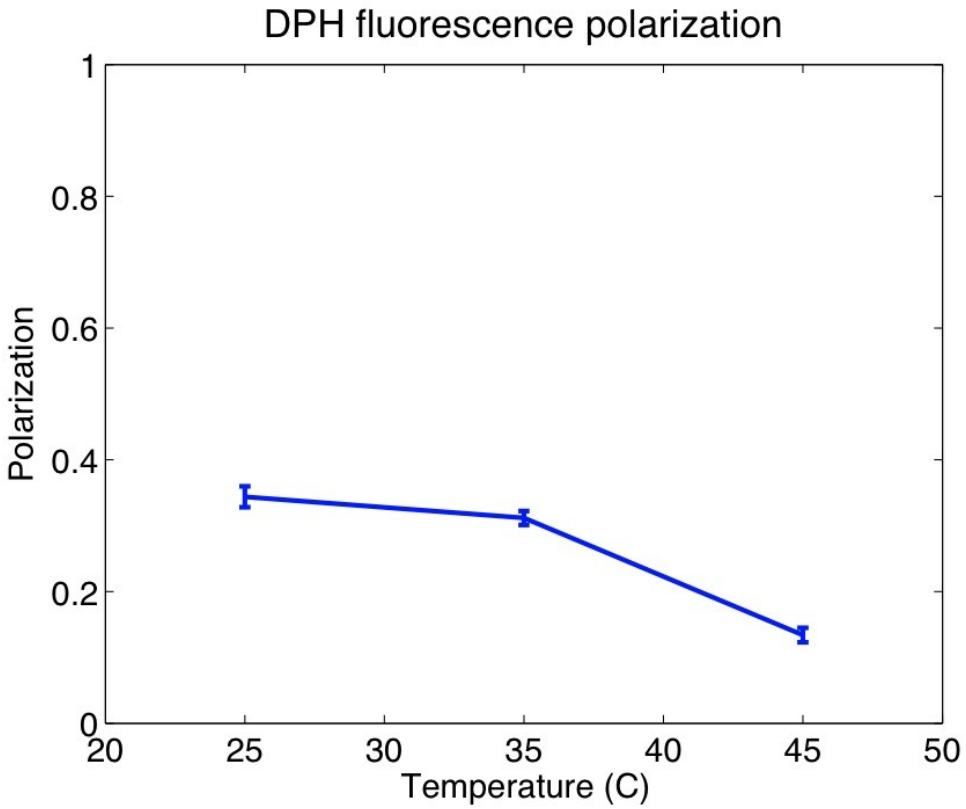

Figure 4.2: DPH polarization as a function of temperature – taken experimentally. Error bars represent one standard deviation of 5 – 7 measurements taken with the same sample.

Bispyrene consists of two pyrene molecules linked by a short carbon chain. Pyrene is a planar molecule, approximately 7 Å wide and 10 Å tall (Galla and Sackmann, 1974). As can be seen in figure 4.1, it is thought that it occupies the place of one lipid molecule in the semi-ordered structure of one monolayer. Pyrene molecules can form excimers, or excited dimers, which are short-lived excited complexes between an excited pyrene molecule and a second pyrene molecule in the ground state. Taking into account the possibility for excimer formation, the reaction for the decay of excited pyrene molecules into the ground state can be written as follows (Galla and Sackmann, 1974) :

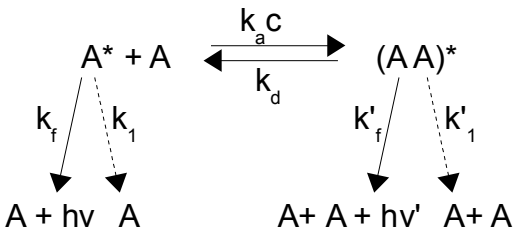

Figure 4.3: Chemical reaction scheme for excimers

The formation of an excimer is a second-order transition, characterized by the transition rate k_a, while the dissociation of the excimer is controlled by the rate constant k_d. The rate constants of the radiative decays back into the ground state are represented by k_f and k'_f for the monomer and the excimer, respectively. Non-radiative decay can also happen, with rate constants k_1 and k'_1 for monomer and excimer, respectively, though these processes are assumed to happen slowly.

Results of the studies of excimers tell us that the ratio of the quantum yield for excimer-to-monomer radiative decay is proportional to the ratio of the excimer-to-monomer emission fluorescence intensity, and is directly related to the association rate constant, k_a. Also, k_f/k'_f is not dependent on the temperature or other external parameters but is rather an intrinsic property of the fluorescent molecule (Förster and Kasper, 1954). Thus, the excimer-to-monomer emission fluorescence intensity ratio will give us a good idea of how likely the pyrene molecules come together in a given sample.

Bispyrene molecules can be used instead of single pyrene molecules. In this case, if the bispyrene molecules are present in a low enough concentration

that excited pyrene molecules can only bump into their sister pyrene molecule in the bispyrene, the excimer-to-monomer fluorescence intensity ratio will tell us the probability that the two pyrene parts of a single bispyrene come together, which will depend on how easily the lipids surrounding the bispyrene molecules move out of the way of the bispyrene thermally fluctuating in the lipid bilayer.

As seen in figure 4.4, bispyrene has two important emission peaks, one around 395 nm, corresponding to the emission of a single excited pyrene molecule, and one at around 484 nm, for the emission of excimers. When the lateral motion of bispyrene is restricted, the monomer emission dominates, with a high peak in intensity at 395 nm. In situations where the two pyrenes of a single bispyrene molecule can come close together with high probability, the excimer emission at 484 nm is relatively higher. The ratio of the emission intensity at 484 nm (excimer) to emission intensity at 395 nm (monomer) can be used as a way to determine changes in lateral diffusion in the membrane; higher values indicate decreased lateral diffusion, or a stiffer environment or higher viscosity (Wilson-Ashworth *et al*, 2006).

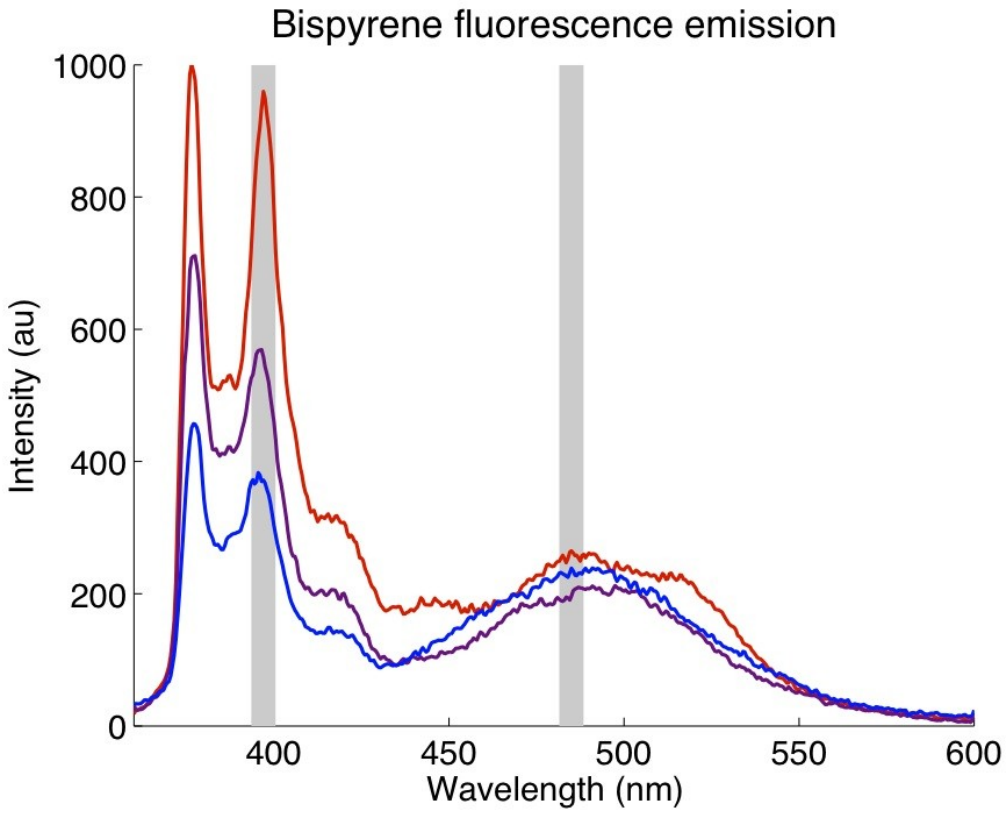

Figure 4.4: Bis-pyrene emission. 160 μM of 100% DOPC LUV. RED: taken at 25°C, low lipid mobility; PURPLE: taken at 35°C, medium lipid mobility; BLUE: taken at 45°C, high lipid mobility. Gray lines: wavelengths taken to calculate excimer-to-monomer ratio.

Prodan inserts into the lipid bilayer, though not very deeply. Hence, it is sensitive to the packing of the lipid headgroups (Wilson-Ashworth *et al*, 2006). The emission spectrum of prodan changes shape drastically when the polarity of the molecule's environment changes. We used a 3 wavelength generalized polarization (3wGP) measure to quantify these changes, developed by Krasnowska et al (1998).

The 3wGP is used instead of a simple generalized polarization, in which the intensity emission at two different wavelengths are treated as the vertical and

horizontal components in a polarization equation, as above. The 3wGP method, based on a modified generalized polarization equation, allows one to measure the partition of the probe between the aqueous and lipid environments.

To obtain the 3wGP value, the emission at three wavelengths is important: 420 nm, 480 nm, and 530 nm. The 3wGP value can be calculated using the following formula:

$$3\text{wGP} = \frac{R_{12} - 1}{R_{12} + 1} \qquad 4.1$$

where R_{12} can be calculated as follows:

$$R_{12} = \frac{I_1 + I_3 k_{32}}{I_2 + I_3 k_{32}} \qquad 4.2$$

I_1 , I_2 , and I_3 are the intensity of the fluorescence emission at 420 nm, 480 nm and 530 nm, respectively, and k_{32} is the ratio of the intensity at 530nm over the intensity at 480 nm when prodan is found in water. It is reported to have a value of 2.8 (Krasnowska *et al*, 1998).

Figure 4.5 shows the emission spectrum of prodan for highly packed lipid bilayers, which has a negative 3wGP value, for loosely packed lipid bilayers, with a positive 3wGP value, and and intermediate state. The emission spectrum of prodan for highly packed lipid bilayers (25°C) consists of two peaks, at around 420 nm and around 530 nm, and a valley at around 480 nm (RED). For intermediate packing of lipid bilayers (35°C), the two peaks increase in intensity and shift towards 480 nm (PURPLE). The emission spectrum of prodan for loosely packed lipid bilayers (45°C) consists of one peak at around 480 nm

(BLUE). Lower 3wGP values mean that the lipid headgroups are not tightly packed, as in lipids found at high temperature. On the other hand, higher 3wGP values can be interpreted as tighter lipid headgroup packing, as in lipids found at low temperature.

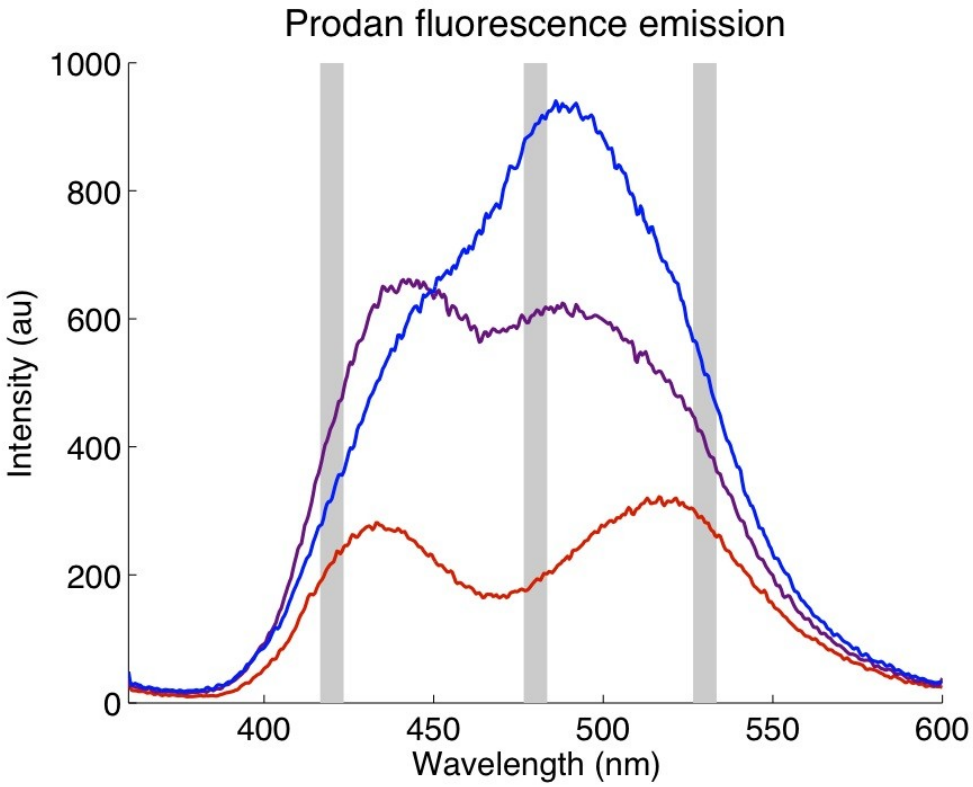

Figure 4.5: Prodan emission. 160 μM of 100% DOPC LUV. RED: taken at 25°C, low lipid mobility; PURPLE: taken at 35°C, medium lipid mobility; BLUE: taken at 45°C, high lipid mobility. Gray lines: wavelengths taken to calculate 3wGP.

4.3 Results

4.3.1 The myristoylated N-terminus of Arf1 [MyrArf1(2-17)] increases the packing of the hydrophobic region of the bilayer

Of the four molecules tested, only one had an effect on lipid packing, as measured by DPH polarization. As seen in Figure 4.6, MyrArf1(2-17) increases

the packing of the hydrophobic region of the lipid bilayer in a concentration-dependent manner, for concentrations up to 10 μM . The polarization increases with increasing concentration of peptide and reaches saturation at a maximum value of around 0.26. The polarization value for no peptide added was left as a fit parameter, and the value obtained, 0.061 is close to that measured in the experiment, 0.058. Addition of similar concentrations of either amphipathic helix, the N-terminus of Arf1 [Arf1(2-17)] and the ALPS domain of Kes1p, and of myristic acid had no effect on DPH polarization (figure 4.7).

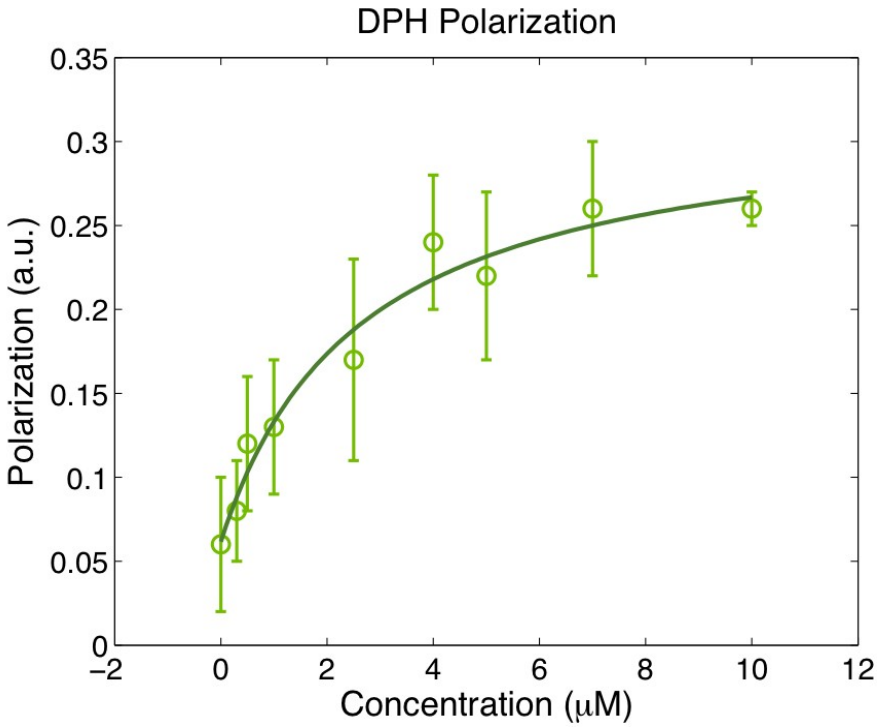

Figure 4.6 MyrArf1(2-17) had a concentration-dependent effect on DPH polarization, with a saturation effect. DPH polarization reached a maximum value of 0.26. Solid line is fit obtained using Matlab software; fit equation is: $P=0.06+0.26C/(2.63+C)$. Experiments were repeated at least 3 times; error bars represent one standard deviation.

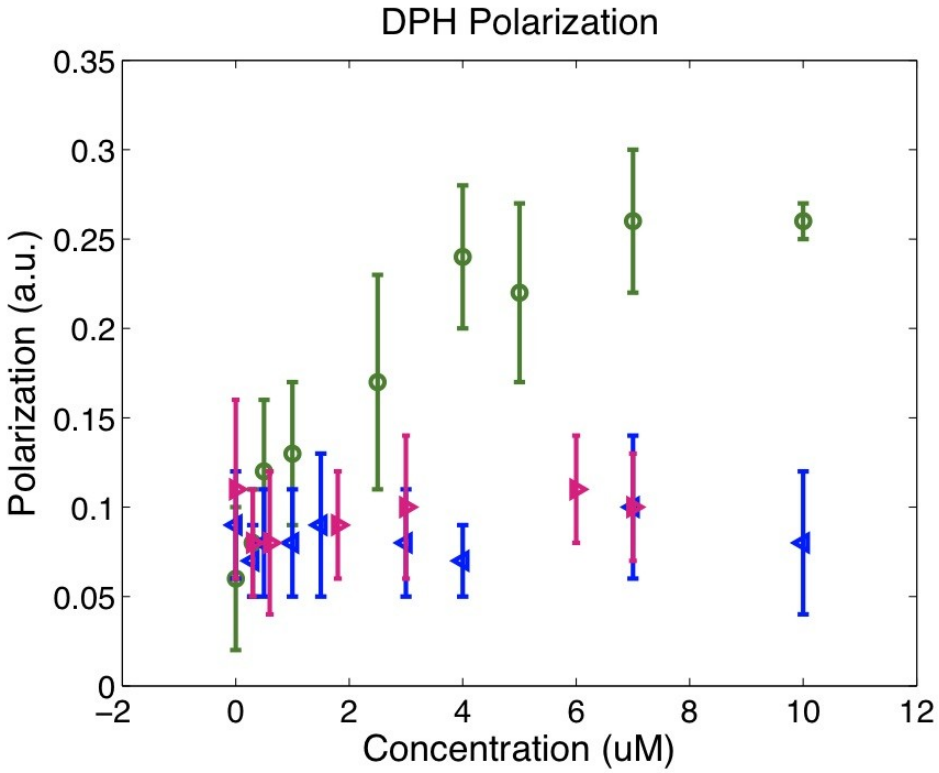

Figure 4.7: MyrArf1(2-17) (green circles) had a concentration-dependent effect on DPH polarization , while Arf1(2-17) (blue triangles) and myristic acid (pink triangles) had no effect on DPH polarization when added to LUV. Experiments were repeated at least 3 times; error bars represent one standard deviation.

4.3.2 MyrArf1(2-17) increases the packing of the lipid head groups

Figure 4.8 shows that MyrArf1(2-17) affected the 3wGP value for prodan fluorescence in a concentration-dependent manner. Increasing the amount of peptide in the sample increased prodan's 3wGP value.

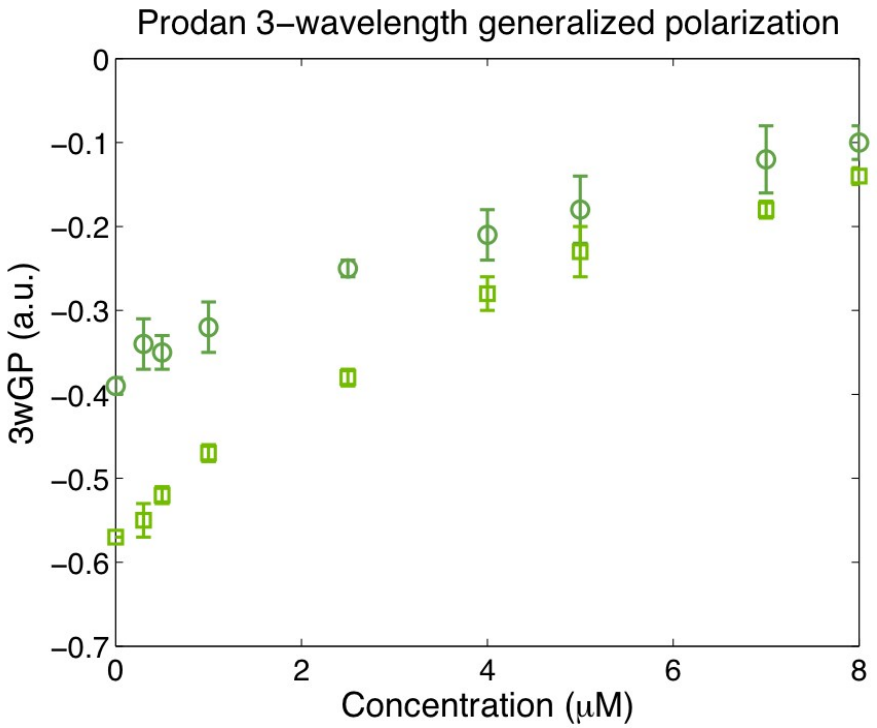

Figure 4.8 Increasing concentrations of MyrArf1(2-17) peptide increases the 3wGP value of prodan, both at 45°C (open squares) and 15°C (open circles). Experiments were repeated at least 3 times; error bars represent one standard deviation.

In order to test if the 3wGP value could cross from negative to positive values, we repeated the experiment at 15°C, also shown in Figure 4.7. At this temperature, DOPC LUV are still in a disordered, less viscous phase, as seen by the negative 3wGP value for LUV free of peptide. This 3wGP value is higher at 15°C than at 45°C meaning that the lipid head groups are more closely packed at 15°C.

Addition of MyrArf1(2-17) at 15°C increased the 3wGP value in a concentration-dependent manner. However, the 15°C data points are not all equally shifted from the 45°C data points, for similar concentrations of peptide.

We did not obtain positive 3wGP values, even for the highest concentrations of peptide used, and the saturation value is similar to the 45°C. This suggests that there is a temperature effect at work, as well as the concentration-dependent effect observed. Addition of 2.5 μM peptide had the same effect on prodan 3wGP values as decreasing the temperature by 30 ºC, from 45 ºC to 15 ºC.

We repeated the experiments for both alpha-helices, Arf1(2-17) and Kes1p ALPS domain, and for myristic acid, both for 15°C and 45°C. As seen in figure 2.9, none of these molecules had an effect on prodan fluorescence.

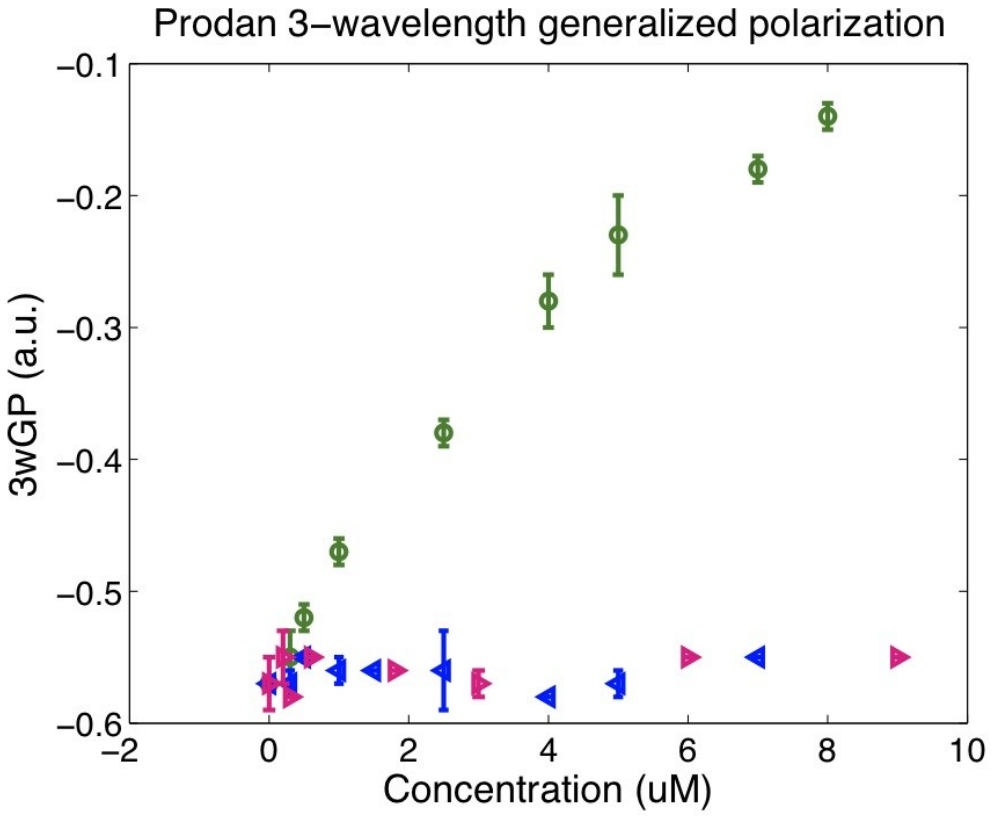

Figure 4.9: Increasing concentrations of MyrArf1(2-17) peptide increases the 3wGP value of prodan (green circles), while increasing concentrations of Arf1(2-17) peptide (blue triangles) and myristic acid (pink triangles) had no effect, at 45°C. Experiments were repeated at least 3 times; error bars represent one standard deviation.

4.3.3 Amphipathic helices with and without fatty acid chains have no effect on lipid lateral mobility

Bispyrene fluorescence spectra were not significantly different in the presence or absence of MyrArf1(2-17) at any concentration up to 10 μM. Similar results were found for Arf1(2-17), Kes1p ALPS domain, and Myristic acid. This is shown on figure 4.10.

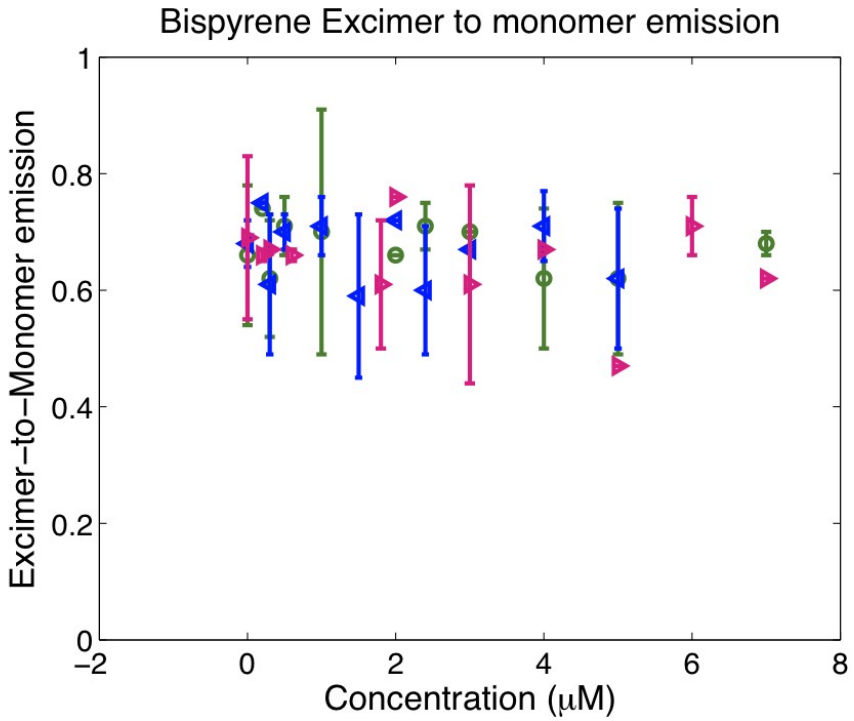

Figure 4.10 Bispyrene excimer-to-monomer fluorescence intensity ratio was not changed by increasing concentrations of MyrArf1(2-17) peptide, Arf1(2-17) peptide, Kes1p ALPS domain, or myristic acid. Experiments were repeated at least 3 times; error bars represent one standard deviation.

4.4 Summary

Fluorescence spectroscopy allows us to gauge the effects of peptides on the local properties of lipid bilayers, such as lipid packing and lateral mobility. Of the four molecules tested, only myristoylated N-terminus of Arf1 had an effect on the fluorescent probes. Addition of this peptide had a similar effect as reducing the temperature by up to 30 °C of lipid bilayers, as assessed by the fluorescence emission of prodan and the fluorescence polarization of DPH. Addition of the myristoylated form of the peptide increased lipid packing, while the individual components, the fatty acid and the alpha-helix by themselves had no effect, indicating that myristoylation is important for the peptide's effect on membranes. The myristoylated peptide had no effect on the lateral mobility of lipid molecules, as measured by the excimer-to-monomer emission intensity ratio of bispyrene. The increased lipid packing upon addition of peptide is consistent with an increase in surface tension, contrary to what we had hypothesized.

Chapter 5: Summary, Conclusion and Future Work

5.1 Summary

Bending rigidity and surface tension of lipid bilayers measured on GUV using techniques like flicker spectroscopy and pulling and retraction of tethers have large variability. The critical force for maintaining a stable tether varies from 2 pN to 10 pN for GUV in the absence of peptide, and also in the presence of peptide. The bending rigidity and surface tension found by fitting the equation for flicker spectroscopy to the fluctuation spectra of GUV were found to be independent of vesicle size, but with a large inter-batch variation. This makes the results of changing the environment, such as by adding membrane-binding peptides on the outside solution, inconclusive.

Addition of the myristoylated N-terminus of Arf1 to the outside of lipid vesicles did have an effect on some measures. The shape of the variance spectra of fluctuations for some cases in the presence of peptide was different than the cases in the absence of peptide. Also, tether retraction was linear, instead of logarithmic, and was associated with the formation of a bulge in vesicles in the presence of peptide. One strong caveat for these conclusions is that some GUV in the presence of peptide presented variance spectra similar to those of GUV in the absence of peptide, and some GUV in the absence of peptide also presented the bulge and linear tether retraction.

Finally, it is clear that addition of myristoylated N-terminus of Arf1

increases the lipid packing of bilayers. This can be seen by the fluorescence emission characteristics of the fluorophores prodan and DPH. The fluorescence emission of these probes in the presence of high concentrations of peptide was similar to that obtained when the temperature was decreased by up to 30 ºC. The other molecules tested had no effect on the probes used, indicating that myristoylation is important for the increased packing of the lipid molecules due to the presence of peptide.

5.2 Conclusion

In chapter 1, we presented a list of predictions based on our hypothesis that Arf1 induces or stabilizes curvature on the membrane, that it does so through the association of its myristoylated N-terminus with the membrane. In this section we present a summary of the results of testing these predictions, and comment on what this means for our understanding of the role of Arf1 in vesicle trafficking.

1) Insertion of the myristoylated N-terminus of Arf1 on one side of bilayer does not decrease bending rigidity. There is some evidence to suggest that addition of the peptide suppresses the thermal fluctuations of the membrane on all length scales.
2) Insertion of the myristoylated N-terminus of Arf1 on one side of bilayer does not decrease the force required to form and maintain a tether.

3) Insertion of the myristoylated N-terminus of Arf1 on one side of bilayer does not change non-local force present as a tether is pulled from a vesicle, meaning that the non-local properties of the bilayer are not changed.
4) Insertion of the myristoylated N-terminus of Arf1 on one side of bilayer increases lipid packing, making lipids more gel-like. This finding is consistent with increased surface tension and suppression of fluctuations on the membrane.
5) Insertion of the myristoylated N-terminus of Arf1 on one side of bilayer does not increase lipid lateral mobility.

Our results are contrary to our initial hypotheses. The increase in lipid packing by the Arf1 peptide, the possible appearance of a bulge at the base of retracting tethers, and the likely suppression of thermal fluctuations suggest that Arf1 might make bending the membrane more difficult. One could speculate that the role of Arf1 in the formation of a COPI vesicle is to locally increase the lipid packing, making the patch of membrane immediately surrounding Arf1 physically distinct from the rest of the membrane. This could then signal the other components of the COPI complex the location of the site of vesicle formation. In this model, insertion of Arf1 would not be sufficient to bend the membrane. Other parts are needed, like the presence of particular lipids, GTP, and coatomer or other proteins implicated in COPI vesicles.

An important conclusion from this work is that the models used to study lipid bilayers have to be revised or refined to include the effects of proteins. The suppression of fluctuations upon addition of Arf1 peptide in such a way that the variance of these fluctuations no longer follows the functional form predicted by the simple model indicates that the underlying assumptions that lead to this simple model, such as homogeneity, must be put to question. Also, the bulge found at the base of retracting tethers that was more likely to be found in the presence of peptide is an observation that the models for tether formation and retraction do not address.

5.2 Future Studies

In order to test the hypothesis that Arf1 serves as a curvature stabilizer, the experimental techniques presented here can be modified in order to better control the variability in the GUV samples.

It is unclear, for example, where the peptide is located on the membrane when it is deformed. We assumed that the peptide would coat all GUV within a sample homogeneously, though this may not be the case. Hence, the location of the peptide on the membrane, and even if there is peptide bound on the membrane of a given GUV, will have to be controlled. This can be accomplished by addition of fluorescently-labeled peptide, which can be purchased from specialized companies. Imaging the GUV using the fluorescent channel will provide further information useful in classifying the GUV being studied.

Appropriate controls would include addition of a different peptide that shows no effect on other measures of the physical properties of membranes and fluorescent molecules alone, to ensure that any effects observed are due to the Arf1 peptide and are not artifacts. As a positive control the experiments would have to be repeated with addition of a molecule that is known to increase bending rigidity of lipid bilayers, such as cholesterol.

In the pulling and retraction experiments, the GUV have a surface tension determined by the non-specific interactions with the glass cover slip. In order to have more control over the varying population of GUV in a given batch, one can perform the same experiments using the micropipette aspiration setup. This can be done two ways: the traditional micropipette aspiration experiments in which the bending rigidity is determined by finding the slope of the plot of surface tension as a function of area difference; a modified setup, where the surface tension is fixed, and known, as tethers are pulled. The large variability in GUV samples will make these experiments difficult to interpret, but perhaps having another measured parameter will allow one to detect subtle changes.

Finally, if Arf1 is related to highly curved surfaces, either as a generator or stabilizer, it is expected that it should localize on these highly curved surfaces, such as on the surface of a tether, or perhaps even on the neck of the tether, where the tether joins the vesicle. This can be tested by adding fluorescently-labeled peptide to the GUV in the setup described above. Again, appropriate controls would include addition of other fluorescently-labeled peptides and

fluorescent molecules, as well as cholesterol, to the lipid bilayer.

Bibliography

Alberts, B., Johnson, A., Lewis, J., Raff, M., Roberts, K., Walter, P. (Garland Science, 2002) *Molecular Biology of the Cell.*4th edition

Amor, J. C., Harrison, D. H., Kahn, R. A., Ringe, D. (1994) Nature **372,** 704-708

Aniento, F., Bernd Helms, J., Memon, A. R. (Blackwell Publishing, 2003) *The Golgi Apparatus and the Plant Secretory Pathway*

Baumgart, T., Hess S.T., Webb, W.W. (2003) Nature **425**, 821-824

Beck, R., Sun, Z., Adolf, F., Rutz, C., Bassler, J., Wild, K., Sinning, I., Hurt, E., Brugger, B., Bethune, J., Wieland, F. (2008) PNAS **105,** 33; 11731-11736

Bigay, J. Gounon, P. Robineau, S. Antonny, B. (2003) Nature **426**, 563-566

Bigay, J., Casella, J. F., Drin, G., Mesmin, B., Antonny, B. (2005) The EMBO Journal **24,** 2244-2253

Bo, L., Waugh, R.E. (1989) Biophys J **55**, 509

Boehm, M., Aguilar, R.C., Bonifacino, J.S. (2001) EMBO J. **20,** 6265–6276.

Bukman, D.J., Yao, J.H. Wortis, M. (1996) Phys Rev E **54**, 5; 5463-5468

Canham, P.B. (1970) J Theor Biol **26**, 61

Drin, G., Casell, J. F., Gautier, R., Boehmer, T., Schwartz, T. U., Antonny, B. (2007) Nature Structure and Molecular Biology **14,** 2; 138-146

Döbereiner, H.G., Evans E., Kraus, M., Seifert, U., Wortis, M. (1997) Phys Rev E **55**, 4458-4474

Döbereiner, H.G., Gompper, G., Haluska, C.K., Kroll, D.M., Petrov, P.G. Riske, K.A. (2003) Phys Rev Lett **91**, 048301

Donaldson, J.G., Cassel, D., Kahn, R.A., Klausner, R.D. (1992) Proc. Natl. Acad. Sci. USA. **89,** 6408–6412.

Duwe, H.P., Käs, J., Sackmann, E. (1990) J. Phys France **51**, 945-961

Engelman, D.M. (2005) Nature 438, 578-580

Evans, E. and Rawicz, W. (1990) Phys Rev Lett **64**, 17

Evans, E. Yeung, A. (1994) Chemistry and Physics of Lipids **73**, 39-56

Faucon J.F., Mitov, M. D., Méléard, P., Bivas, I., Bothorel, P. (1989) J Phys France **50**, 17; 2389-2414

Ford, M.G.J., Mills, I.G., Peter, B.J., Vallis, Y., Praefcke, G.J.K., Evans, P.R. and McMahon, H.T. (2002) Nature 419, 361-366.

Förster, Th., Kasper, K. (1954) A. Phys Chem **1**, 275-277

Galla, H.J., Sackmann, E. (1974) Biochemica et Biophysica Acta **339**, 103-115

Gerbeaud, C. (1998) PhD Thesis, University Bordeaux I

Gissen, P. and Maher, E. R. (2007) J Med Genet **44,** 545-555

Häckl, W., Seifert, U., Sackmann, E. (1997) J Phys II **7**, 1141

Helfrich, W. (1973) Z. Naturforsch **C28**, 693

Helfrich, W. and Servuss, R.M. (1984) Il Nuovo Cimento **3D**, 1

Hell, S., Reiner, G., Cremer, C., Stelzer, E.H.K. (1993) Journal of Microscopy **169**, 391-405

Jin, A.J., Nossal, R. (1993) Biophys J **65**, 1523-1537

Kahn, R. A., Randazzo, P. A., Serafini, T., Weiss, O., Rulka, C., Clark, J., Amherdt, M., Roller, P., Orci, L., Rothman, J. E. (1992) The Journal of Biological Chemisty **267,** 18; 13039-13046

Kass, M., Witkin, A., Terzopoulos D. (1988) International Journal of Computer Vision, 321-331

Krasnowska, E.K., Gratton, E., Parasassi, T. (1998) Biophysical Journal **74**, 1984-1993

Krauss, M., Jia, J. Y., Roux, A., Beck, R., Wieland, F. T., De Camilli, P., Haucke, V. (2008) The Journal of Biological Chemistry **283,** 41; 27717-27723

Kremer, J.J., Sklansky, D.J., Murphy, R.M. (2001) Biochemistry **40**, 8563-8571

Kummrow, M., Helfrich, W. (1991) Phys Rev A **44**, 8356

Lakowicz, J.R. (1983) Principles of Fluorescence Spectroscopy. Plenum Press, New York

Lee, C., Goldberg, J. (2010) Cell, in press

Lee, A.T., Balasubramanian, K., Schroit, A.J. (2000) Biochimica et Biophysica Acta **1509**, 475-484

Lundmark, R., Doherty, G. J., Vallis, Y., Peter, B. J., McMahon, H. T. (2008) Biochem J **414,** 189-194

Luo, R., Randazzo, P. A. (2008) The Journal of Biological Chemistry **283,** 32; 21965-21977

Mélélard, P., Gerbeaud, C., Bardusco, P., Jeandaine, N., Mitov, M.D., Fernandez-Puente, L. (1998) Biochimie **80**, 401

Mesmin, B., Drin, G., Levi, S., Rawet, M., Cassel, D., Bigay, J., Antonny, B. (2007) Biochemistry **46,** 1779-1790

Miao, L., Seifert, U., Wortis, M., Döbereiner, H.G. (1994) Phys Rev E, **49,** 6

Milner, S.T., Safran, S. A. (1987) Phys Rev A **36**, 4371-4379

Mutz, M., Helfrich, W. (1990) J Phys France **51**, 991

National Center for Biotechnology Information: http://www.ncbi.nlm.nih.gov/

Neuman, K.C., Block, S.M., Optical trapping. Review of Scientific Instruments (2004) 74, 9; 2787-2809

Nie, Z., Hirsch, D. S., Randazzo, P. A. (2006) Current Opinion in Cell Biology **15,** 396-404

Nie, Z., Randazzo, P. A. (2006) Journal of Cell Science **119,** 7; 1203-1211

Nossal, R. (2001) Traffic 2, 138-147

Nossal, R., Zimmerberg, J. (2002) Current Biology 12, R770-R772

Pan, J., Tristram-Nagle, S., Kucerka, Nagle, J.F., Biophys J (2008) 94, 117-124

Pécréaux, J., Döbereiner, H.G., Prost, J., Joanny, J.F., Bassereau, P. (2004) Eur Phys J E **13**, 277-290

Phillips, R., Kondev, J., Theriot, J. (Garland Science, 2009) *Physical Biology of the Cell*.

Poole, C., Losert, W. (2007) From: Methods in Molecular Biology, vol 400: Methods in Membrane Lipids, 389-404

Rawicz, W., Olbrich, K.C., McIntosh, T., Needham, D., Evans, E. (2000) Biophys J **79**, 328-339

Rossier, O. Cuvelier, D., Borghi, N., Puech, P.H., Derényi, I., Buguin, A., Nassoy, P., Brochard-Wyart, F. (2003) Langmuir **19**, 575-584

Sanchez-Martin, M.J., Amigo, J.M., Pujol, M., Haro, I., Alsina, M.A., Busquets, M.A. (2009) Anal Bioanal Chem

Safran, S. A. (Addison Wesley, 1994) *Statistical Thermodynamics of Surfaces, Interfaces, and Membranes*

Schneider, M.B., Jenkins, J.T., Webb, W.W. (1984) J Phys France **45**, 1457-1472

Singer, S. J., Nicolson, G. L. (1972) Science **175** 4023, 720-731

Song, J., Waugh, R.E. (1990) J. Biomech. Eng. **112**, 3, 235-241

Song, J., Waugh, R.E. (1993) Biophys J **64**, 1967

Veatch, S.L., Keller, S.L. (2003) Biophys J **85**, 3074-3083

Walpole, R.E., Myers, R.H., translation by Maldonado Vázquez, G. (1994) Probabilidad y Estadística (McGraw-Hill, 3rd Edition in Spanish)

Willemsen, O.H., Snel, M.M.E., Cambi, A., Greve, J., De Grooth B.G., Figdor, C.G. (2000) Biophys J **79**, 3267-3281

Wilson- Ashworth, H.A., Bahm, Q., Erickson, J., Shikle, A., Vu, M.P., Woodbury, D., Bell, J.D.(2006) Biophys J **91,** 4091-4101

Xu, C., Prince J.L. (1998) IEEE Transactions on Image Processing, 359-369

Zaremba S, Keen JH. (1983) J Cell Biol **97**, 1339 – 1347